

Stephen F. Austin State University

**SFA ScholarWorks**

---

Electronic Theses and Dissertations

---

Summer 8-6-2022

## **Geochemical Characterization of the Louann Salt, Puma Field, Green Canyon, Gulf of Mexico Basin – Using XRF and XRD**

Brian Lesh  
leshbl@jacks.sfasu.edu

Follow this and additional works at: <https://scholarworks.sfasu.edu/etds>



Part of the [Geochemistry Commons](#), and the [Geology Commons](#)

[Tell us](#) how this article helped you.

---

### **Repository Citation**

Lesh, Brian, "Geochemical Characterization of the Louann Salt, Puma Field, Green Canyon, Gulf of Mexico Basin – Using XRF and XRD" (2022). *Electronic Theses and Dissertations*. 455.  
<https://scholarworks.sfasu.edu/etds/455>

This Thesis is brought to you for free and open access by SFA ScholarWorks. It has been accepted for inclusion in Electronic Theses and Dissertations by an authorized administrator of SFA ScholarWorks. For more information, please contact [cdsscholarworks@sfasu.edu](mailto:cdsscholarworks@sfasu.edu).

---

## Geochemical Characterization of the Louann Salt, Puma Field, Green Canyon, Gulf of Mexico Basin – Using XRF and XRD

### Creative Commons License



This work is licensed under a [Creative Commons Attribution-Noncommercial-No Derivative Works 4.0 License](https://creativecommons.org/licenses/by-nc-nd/4.0/).

GEOCHEMICAL CHARACTERIZATION OF THE LOUANN SALT, PUMA FIELD,  
GREEN CANYON, GULF OF MEXICO BASIN – USING XRF AND XRD

By

Brian L. Lesh, Bachelor of Science

Presented to the Faculty of the Graduate School of

Stephen F. Austin State University

In Partial Fulfillment

Of the Requirements

For the Degree of

Master of Science

STEPHEN F. AUSTIN STATE UNIVERSITY

August, 2022

GEOCHEMICAL CHARACTERIZATION OF THE LOUANN SALT, PUMA FIELD,  
GREEN CANYON, GULF OF MEXICO BASIN – USING XRF AND XRD

By

Brian L. Lesh, Bachelor of Science

APPROVED:

---

Dr. Melinda Faulkner, Thesis Director

---

Dr. Julie Bloxson, Committee Member

---

Dr. Kevin Stafford, Committee Member

---

Dr. Robert Friedfeld, Committee Member

---

Freddie Avant, Ph.D.  
Interim Dean of Research and Graduate Studies

## ABSTRACT

The Jurassic-aged Louann Salt is an evaporite sequence deposited in the Gulf of Mexico Basin (GOMB). It is an important component of the GOMB petroleum system and influences the facies pattern in overlying strata and the distribution of petroleum stratigraphic traps. The Louann Salt is composed primarily of halite with intercalated anhydrites and silty or sandy-halite intervals, with overall thicknesses in excess of four kilometers (~13,000 feet). Suture zones occur intermittently within the Louann Salt, formed by the collision of allochthonous evaporite layers. The mineralogy and geochemistry of the suture zones are currently understudied and can be hazardous during drilling operations, potentially causing over-pressurization of the zone. Furthermore, these evaporite bodies are potential sources for critical minerals or Rare Earth Elements, which can also lend insight into depositional conditions during the Jurassic.

The focus of this study was to determine the bulk geochemistry of the allochthonous evaporite layers within the Louann Salt in the Puma Field of the GOMB. Geochemical analyses were performed by handheld X-ray fluorescence (XRF) on approximately 600 cutting samples from the Puma West GC821-002 well, ranging from 2,057 meters to 6,528 meters (6,750 feet to 21,420 feet) below the surface. X-ray diffraction (XRD) analyses were conducted on ten samples within the suture zone to determine its mineralogy.

The results of the XRF analyses delineated the upper and lower boundaries of the Louann Salt by the inverse relationship between the chlorine and silicon elemental values.

XRF analyses also indicate that the Louann Salt contains Rare Earth Elements (REEs) in the hundreds of part-per-million (ppm), such as Lanthanum (La), Praseodymium (Pa), Cerium (Ce), and Neodymium (Nd). REEs in the Louann are in concentrations equivalent to those being mined for economic value. XRD results indicate that the mineralogy of the suture zone is primarily composed of quartz, hematite, and smectite, with minor amounts of other clay minerals. This study provides insight into the depositional history of the Louann Salt and characteristics of the allochthonous bodies within the Louann for future mapping of the extent of these bodies in the GOMB.

## ACKNOWLEDGMENTS

I take this opportunity to express my gratitude and appreciation to the people who made this research possible. I would like to thank my thesis committee: my thesis advisor Dr. Melinda Faulkner, Dr. Julie Bloxson, Dr. Kevin Stafford, and Dr. Robert Friedfeld for their collaboration on my thesis. I am extremely grateful to Dr. Melinda Faulkner, for convincing me that I was ready for graduate school and continued motivation throughout my graduate career. Also, Dr. Julie Bloxson for her enthusiasm, guidance, and for teaching me the skills that I needed to successfully complete my thesis. I would also like to thank Christine Piela Cox and BP Exploration & Production, Chevron Corporation, and Talos Energy Inc. for the opportunity to be a part of this research, and for whom without this research would not be possible. Finally, I am deeply thankful for the constant encouragement and unwavering support I received from my friends, family, and my amazing wife, Courtney Lesh.

## TABLE OF CONTENTS

ABSTRACT .....	iii
ACKNOWLEDGEMENTS .....	v
TABLE OF CONTENTS .....	vi
LIST OF FIGURES .....	ix
LIST OF TABLES .....	xii
LIST OF EQUATIONS .....	xiii
LIST OF APPENDICES .....	xiv
1. INTRODUCTION .....	1
2. GEOLOGICAL SETTING AND REGIONAL GEOLOGY .....	3
3. REGIONAL STRATIGRAPHY .....	10
3.1 Puma Appraisal Area / Puma Diapir .....	10
3.2 Werner Formation (Jwe) .....	10
3.3 Louann Salt Formation (Jls) .....	15
3.4 Norphlet Formation (Jno) .....	15
3.5 Neogene Strata .....	16
4. SALT MOBILIZATION AND TECTONICS .....	17
4.1 Suture Zones .....	20
5. OBJECTIVES .....	22
6. SIGNIFICANCE .....	23
7. METHODOLOGY .....	24
7.1 X-Ray Diffraction (XRD) .....	25
7.2 X-Ray Fluorescence (XRF) .....	26
8. RESULTS .....	28
8.1 Cutting Descriptions .....	28
8.2 General Geochemistry .....	29
8.3 XRD Analyses .....	29



8.3.1	Suture Zone Mineralogy .....	29
8.3.2	XRD Graph Comparison .....	30
8.4	XRF Analyses .....	33
8.4.1	Major Elements Geochemistry .....	33
8.4.2	Elements of Interest (EOI) Element Geochemistry .....	36
8.4.3	Rare Earth Element (REEs) Element Geochemistry .....	39
8.5	Cross Plot Analyses .....	41
8.5.1	Major Elements Plots .....	41
8.5.2	Elements of Interest Plots .....	44
8.5.3	Rare Earth Elements Plots .....	49
9.	DISCUSSION .....	51
9.1	XRD Analyses .....	51
9.1.1	Suture Zone Mineralogy .....	51
9.2	XRF Analyses .....	53
9.2.1	Major Elements .....	53
9.2.2	Elements of Interest .....	56
9.2.3	Rare Earth Elements .....	58
9.3	Suture Zone Hypothesis .....	61
9.3.1	Suture Zone Formation .....	62
9.3.2	Sediment in the Suture Zone .....	67
9.3.3	Source of Minerals within the Puma Well Suture Zone .....	67
10.	LIMITATIONS TO STUDY .....	68
11.	CONCLUSIONS .....	69
12.	RECOMMENDATIONS FOR FUTURE STUDIES .....	71
13.	REFERENCES .....	72
14.	APPENDICES .....	80
14.1	Appendix A – Thermo Niton XL3t GOLDD+ Detectable Elements .....	80
14.2	Appendix B – Detected Elements from XRF Analysis .....	83
14.3	Appendix C – XRF Data .....	85

14.4	Appendix D – Detailed XRD Results .....	94
14.5	Appendix E – XRD Graphs .....	96
15.	VITA .....	106

## LIST OF FIGURES

Figure 1.1. Map of the Puma Field, Gulf of Mexico. ....	2
Figure 2.1. A. The configuration of North and South America (Late Triassic). L. Triassic and E. Jurassic Grabens (red shading), B. Configuration at close of Phase I extension. Extent of the Louann Salt (green, thick salt – dark green). Sea floor spreading (dashed black line). ....	4
Figure 2.2. Schematic diagram that shows the four phases of the early evolution of the Gulf of Mexico Basin. ....	5
Figure 2.3. Locations of the thick and thin transitional crust within the GOMB. ....	6
Figure 2.4: Configuration of the GOMB at close of Phase II (From Ewing and Galloway, 2019). ....	8
Figure 3.1. Location map of the Puma Appraisal Area / Puma Diapir within the Green Canyon Protraction Area. ....	11
Figure 3.2. NW – SE Seismic image of the Puma Diapir. Black line is the Puma West GC821-002 well. Red line is the GC 821-1 well drilled in 2010. ....	12
Figure 3.3. SW – NE Seismic image of the Puma Diapir. Black line is the Puma West GC821-002 well. ....	13
Figure 3.4. Stratigraphic column showing lithologic formations of the GOMB from the basement Paleozoic rocks through the Lower Cretaceous (Valanginian). ....	14
Figure 4.1. Example of the different salt structures that can form as a result of deformation in salt tectonics. ....	18
Figure 4.2. Cross Section model depicting an allochthonous salt amalgamation. ....	20
Figure 8.1. Figure shows variations in the salt as you move down core (left to right). A – Cuttings from sample 11940-11970. B – Cuttings within the suture zone, sample 13530 – 13560. C – Cuttings from sample 17580 – 17610. ....	29
Figure 8.2. XRD graph of samples 13,160 Spot – Fine and 13,830 – 13,860 Fine. XRD Legend. ....	32

Figure 8.3. Major Elements, XRF graphs of Mg, Si, S, Cl, and Ca. Black dashed lines represent a change in lithology. Lithology symbols and colors were based on the BakerHughes Atlas of Log Responses. ....	34
Figure 8.4. Elements of Interest, XRF graphs of Al, K, Fe, and Zr. Black dashed lines represent a change in lithology. Lithology symbols and colors were based on the BakerHughes Atlas of Log Responses. ....	37
Figure 8.5. Elements of Interest, XRF graphs of Ni, Ba, Zn, and Nb. Black dashed lines represent a change in lithology. Lithology symbols and colors were based on the BakerHughes Atlas of Log Responses. ....	38
Figure 8.6. Rare Earth Elements, XRF graphs of La, Ce, Pr, and Nd. Black dashed lines represent a change in lithology. Lithology symbols and colors were based on the BakerHughes Atlas of Log Responses. ....	40
Figure 8.7. Major elements Cross Plots from XRF analysis. Vertical lines indicate outside Louann Salt interval (left of line), suture zone interval (middle), and Louann Salt interval (right). ....	42
Figure 8.8. Cross plot of elements Ca vs S (ppm). A) Ca vs S – All Samples. B) Ca vs S – Only Cl >50%. C) Ca vs S – Suture zone only. ....	43
Figure 8.9. Cross Plots of Major Elements (Cl & Si) and Elements of Interest (Al &K) from XRF analysis. All cross plots compare elements concentration in ppm. A) Cl vs Fe. B) Si vs Fe. C) Al vs Fe. D) K vs Fe. ....	45
Figure 8.10. Cross Plots of EOI from XRF analysis. All cross plots compare elements concentration in ppm. A) Zn vs Fe. B) Zr vs Fe. C) Nb vs Fe. ....	46
Figure 8.11. Cross plot of Major Elements (Cl & Si) and EOI vs Nb. All cross plots compare element concentrations in ppm. A) Cl vs Nb. B) Si vs Nb. C) K vs Nb. D) Al vs Nb. E) Zn vs Nb. F) Zr vs Nb. ....	47
Figure 8.12. XRF cross plot analysis of elements Ni (ppm) and Ba (ppm). ....	48
Figure 8.13. Rare Earth Element Cross Plot analysis. Large plot on top shows all REEs (ppm) plotted together against chlorine (%). Bottom smaller plots are each REEs individually plotted against chlorine (%). ....	50
Figure 9.1. Cross plot of the suture zone interval from XRF data. All elements are plotted in ppm. A) Cl vs Fe. B) Si vs Fe. C) Al vs Fe. D) K vs Fe. ....	52

Figure 9.2: Cross plot of Ca vs S (ppm). A) Downcore XRF graphs of S and Ca. Location of possible anhydrite bed (Red box). B) The three points represent XRF samples 16,540 – 16,680. Correlation indicates the possibility of an anhydrite bed associated at these depths. ....55

Figure 9.3. Rare Earth Element Cross Plot analysis. Large plot on top shows all REEs (ppm) plotted together against S (ppm). Bottom smaller plots are individually plotted against S (ppm). ....60

Figure 9.4. Block diagrams showing the characteristics of allosutures and autosutures. A) Allosuture forms from coalescence of two split sheets sourced from different feeders. B) Autosuture forms between two lobes of the same salt sheet moving at different speeds or in different directions (From Dooley et al., 2012). ....63

Figure 9.5. Block diagram of an encircling autosuture. The advancing salt sheet divided into two lobes to bypass a grounded mini basin. The two lobes encircled this obstacle and rejoined on the downslope side (From Dooley et al., 2012). ....65

Figure 9.6. Block diagram of an encircling autosuture. A) The advancing salt sheet divided into two lobes to bypass a grounded mini basin. B) The two lobes encircled this obstacle and rejoined on the downslope side (From Dooley et al., 2012). ....66

## LIST OF TABLES

Table 7.1. Well data information for Puma West GC821-002 well. ....	24
Table 8.1. Sample intervals for XRF analysis. ....	28
Table 8.2. Condensed XRD results from RockJock Program. ....	31
Table 9.1. Salinity based classification paragenesis and brine properties based on concentration of seawater (Modified from Warren, 2016). ....	57

LIST OF EQUATIONS

Equation 1. Element (%) from ppm. ....35

## LIST OF APPENDICES

Appendix A. XRF handgun table with list of detectable elements. ....	80
Appendix B. Elements that were identified in the XRF analysis and corresponding average concentration in parts per million (ppm). ....	83
Appendix C. XRF Data. ....	85
Appendix D. Detailed XRD results. ....	94
Appendix E. All XRD Graphs. ....	96



## 1. INTRODUCTION

The Jurassic-aged Louann Salt is a massive evaporite series of halite that is intercalated with anhydrite and silty or sandy-halite intervals deposited within the Gulf of Mexico Basin (GOMB). The formation is an important component of the GOMB petroleum system which influences the facies patterns in overlying strata and the distribution of petroleum stratigraphic traps (Land et al., 1988). The Louann Salt is not a homogenous salt body, rather there are suture zones formed by the collision of allochthonous evaporite layers. These suture zones occur intermittently within the Louann and vary in thickness and chemical composition. The mineralogy and geochemistry of the suture zones are currently unknown and can be hazardous when drilling through these layers. Potential drilling hazards are due to anomalous pressure behavior of entrapped sediments (Weijermars, 2015 (A)).

Although the Louann Salt is important to the GOMB petroleum system, there is little information on the formation's geochemistry. This study focuses on the geochemistry of Louann Salt cuttings from the Puma West GC821-002, which were provided by BP Exploration & Production (Figure 1.1). The cuttings were collected from the Puma Diapir salt structure in the Green Canyon (GC) Block 821. The Puma Appraisal Area is in the southeast portion of the Green Canyon Protraction Area on the outer continental shelf, immediately north of the Sigsbee Escarpment (Weiland et al., 2008). The purpose of this

study is to develop a geochemical database that can provide industry with information that could help avoid hazardous situations when drilling through the Louann Salt, and establish methods for geochemical analyses of halite bodies. This information can also be used to correlate evaporite layers across the GOMB for future wells.

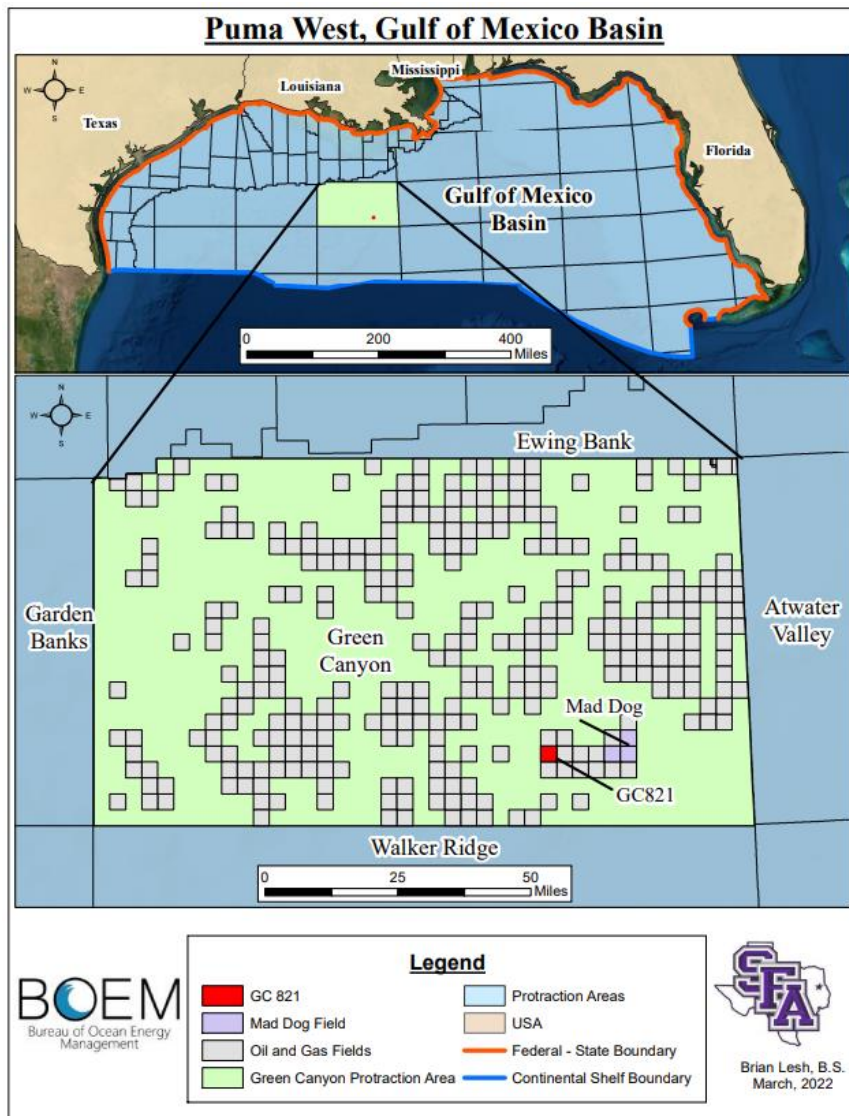


Figure 1.1. Location map of the Puma Field, Gulf of Mexico. (Modified from BOEM., 2022 (A)).

## 2. GEOLOGICAL SETTING AND REGIONAL GEOLOGY

The GOMB is a small ocean basin between the North American tectonic plate and the Yucatan block (Ewing and Galloway, 2019). The GOMB was opened in two phases during the separation of the North American plate from the supercontinent Pangaea (Ewing and Galloway, 2019). Phase I consisted of extension during the Late Triassic through the Middle Jurassic periods. Extension during this time was characterized by brittle deformation, including linear rift zones that created a complex series of northwest-trending grabens and half grabens, suggesting extension in the southwest direction (Rueda-Gaxiola, 2003; Salvador, 1991; Buffler, 1991). Initial rifting spread southward along the Central Atlantic spreading ridge, through a possible volcanic center in southern Florida, and the Bahamas (Figure 2.1; Pindell and Kennan, 2009). This rifting marked the initial breakup of Pangaea along the zones of weakness and sutures that formed during the Proterozoic and late Paleozoic as Pangaea was assembled (Buffler, 1991).

During the Middle Jurassic, the GOMB region underwent a period of rifting and attenuation that caused the beginning of the rotation of the Yucatan block and the formation of transitional crust and basement highs and lows that formed the basic architecture of the basin present today (Figure 2.2; Buffler, 1991). Stretching and hyperextension affected the outer portion of the basin by producing the relatively thick edges of the broad arches and sub-basin area. The broad crust that rims the outer edges of the basin is divided into an outer area of thick transitional crust and an inner area of thin transitional crust.

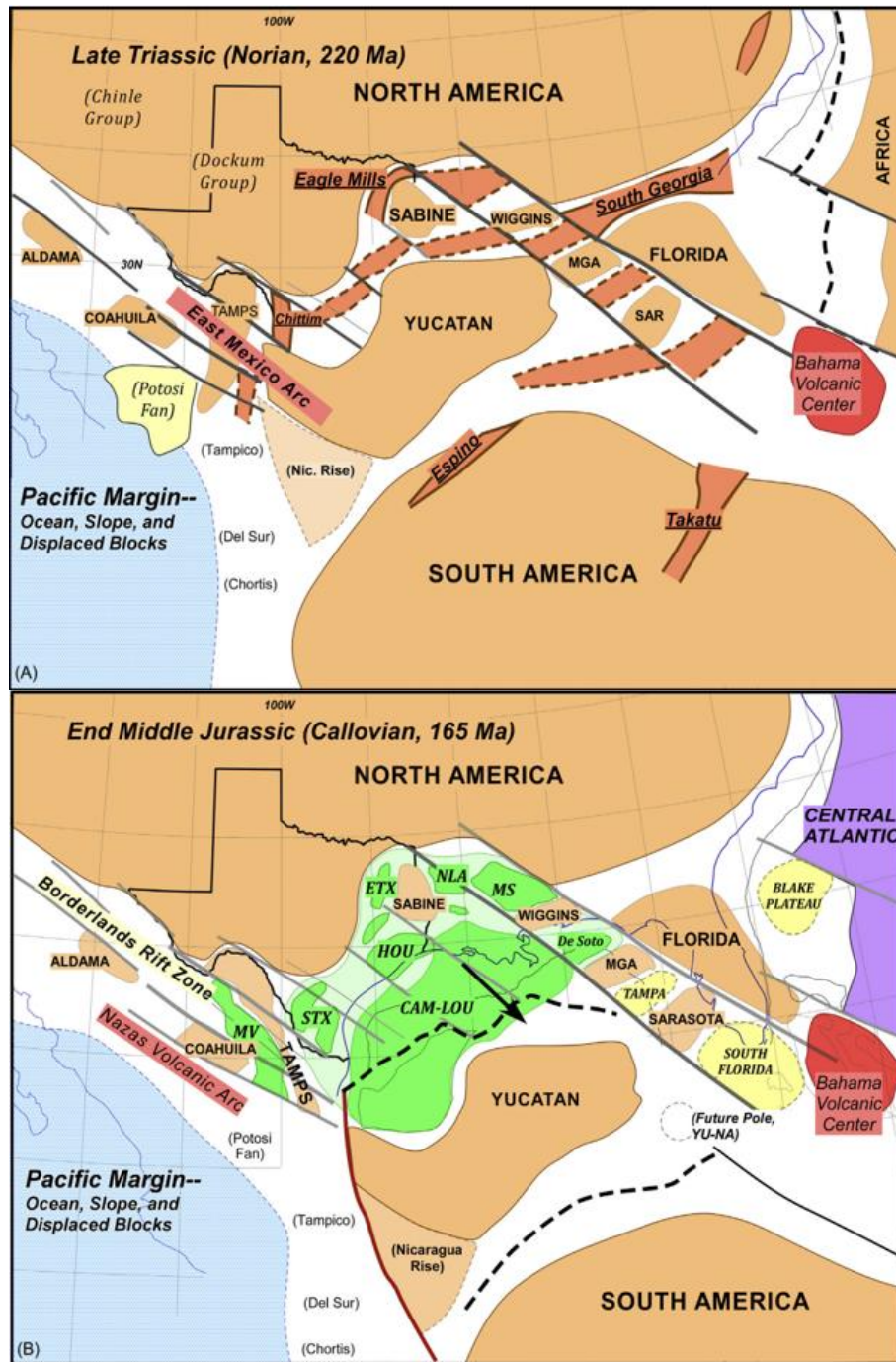


Figure 2.1: A) The configuration of North and South America (Late Triassic). L. Triassic and E. Jurassic Grabens (red shading). B) Configuration at close of Phase I extension. Extent of the Louann Salt (green, thick salt – dark green). Sea floor spreading (dashed black line) (From Ewing and Galloway, 2019).

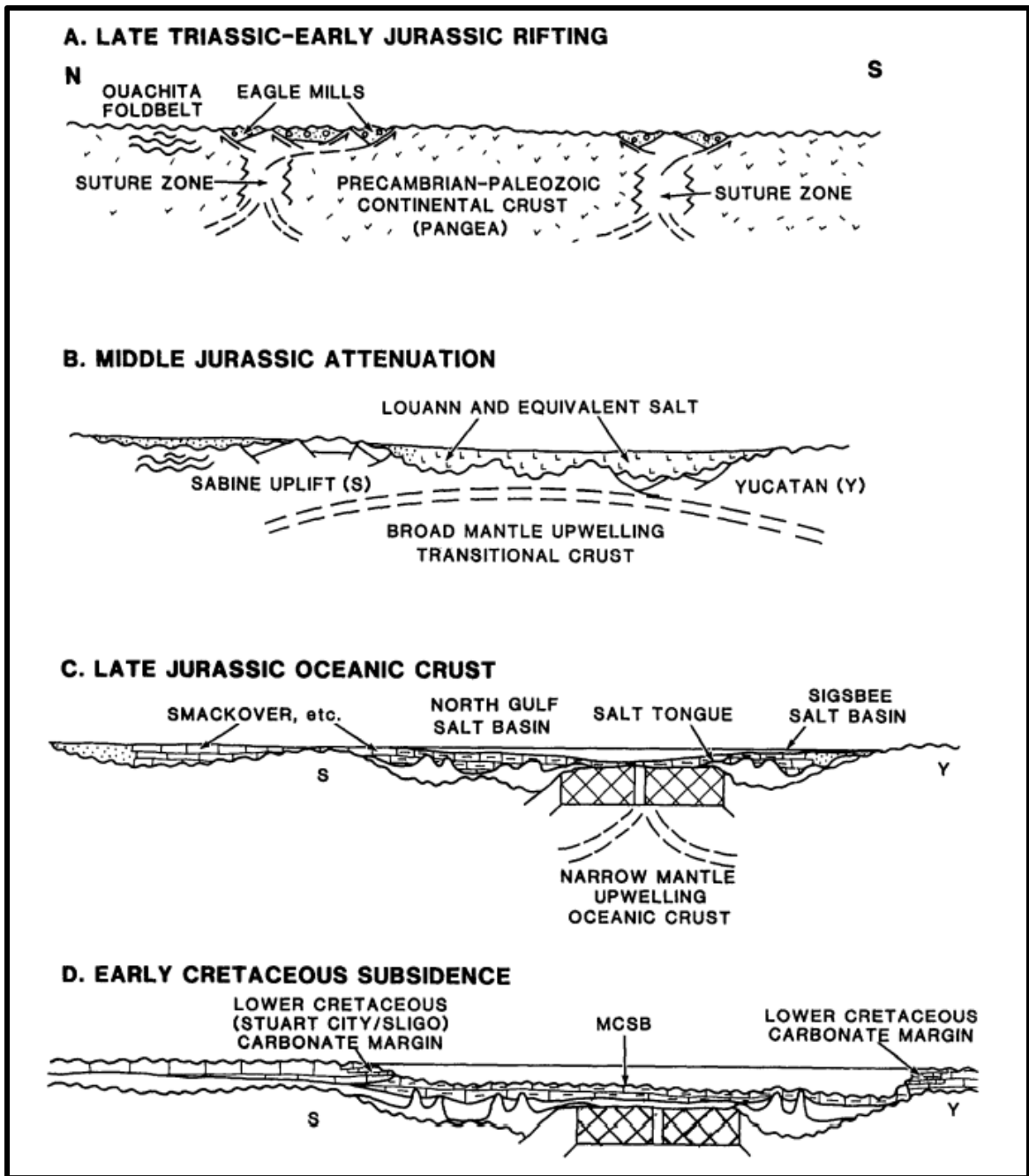


Figure 2.2. Schematic diagram that shows the four phases of the early evolution of the Gulf of Mexico Basin (Late Triassic through the Early Cretaceous) (From Buffler, 1991).

The thick transitional crust is an area of continental crust that had undergone moderate attenuation during the break up of Pangaea. It is characterized by a series of arches and basins with varying thicknesses of 20 – 35 km (65,615 – 115,000 ft) (Figure 2.3). The thin transitional crust is characterized by increased basement depths, decreased crustal thickness, and a marked change in orientation of basement features. The thin transitional crust has a varying thickness of 6 – 20 km (20,000 – 65,615 ft) (Figure 2.3; Buffler, 1991).

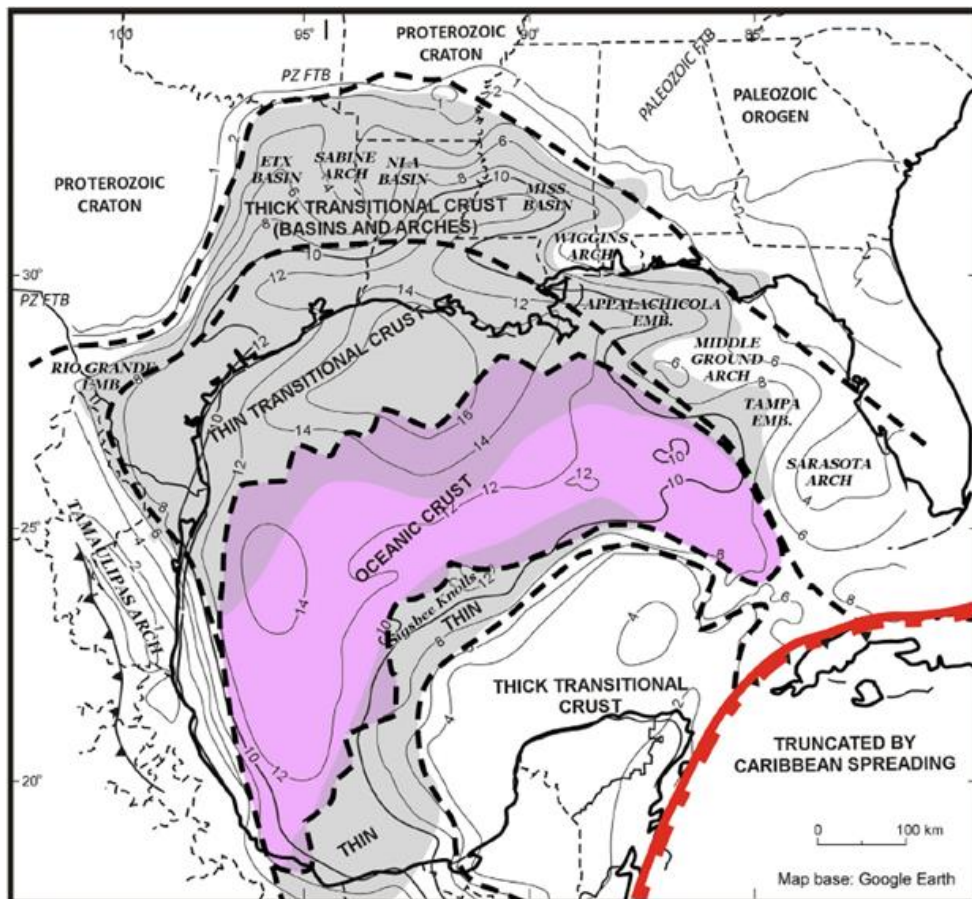


Figure 2.3. Locations of the thick and thin transitional crust within the GOMB (From Ewing and Galloway, 2019).

Furthermore, the center of the basin was more deformed due to relative proximity to the spreading center. This resulted in significant stretching and subsidence that led to the creation of an extensive sag basin, seen in Figure 2.2 (Buffler, 1991). Shortly after this sag basin was formed, deposition of the Louann Salt and other evaporites began (Ewing and Galloway, 2019). It is thought that the deposition of evaporites in the GOMB could have been synchronous with the collapse of the outer continental margin (Pindell et al., 2014). Rifting is thought to have continued through the deposition of the Louann Salt, and Phase I concluded (Hudec et al., 2013).

Phase II consisted of rotational seafloor spreading and the generation of oceanic crust along a generally east to west trend; this spreading continued through the Late Jurassic into the Early Cretaceous (Figure 2.4; Pindell and Kennan, 2001, 2009). Deepwater sediments were deposited over oceanic crust while shallow to deep shelfal environments were established adjacent to areas of transitional crust (Figure 2.2; Buffler, 1991). As the Yucatan block continued to rotate, it was accompanied by large amounts of NNW–SSE dextral shear along the western flank of the basin (Pindell and Kennan, 2001). Crustal rupture and emplacement of basaltic crust began in the Oxfordian and continued through the end of the crustal spreading in the Late Berriasian or Early Valanginian (Ewing and Galloway, 2019). Between the Oxfordian and Valanginian, the GOMB was formed by 100 – 500 km (62 – 310 mi) of extension due to the southeast movement and counter-clockwise rotation of the Yucatan block by 42 degrees to the basin’s present-day location (Marton and Buffler, 1999; Ewing and Galloway, 2019).

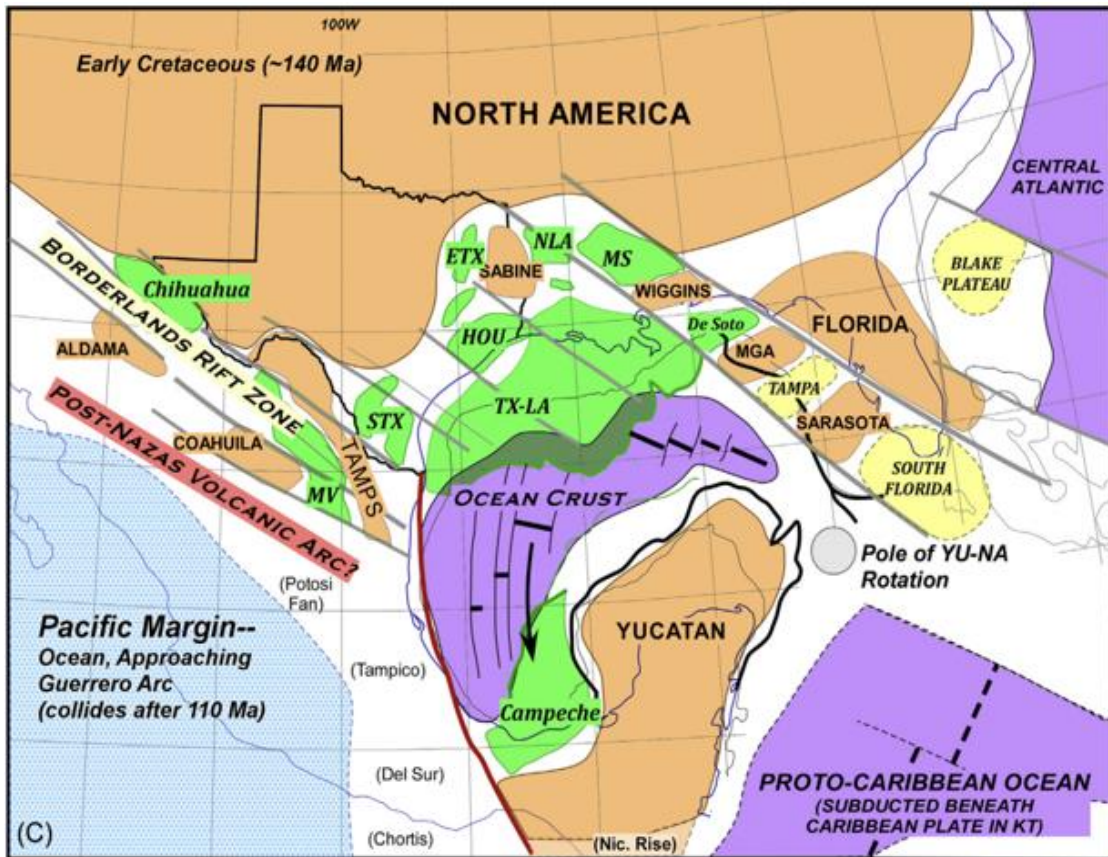


Figure 2.4: Configuration of the GOMB at close of Phase II (From Ewing and Galloway, 2019).

After seafloor spreading ceased, cooling and subsidence of the oceanic crust and the stretched continental margins dominated basin development (Ewing and Galloway, 2019). Once the Gulf of Mexico was locked into its present-day configuration, broad carbonate platforms were established that became the boundary of differential subsidence between thin transitional and oceanic crust, and thick transitional crust (Figure 2.2). In the Middle Cenomanian, there was a rapid fall and extended rise in sea level that was likely



caused by a combination of seafloor spreading, an increase in volcanic activity at mid-ocean ridges, a warmer climate, and continental uplift. This combination resulted in sea level that drowned the carbonate platforms, causing the carbonate margins to retreat landward. This widespread submarine erosion of the Early Cretaceous created the Middle Cretaceous sequence boundary (Buffler, 1991). The Late Cretaceous and Cenozoic history are dominated by load-induced subsidence beneath basinward-prograding delta and shoreline systems, complicated by intrabasinal gravity tectonics (salt and shale) and extrabasinal tectonics on the western margin (Ewing and Galloway, 2019).

### 3. REGIONAL STRATIGRAPHY

#### 3.1 Puma Appraisal Area / Puma Diapir

The Louann Salt cuttings from the Puma West GC821-002 well were collected from the “Puma Diapir,” a salt diapir of the Jurassic-aged Louann Salt emplaced within Miocene/Pliocene strata in the Puma appraisal area of the GOMB (Figure 3.1). The Puma Appraisal Area is located in the southeastern corner of the Green Canyon Protraction Area and extends from GC Block 821 to GC Block 825, and is included in at least 13 oil and gas fields. Weiland et al. (2008) described the sea floor of the Puma Appraisal Area as rugged and shattered due to the growth of the Puma salt structure causing extensive faulting, tilting, stratigraphic thinning, and mass wasting (Figures 3.2 and 3.3).

#### 3.2 Werner Formation (Jwe)

The Werner Formation disconformably overlies the Eagle Mills Formation of the Triassic to Early Jurassic period and is overlain by the Louann Salt Formation (Figure 3.4; Mancini et al. 1990). This formation is composed of an upper massive anhydrite member and a lower member that consists of conglomerates similar to those in the Eagle Mills Formation (Wade and Moore, 1993). The Werner Formation is discontinuous in its distribution, and its deposition appears to have been preferential to actively subsiding areas (Mancini et al., 1990). The maximum thickness of Werner strata is thought to be over 400 m (1,310 ft) (Tew et al., 1991).

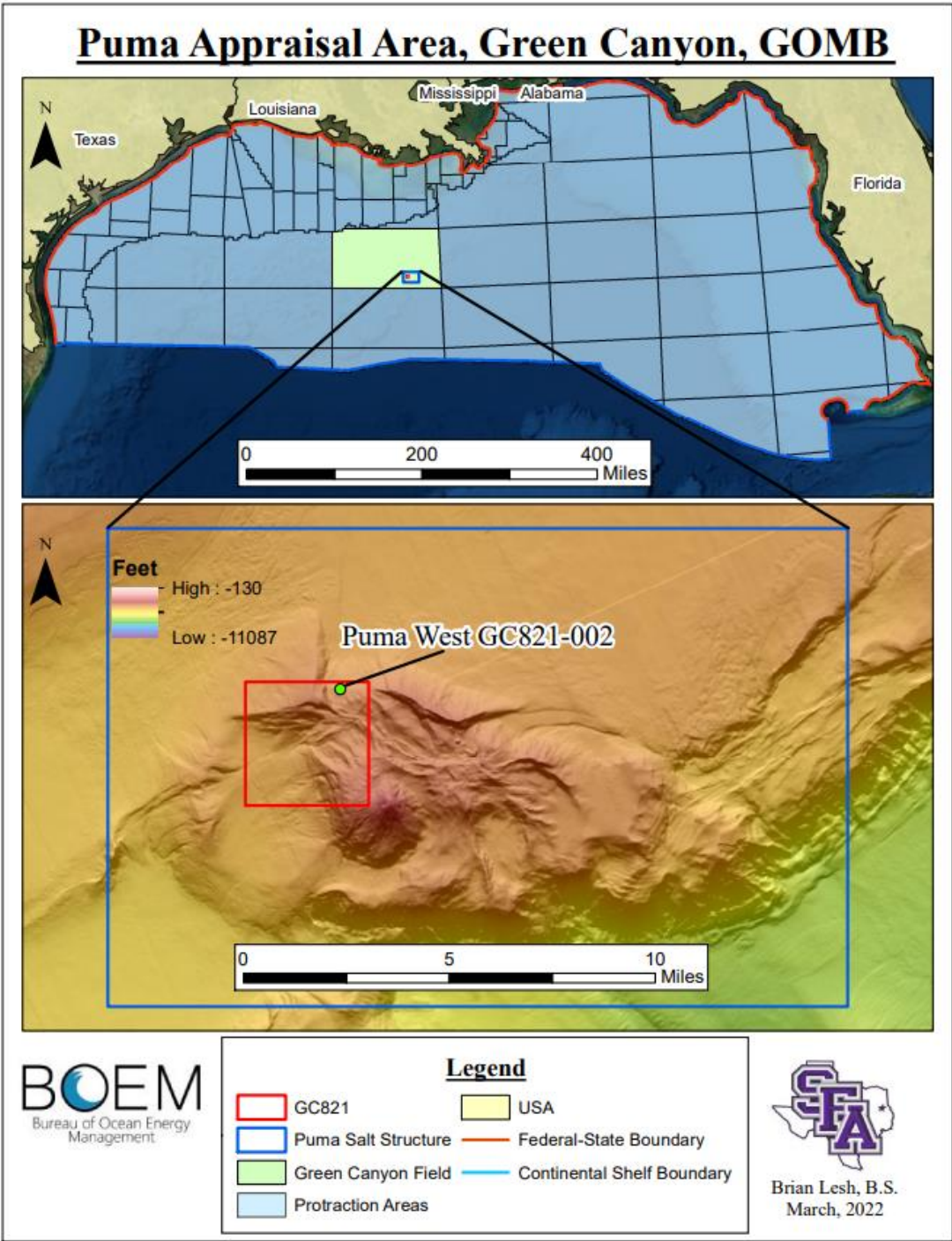


Figure 3.1: Location map of the Puma Diapir within the Green Canyon Protraction Area (Modified from BOEM., 2022 (A) and BOEM., 2022 (B)).

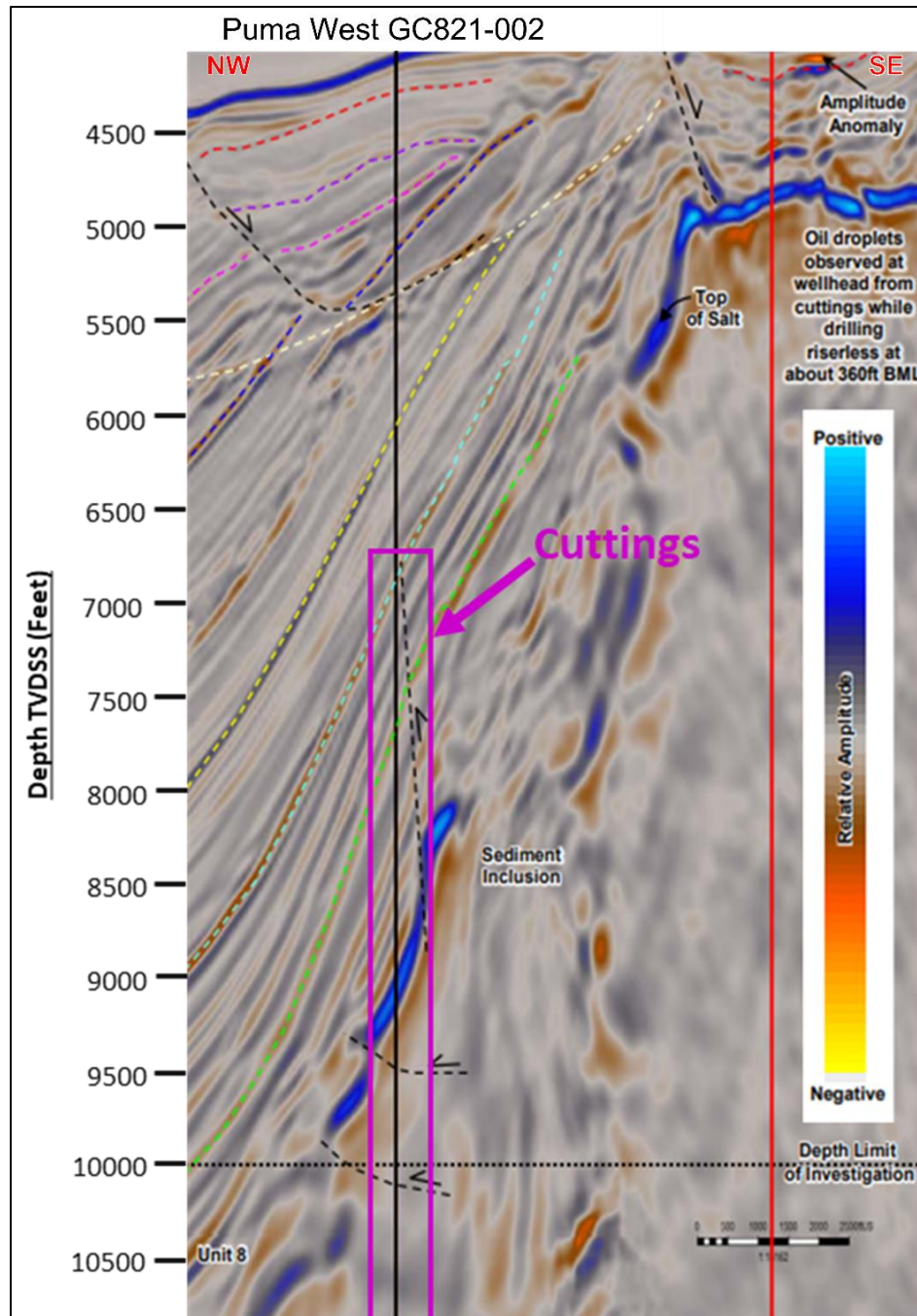


Figure 3.2: NW – SE Seismic image of the Puma Diapir. Black line is the Puma West GC821-002 well. Red line is the GC 821-1 well drilled in 2010. Purple box indicates the location where the cutting samples were collected (Modified from BP, E.& P.I., 2019).

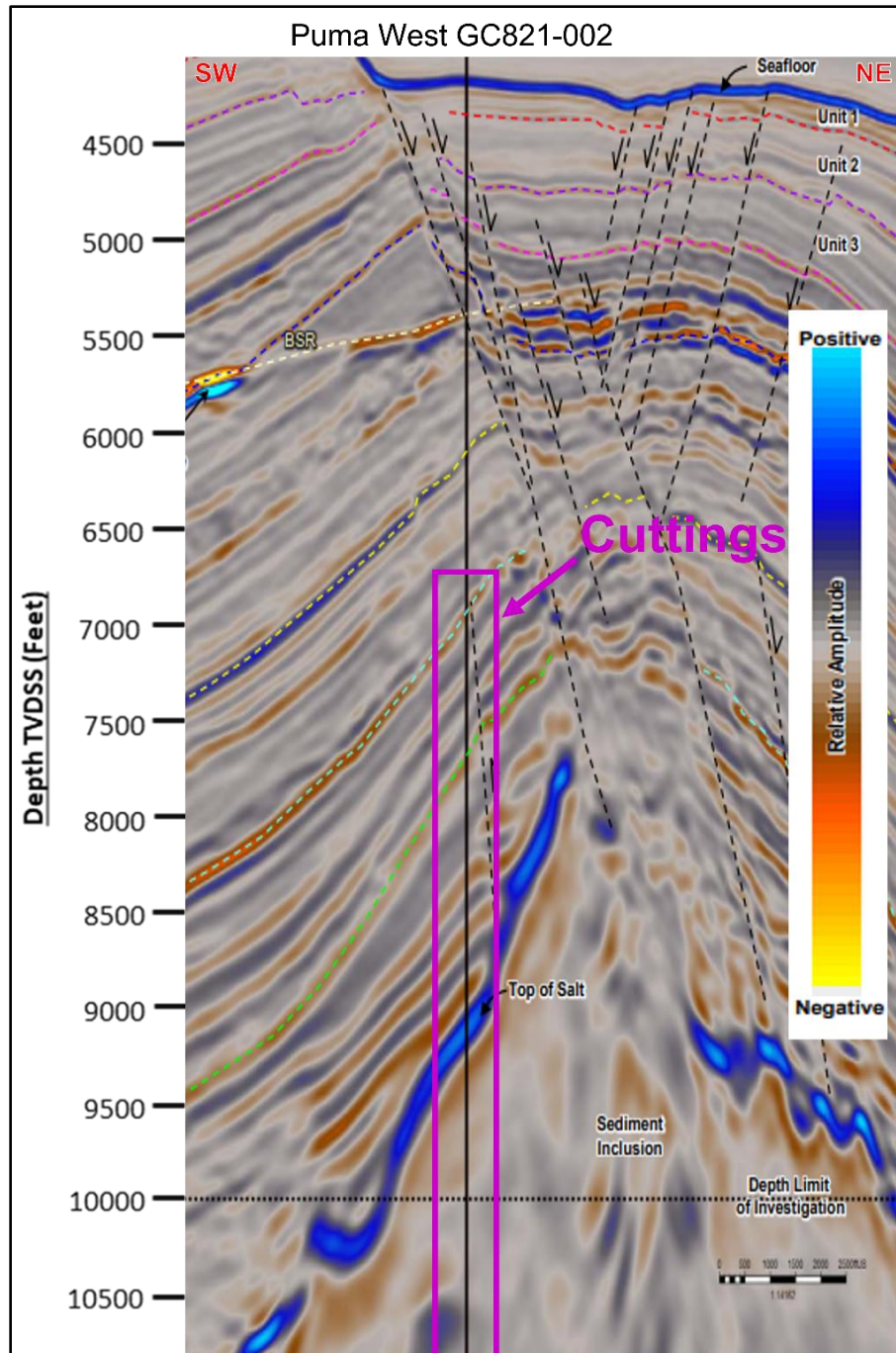


Figure 3.3: SW – NE Seismic image of the Puma Diapir. Black line is the Puma West GC821-002 well. Purple box indicates the location where the cutting samples were collected (Modified from BP, E.& P.I., 2019).

Age (Ma)	SERIES	STAGE	Lithostratigraphy
140	Lower Cretaceous (in part)	Valanginian	Cotton Valley Group
		Berriasian	
145	Upper Jurassic	Tithonian	Haynesville Formation Buckner Anhydrite (Lower Haynesville) Upper Smackover Formation Lower Smackover Formation Norphlet Formation Pine Hill Anhydrite Member Louann Salt
150		Kimmeridgian	
155		Oxfordian	
		Callovian	
160			
165		Middle Jurassic	
170			Triassic Eagle Mills Formation Paleozoic Rocks
	Underlying Beds		

Figure 3.4. Stratigraphic column showing lithologic formations of the GOMB from the basement Paleozoic rocks through the Lower Cretaceous (Valanginian) (From Obid, 2005).

### 3.3 Louann Salt Formation (Jls)

The Louann Salt is an evaporite sequence that was deposited during the Middle Jurassic after the creation of an extensive sag basin caused by stretching and subsidence (Buffler, 1991). The Louann Salt was deposited in an anoxic, hypersaline environment after an influx of marine water and intense evaporation. It consists primarily of halite with minor (1 – 5%) amounts of anhydrite, gypsum, shale, and fine sand (Caesar et al., 2019; Andrews, 1960). The salt is characterized as being white to gray, translucent, coarsely grained halite (Andrews, 1960). The formation conformably overlies the Werner Formation, or in absence of the Werner, disconformably overlies the Eagle Mills Formation or basement rocks (Figure 3.4; Mancini et al., 1990). In the Puma Diapir, the salt is allochthonous, and overlies Miocene strata and underlies Pliocene – Miocene strata. The Louann Salt has a variable thickness across the GOMB that can be over four km (13,120 ft). (Ewing and Galloway, 2019).

### 3.4 Norphlet Formation (Jno)

The Norphlet Formation comprises a regressive depositional sequence of terrigenous clastics derived from the erosion of the bordering highland areas. (Mancini et al., 1990). The Norphlet Formation is a non-fossiliferous, eolian sandstone that was deposited during the Oxfordian and is underlain by the Louann Salt and overlain by the Smackover Formation (Figure 3.4; Hunt et al., 2017; Salvador, 1987). The Norphlet Formation thickness ranges between 200 – 245 m (650 – 800 ft) and may reach 300 m (980

ft) (Mink et al., 1990). This formation contains four lithofacies: conglomerate, arkosic sandstone, quartzose sandstone, and shale (Badon, 1975; Mancini et al., 1985). The paleogeography of the Norphlet Formation during deposition was dominated by a broad desert plain bordered on the north and east by the Appalachian Highlands and on the south by the developing GOMB (Mancini et al., 1990). Widespread eolian sandstone, few fossils, extensively oxidized red beds, and the underlying evaporites indicate that the Norphlet Formation was deposited in an arid continental setting (Mancini et al., 1985; Tew et al., 1991).

### 3.5 Neogene Strata

Because of the allochthonous nature of the Louann, the strata below the Louann Salt cuttings in this well are Miocene in age. The lowermost cuttings are primarily a silty-shale that quickly grade into a sandy-silt, and continues to fluctuate up core. This interval is approximately 457 meters (1,560 feet) thick. The strata above the Louann Salt cuttings are Pliocene – Miocene in age. Directly above the salt, is predominantly sand-prone intervals that are overlain by fine-grained mass transport deposits (MTDs) interbedded with sand-prone intervals. The uppermost cuttings, are fine-grained MTDs with interlayered silts (BP, E.& P.I., 2019). This interval is approximately 790 meters (2,580 feet) thick.



#### 4. SALT MOBILIZATION AND TECTONICS

Salt tectonics (halokinesis) is the general term that encompasses notions of lateral and vertical salt flow, trans-stratal salt movement, salt pillowing, and diapirism that involves tectonic deformation of halite or other evaporites as a substratum or source layer (Warren, 2016). Salt tectonics are unique from most clastic and carbonate deformation because under subsurface conditions, salt behaves like a viscous fluid with negligible yield strength in the subsurface and at the surface (Hudec and Jackson, 2007; Warsitzka et al., 2011). Salt becomes gravitationally unstable in the subsurface due to impure salt having an approximate density of  $2.2 \text{ g/cm}^3$ , less dense than most carbonates and moderately to fully compacted siliciclastic rocks. This causes salt bodies to become buoyant when overlain by denser overburden (Hudec and Jackson, 2007). Salt tectonics can be separated into two principles: differential loading and the incompetence of salt in the subsurface.

Differential loading is what drives salt tectonics and makes halokinesis a more passive process (Warren, 2016). There are three types of loading that drive salt flow: gravitational, displacement, and thermal loading. Gravitational loading is similar to the concept of hydraulic head in fluid statics, where the weight of overlying rocks in combination with gravitational forces causes the salt body to be forced upward until the acting forces are in equilibrium (Kehle, 1988; Hudec and Jackson, 2007). Displacement loading occurs when salt bodies move toward or away from one another during regional shortening or extension, causing deformation to preexisting salt structures such as salt

diapirs (Figure 4.1). Salt diapirs are defined as salt flow features showing discordant interactive contacts with the encasing sedimentary strata, with shapes and geometries that are a response to salt's inherent mechanical weakness. Thermal loading is the result of volume changes caused by changes in temperature, where the salt expands and becomes buoyant due to changes in thermal convection (Hudec and Jackson, 2007).

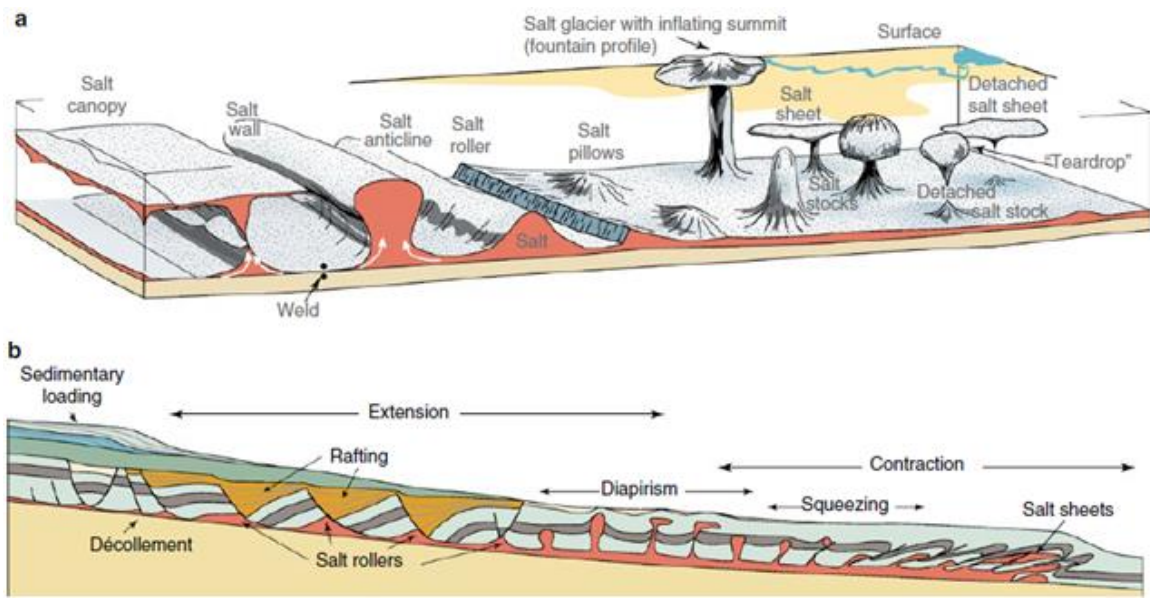


Figure 4.1: Example of the different salt structures that can form as a result of deformation in salt tectonics (From Warren, 2016).

The second principle that influences salt tectonics is that salt is a very weak and incompetent layer in the subsurface; its lateral flow and sliding carries along with its overburden in extension and acts as a *décollement* in compression (Warren, 2016). A

décollement is the detachment zone between two bodies of rock as a result of deformation (Sherkati et al., 2005). During extension, the overburden is thinned and fractured causing the underlying salt to fill in the fractures in a process called “reactive diapirism.” If the salt is less dense than the overburden, the diapir will continue to grow upwards until it reaches an overlying formation that it is unable to move through and will continue to stretch (Hudec and Jackson, 2007). During compression, the preexisting salt structures are reactivated and will continue to grow upwards. If there are no salt structures when compressional forces occur against the salt, it will detach from the upper and lower units, and create new structures or follow the path of the compressional forces along fault planes (Hudec and Jackson, 2007).

In the Gulf of Mexico Basin, the combination of a kilometers-thick (0.62 mi), basin-flooring Jurassic Louann Salt, rapid sediment loading, and offlap of a high-relief, continental-margin sediment prism resulted in the mass transfer of salt and over-pressured mud up-section and basinward throughout the history of the Northern Gulf of Mexico (Ewing and Galloway, 2019). Structures as a result of salt tectonics in the GOMB include growth fault families, allochthonous salt bodies, salt welds, roho fault families, salt diapirs, compressional fold-belts, and raft tectonics (Ewing and Galloway, 2019). Fort and Brun (2012) characterized the salt tectonics of the northern Gulf of Mexico by two regional-scale directions of salt flow towards the southeast and southwest in the northwest and northern margins, respectively.

#### 4.1 Suture Zones

Suture zones in salt bodies form when two bodies of allochthonous salt amalgamate. The contact location between the salt bodies is the “suture zone” (Bouroullec and Weimer, 2007). Figure 4.2 depicts a suture zone forming from two separate salt diapirs. As the diapirs form, one diapir forms into a salt tongue and the other a salt stock. Salt migration causes the salt from both structures to amalgamate, coalescing two allochthonous salt bodies to form the suture zone.

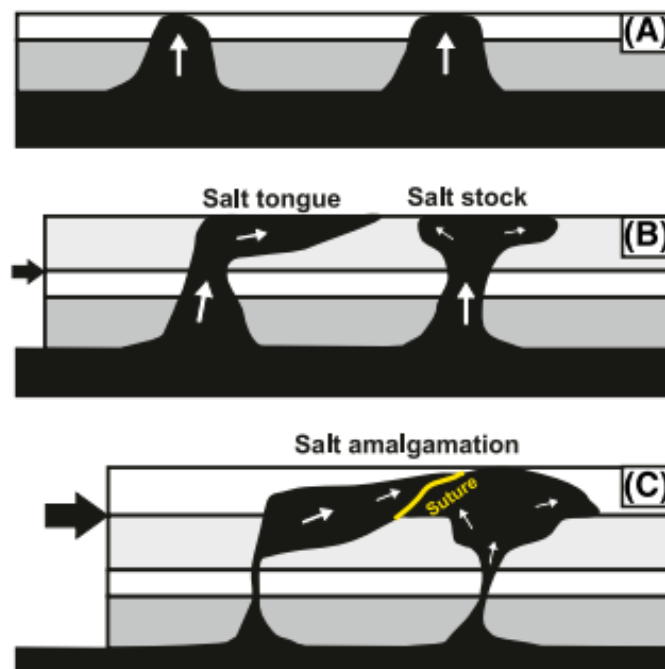


Figure 4.2: Cross Section model depicting an allochthonous salt amalgamation. A) Two salt diapirs rise. B) One diapir evolves into an allochthonous salt tongue and the other forms an allochthonous salt stock. C) Salt migration causes both allochthonous salt bodies to amalgamate, forming a salt suture at the contact location (From Bouroullec and Weimer, 2007).

Dooley et al. (2012) further defines sutures into two separate terms: autosutures and allosutures. Autosutures form by internal folding and disruption of the original contact surface between one salt sheet and its overlying sediment veneer. Allosutures are larger and more prominent, and form when different salt sheets coalesce (Weijermars, 2015 (B)). When suture zones form, sediments become entrapped between the two salt bodies and can become potential drilling hazards due to anomalous pressure (Weijermars, 2015 (B)). Sediments trapped in suture zones are from the roofs of the allochthonous salt bodies involved in the collision (Dooley et al., 2012). At the base of a suture, a triangular shaped sedimentary wedge is formed. The wedge structures form by sedimentation in the space between the advancing salt sheets before they coalesce, or by slumping of material off the roof of the approaching salt sheets (Weijermars, 2015 (A)).

## 5. OBJECTIVES

The objectives of this research were to characterize the geochemical variations of the Louann Salt cuttings collected from the Puma West GC821-002 well and identify the mineralogy of the suture zone within the Louann Salt interval. Understanding how the geochemistry changes within the Louann Salt and determining the mineralogy of the suture zone will provide valuable information to operators in the GOMB. These objectives were achieved by:

1. Determining the elemental composition of the Louann Salt by utilizing XRF on the GC821-002 well cuttings.
2. Determining bulk lithology of the well cuttings by analyzing the relationship between the concentrations of major elements – Mg, Si, S, Cl, and Ca.
3. Identifying the relationship between elements of interest (Al, K, Fe, Ba, Ni, Zn, Nb, and Zr) and Cl.
4. Creating a methodology for analyzing halite in XRD, and characterizing the mineralogy of the suture zone cuttings using XRD.
5. Providing BP with the elemental and mineralogical data collected on the Louann Salt.

## 6. SIGNIFICANCE

The purpose of this research was to identify the geochemical variations within the Louann Salt and determine the chemical composition of the suture zone. At the time of this study, there were few studies published on the geochemistry of the Louann Salt. Knowing the chemical composition of these evaporite bodies is critical when drilling because the abrupt changes in lithology may cause over-pressurization of the well. This study will help BP Exploration & Production and the industry develop a better understanding of the geochemical variations within the Louann Salt and the associated suture zones.

## 7. METHODOLOGY

In order to characterize the elemental composition of the Louann Salt, X-ray fluorescence (XRF) and X-ray diffraction (XRD) analyses were performed on cutting samples from the Puma West GC821-002 well provided by BP Exploration & Production, representing approximately 4,470 meters (~14,670 feet) of the Puma Diapir. Note that these techniques have not been employed on halite bodies in either core or cuttings, and one aspect of this research was to determine the proper methodology. XRF was used to identify elemental variations and trends in 202 cutting samples in approximately 27.4 meter (~90 feet) intervals at depths above and below the suture zone, and approximately 9.1 meter (~30 feet) intervals within the suture zone. XRD was used to determine the mineralogy of ten samples in approximately 30.1 meter (~100 feet) intervals within the suture zone. The general information for the Puma West well is presented in Table 7.1.

Table 7.1: General Well Information (From BOEM. (C)).

API	Well Name	Company	Basin	Protraction Area	Field	Interval of Interest
608114073600	Puma West GC821-002	BP	GOMB	Green Canyon	Puma	6,750 – 21,420 ft.



## 7.1 X-Ray Diffraction (XRD)

XRD was used to determine the specific minerals within the Louann Salt suture zone. Ten samples were chosen in 30.5-meter (100 feet) intervals to determine the mineralogy within the suture zone. XRD was performed on a Bruker D8 Advance diffractometer. Samples were analyzed from 5 to 65, 2-theta ( $2\Theta$ ) using Cu K-alpha radiation ( $1.5418 \text{ \AA}$ ), with 0.02-degree steps and a count time of two seconds per step (Eberl, 2003). Before testing, the salt from each sample was dissolved using deionized (DI) water to reduce the effects of halite on the diffraction pattern. The cubic nature of halite has a strong diffraction and dominates the signal, causing difficulty in identifying the remaining minerals. Approximately 10.0 g of each sample was placed in a beaker with a magnetic spinbar, and placed onto a hotplate with a magnetic spinner. The beaker was half filled with DI water and was stirred for approximately ten minutes or until the salt crystals had been dissolved. To isolate the insoluble fraction from each sample, the sample was placed over filter paper in a funnel and rinsed with DI water filtered through the sample using an oil-driven vacuum. This dissolved the salt and isolated the insoluble minerals from the suture zone. As the DI water was pulled through the filter paper, more DI was added to continue the filtration process. Each sample was filtered for approximately 10 minutes. Samples were then dried overnight in an oven set at  $60.0^{\circ}\text{C}$ .

The methods outlined in Eberl (2003) were used to prepare each sample for XRD analysis. Samples were once again sieved to 250 microns and carefully placed into a side-pack XRD holder affixed with 600 grit wet-sand paper. This ensured that the clay minerals

were not “pressed” flat during the packing and were randomly oriented. Corundum was not added to samples in order to obtain a quantitative rather than qualitative analysis. A graph that compares the angle between the incident and the scatter beam ( $2\Theta$ ) and the intensity of the beam was produced. Weight percentages were calculated from the comparison of the integrated intensities and the integrated intensity of the internal standard (Eberl, D.D., 2003). The USGS software RockJock was used to analyze the XRD graph to determine the mineralogy of each sample. RockJock compares the integrated intensities of unknown mineral peaks in the pattern to a known database of minerals to determine which minerals are present.

## 7.2 X-Ray Fluorescence (XRF)

XRF analyses were performed using the Thermo Nitron XT3t GOLDD+ handheld analyzer on cuttings taken from the Puma West GC821-002 well to determine the elemental composition of the Louann Salt interval of the Puma well. Each cutting sample packet represented an agglomeration of 9.14 meters (30 feet) of material from the depth interval 2,057 – 6,528 meters (6,750 – 21,420 feet) below the sea level. Two sample intervals were chosen for the XRF analysis; 27.4 meter (90 feet) intervals for cutting packets outside the suture zone and 9.1 meter (30 feet) intervals within the suture zone.

All cutting samples were crushed using a pestle and mortar and sieved to 250 microns. Approximately 15 grams of each crushed sample was packed into a zip-lock sample bag and marked with the associated depth and box number. Approximately 5g of

each sample was then packed into an XRF sample cup (Series 1500) affixed with 0.4  $\mu\text{m}$  polypropylene X-ray film and back-packed by a cotton ball to fill any void space. The “Test All Geo Mode” of the Thermo Nitron handheld analyzer was used for a total of five minutes per sample (60 sec each for main, low, and high filters, and 120 for the light filter). Elements that can be tested for in the “Test All Geo Mode” can be found in Appendix A. After all samples were analyzed, the results were downloaded from the Thermo Nitron analyzer into a Microsoft Excel spreadsheet for ease of data organization.

## 8. RESULTS

### 8.1 Cutting Descriptions

Cutting samples of the Louann Salt ranged from fine to very coarse, angular grains. Some of the sample packets were duplicates of the same depth interval, including a fine-grained and coarse-grained sample. “Spot” locations were taken at various depths, indicating a change in the sample or a possible area of interest. Table 8.1 indicates the sampling interval used during the geochemical analyses. The color of the salt cuttings ranged from a whitish-gray up core from the suture zone (Figure 8.1a); samples within the suture zone were mostly covered with a red clay veneer on the surface of the salt clasts (Figure 8.1b); and Louann Salt cuttings down core from the suture zone were light-reddish pink (Figure 8.1c).

Table 8.1: Sampling intervals for XRF analysis

Interval	Interval Depth	XRF Sample Interval	XRF Samples Tested	XRD Sample Interval	XRD Samples Tested
Pliocene – Miocene Strata	6,750 – 9,330 ft (2,057 – 2,844 m)	90 feet	32	N/A	N/A
Upper Louann Salt	9,420 – 13,145 (2,871 – 4,007 m)	90 Feet	43	N/A	N/A
Suture Zone	13,160 – 14,010 (4,011 – 4,270 m)	30 Feet	28	100 Feet	10
Lower Louann Salt	14,040 – 19,770 (4,279 – 6,026 m)	90 Feet	73	N/A	N/A
Miocene Strata	19,868 – 21,420 (6,056 – 6,529 m)	90 Feet	26	N/A	N/A



Figure 8.1: Color variations in the salt cuttings from: A. Upper Louann (sample 11,940-11,970 ft (3,639 – 3,643 m)); B. Suture zone (sample 13,530 – 13,560 (4,124 – 4,133 m)); and C. Lower Louann (sample 17,580 – 17,610 (5,358 – 5,367 m)).

## 8.2 General Geochemistry

The average concentrations in parts-per-million (ppm) of major elements, elements of interest (EOI) and rare earth elements (REEs) within the Puma Well cutting samples can be found in Appendix B. Overall, geochemical variations in the cuttings are related to changes in lithology from marine clays and shales to salt. The main geochemical variation within the Louann Salt interval is the suture zone at 4,011 m (13,160 feet). This suture zone is approximately 259 m (850 feet) thick and consists of quartz, hematite, and clay-coated salt.

## 8.3 XRD Analyses

### 8.3.1 Suture Zone Mineralogy

The results from the XRD analyses showed distinct differences in mineralogy that were split into two broad categories: non-clay minerals and clay minerals. Non-clay minerals detected include quartz, hematite, microcline, barite, goethite, and residual

amounts of halite and sylvite; the dominant non-clay minerals were quartz and hematite. Clay minerals detected include smectite, halloysite, glauconite, dickite, biotite, chlorite, muscovite, palygorskite, and illite; the dominant clay minerals were smectite and halloysite. The condensed results of the XRD analysis are shown in Table 8.2. The expanded XRD results are located in Appendix D, and report the different forms of each mineral identified within the suture zone.

### 8.3.2 XRD Graph Comparison

All suture zones samples analyzed with XRD had similar mineralogy. The mineralogy of Samples 13,160 (4,011 m) Spot – Fine and 13,830 – 13,860 (4,215 – 4,225 m) Fine represent the upper and lower boundary of the suture zone interval (Figure 8.2). The upper boundary is represented by sample 13,160 (4,011 m) Spot – Fine (Figure 8.2A). Minerals present within this sample include barite, biotite, dickite, goethite, halite, hematite, microcline, palygorskite, quartz, and smectite. The lower suture zone boundary is represented by sample 13,830 – 13,860 (4,215 – 4,225 m) (Figure 8.2B). Minerals present within this sample include barite, dickite, glauconite, halite, hematite, microcline, quartz, and smectite. The main variation between each of the 10 samples is the intensities of the peaks from five to 20 two-theta ( $2\theta$ ). All XRD graphs can be found in Appendix E.

Table 8.2: Condensed XRD Results. Table is divided by clay/non-clay minerals and the minerals weight % identified in each sample (Eberl, D.D., 2003).

Sample Name: (Feet)	13,160 Spot Fine	13,200 – 13,230	13,350 – 13,380 Fine	13,410 – 13,440 Fine	13,500 – 13,530	13,635 Spot Fine	13,710 – 13,740	13,830 – 13,860 Fine	13,920 – 13,950 Fine	13,978 Spot Fine
Degree of Fit:	0.0372	0.0876	0.0775	0.0633	0.0377	0.0451	0.0393	0.0455	0.0451	0.0490
Mineral	Wt %	Wt %	Wt %	Wt %	Wt %	Wt %	Wt %	Wt %	Wt %	Wt %
<b>NON-CLAYS</b>										
Quartz	25.5	32.0	28.7	23.0	26.0	26.7	25.7	26.2	28.6	24.6
Hematite	20.7	12.2	10.4	15.6	19.4	17.1	16.9	17.1	20.3	19.6
Microcline	6.6	6.5	5.6	6.0	6.7	6.0	6.7	6.3	7.3	7.4
Barite	4.1	4.8	4.1	5.1	5.4	3.3	2.4	6.9	7.4	2.9
Anhydrite	2.7	5.3	6.5	2.9	1.3	0.6	2.5	1.9	2.2	4.0
Gypsum	1.8	2.7	1.7	1.8	2.6	2.1	2.1	3.4	1.4	1.4
Goethite	0.9	1.1	1.0	1.4	0.9	0.5	0.5	0.4	0.7	1.0
Calcite	0.4	0.9	0.7	1.0	0.6	0.6	0.5	1.5	0.6	0.6
Halite	0.3	0.3	0.3	0.4	0.4	0.3	0.2	0.4	0.2	0.2
Sylvite	0.0	0.1	0.0	0.0	0.1	0.0	0.1	0.0	0.0	0.1
Total Non-Clays	63.0	65.8	59.1	57.2	63.4	57.1	57.7	64.2	68.8	61.8
<b>CLAYS</b>										
Smectite	16.3	11.3	21.0	22.0	12.3	20.1	19.1	16.7	16.0	16.3
Halloysite	8.9	10.9	10.1	13.8	11.4	11.2	10.3	6.2	5.3	8.9
Glauconite	2.5	7.5	5.3	4.0	5.4	4.4	4.3	4.4	4.6	2.5
Biotite	2.5	1.2	2.2	2.4	1.8	2.0	1.9	1.9	1.1	2.5
Dickite	3.9	1.7	0.0	0.0	2.4	3.4	1.4	1.2	1.3	3.9
Palygorskite	1.4	1.6	2.2	0.7	0.0	0.5	1.2	2.5	0.6	1.4
Muscovite	1.6	0.0	0.0	0.0	3.0	0.0	1.6	2.5	1.1	1.6
Chlorite	0.0	0.0	0.0	0.0	0.0	0.0	1.5	0.0	0.6	0.0
Kaolinite	0.0	0.0	0.0	0.0	0.3	1.3	0.0	0.0	0.0	0.0
Illite	0.0	0.0	0.0	0.0	0.0	0.0	1.0	0.3	0.5	0.0
Total Clays	37.0	34.2	40.9	42.8	36.6	42.9	42.3	35.8	31.2	38.2
<b>TOTAL</b>	100.0	100.0	100.0	100.0	100.0	100.0	100.0	100.0	100.0	100.0

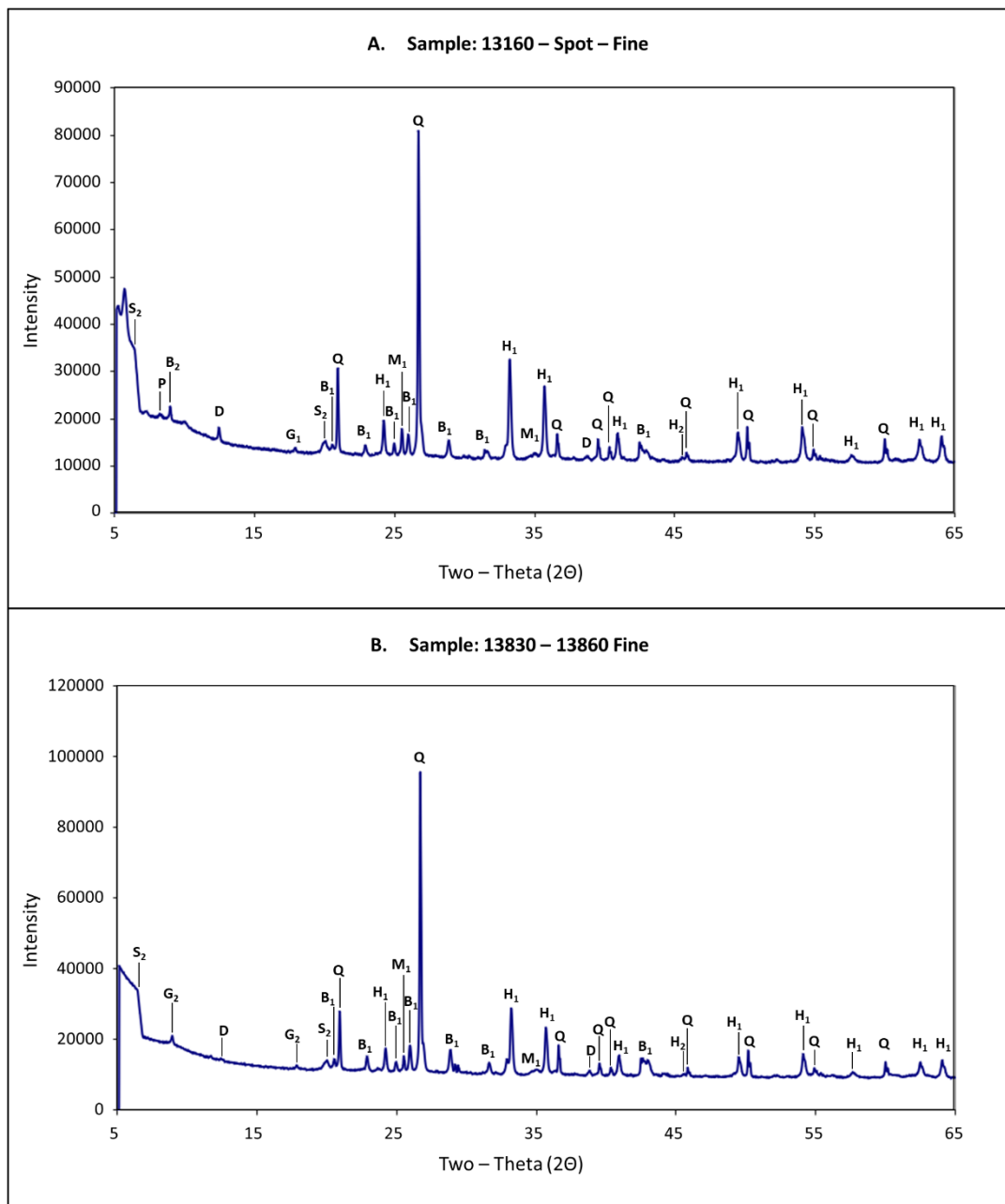


Figure 8.2(A, B): A. XRD results from sample 13,160 Spot – Fine. B. XRD result for sample 13,830 – 13,860 Fine. XRD Legend: B<sub>1</sub> = Barite, B<sub>2</sub> = Biotite, D = Dickite, G<sub>1</sub> = Goethite, G<sub>2</sub> = Glauconite, H<sub>1</sub> = Hematite, H<sub>2</sub> = Halite, M<sub>1</sub> = Microcline, P = Palygorskite, Q = Quartz, S<sub>2</sub> = Smectite.



## 8.4 XRF Analyses

### 8.4.1 Major Elements Geochemistry

Major elements Magnesium (Mg), Silicon (Si), Sulfur (S), Chlorine (Cl), and Calcium (Ca) were selected to support a generalized lithologic interpretation of the cuttings (Figure 8.3). Si and Mg were used as proxies to identify zones of siliciclastics (clay/shale), Cl was used to identify salt, and S and Ca were used to identify any potential anhydrite beds. Element proxies were determined based on the XRD data found by Fredrich et al. (2007).

The cuttings had an average concentration of 2,482 ppm of magnesium (Mg) detected during the XRF analysis. Figure 8.3 indicates that Mg was almost exclusively found within the Neogene strata. In those two intervals, Mg had an average concentration of 9,487 ppm in the Pliocene/Miocene strata and 5,761 ppm in the Miocene strata. Once Cl became the dominant element, the concentration of Mg dropped below the level of detection (<LOD). In the suture zone, Mg was detected in five samples, but the concentration did not exceed more than 1.4% of the sample's overall elemental constituents. Because Mg concentrations was almost non-existent when Cl was the dominant element, Mg can be used to indicate changes in lithology from the Neogene strata to the Louann Salt in this system.

Silicon (Si) was present in all samples. With respect to Cl, the concentration of Si never reached >1.1% when the concentration of Cl was 50% or greater (Figure 8.3). Once

the lithology changed from the upper Louann Salt to the suture zone interval, the concentration of Si fluctuated between 2.6% and 11.2%, with an average of 6.3%. Within the suture zone, the increased amount of siliciclastic material directly reflects increased Si concentrations as Cl concentrations decreased. This trend also continued with several elements of interest elements discussed in the following section.

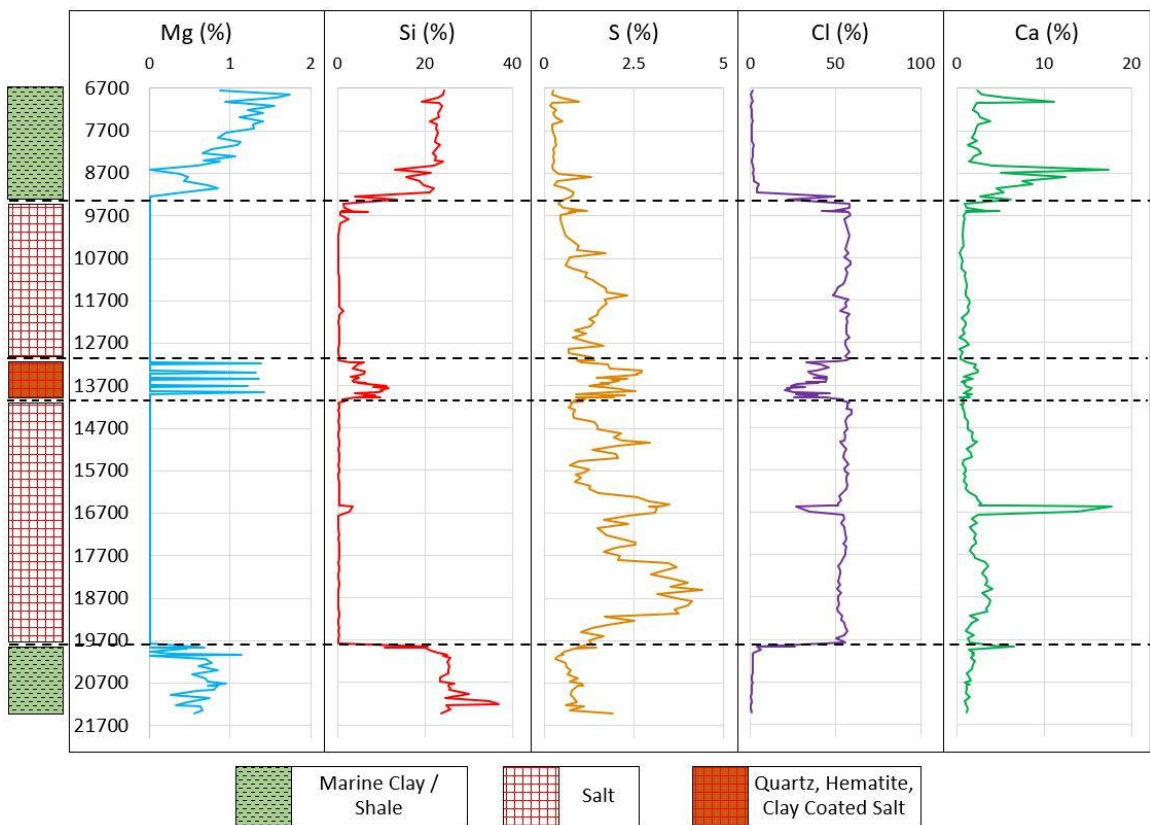


Figure 8.3: Major Elements, XRF graphs of Mg, Si, S, Cl, and Ca in (%). Major Elements with generalized lithology. Black dashed lines represent a change in lithology. Lithology symbols and colors were based on the BakerHughes Atlas of Log Responses.

Chlorine (Cl) concentrations were converted from ppm to percent (%) using Equation 1 for ease of determining where the Louann Salt interval started and ended. The upper and lower contacts of the Louann Salt interval were determined by using a cutoff percentage of 50%. Cl had a minimum concentration of 0.33%, a maximum concentration of 59.5%, and an average concentration of 37.2% in the samples analyzed with the XRF (Figure 8.3). The upper interval of the Louann Salt was determined to be at approximately 2,871 – 2,880 meters (9,420 – 9,450 feet), marked by a Cl% increase from 21.69% to 58.29%. The lower interval was determined to be at 6,026 – 6,035 m (19,770 – 19,800 feet), marked by a decrease in Cl% from 55.98% to 5.41%. Within the Louann Salt interval, a “suture” zone was delineated by a decrease in Cl% from 50.32% to 32.79% at 4,011 m depth (13,160 feet). The suture zone ended at approximately at 4,270 - 4,279 meters depth (14,010 – 14,040 feet), marked by an increase in Cl% from 47.88% to 54.47%.

$$\text{Equation 1.} \quad \textit{Element X} (\%) = \frac{\textit{Element X (ppm)}}{10,000}$$

S and Ca were also present in every sample analyzed, but unlike Si, they did not have an easily discernable trend with respect to Cl. Moving down core, S had an overall increasing trend throughout the samples but fluctuated repeatedly (Figure 8.3). These fluctuations might have been caused by interbedded anhydrite within the Louann. There was no discernable trend to Ca concentrations, as it fluctuated from <1.0% to ~5.0% when salt was the dominant lithology.

#### 8.4.2 Elements of Interest (EOI) – Element Geochemistry

EOI selected for this analysis included Aluminum (Al), Potassium (K), Iron (Fe), Nickel (Ni), Zinc (Zn), Zirconium (Zr), Niobium (Nb) and Barium (Ba) (Figures 8.4 and 8.5). Al, K, Fe, and Zr trended similarly to Si (discussed in the previous section) with respect to Cl (Figure 8.4). They all decreased in concentration when Cl was the dominant element within the Louann interval. The trend for Fe differed slightly in that it reached its highest concentration within the suture zone associated with hematite, and not in the Pliocene – Miocene boundaries above and below the salt.

Zr reported similar geochemical variations with Fe, Al, and K when salt was the dominant lithology (Figure 8.4). Concentrations were increased in the Neogene strata above and below the Louann Salt and reported an increased trend in concentration similar to Fe, Al, and K within the suture zone. Changes were not significant.

Ba and Ni reported a similar trend; they both increased in concentration down core near the suture zone (Figure 8.5). Within the suture zone, both had similar fluctuating spikes and decreases once the suture zone ended. Below the suture zone, Ba and Ni concentrations began to steadily increase fluctuated until the Louann interval ended. Ni was the only element found that has an equivalent trend to Ba.

Zn concentrations reported similar trends only when salt was the dominant lithology (Figure 8.5). Zn reported higher concentrations outside the Louann interval, but the changes were not significant. The highest concentration (281 ppm) was detected at

~5,047 m depth (~16,557 feet), but the concentration significantly decreased at the next sample location.

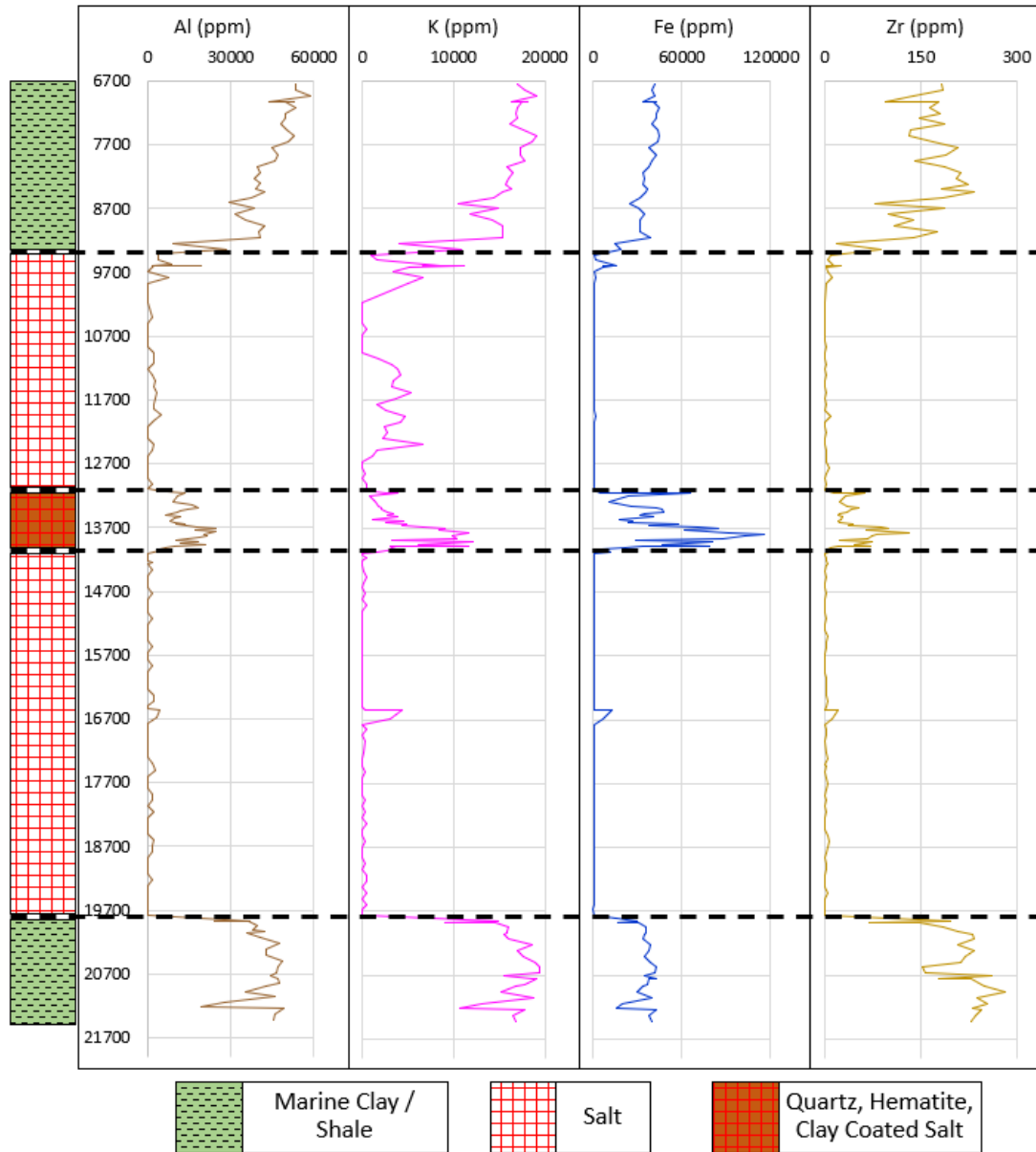


Figure 8.4: Elements of Interest, XRF graphs of Al, K, Fe, and Zr. Black dashed lines represent a change in lithology. Lithology symbols and colors were based on the BakerHughes Atlas of Log Responses.

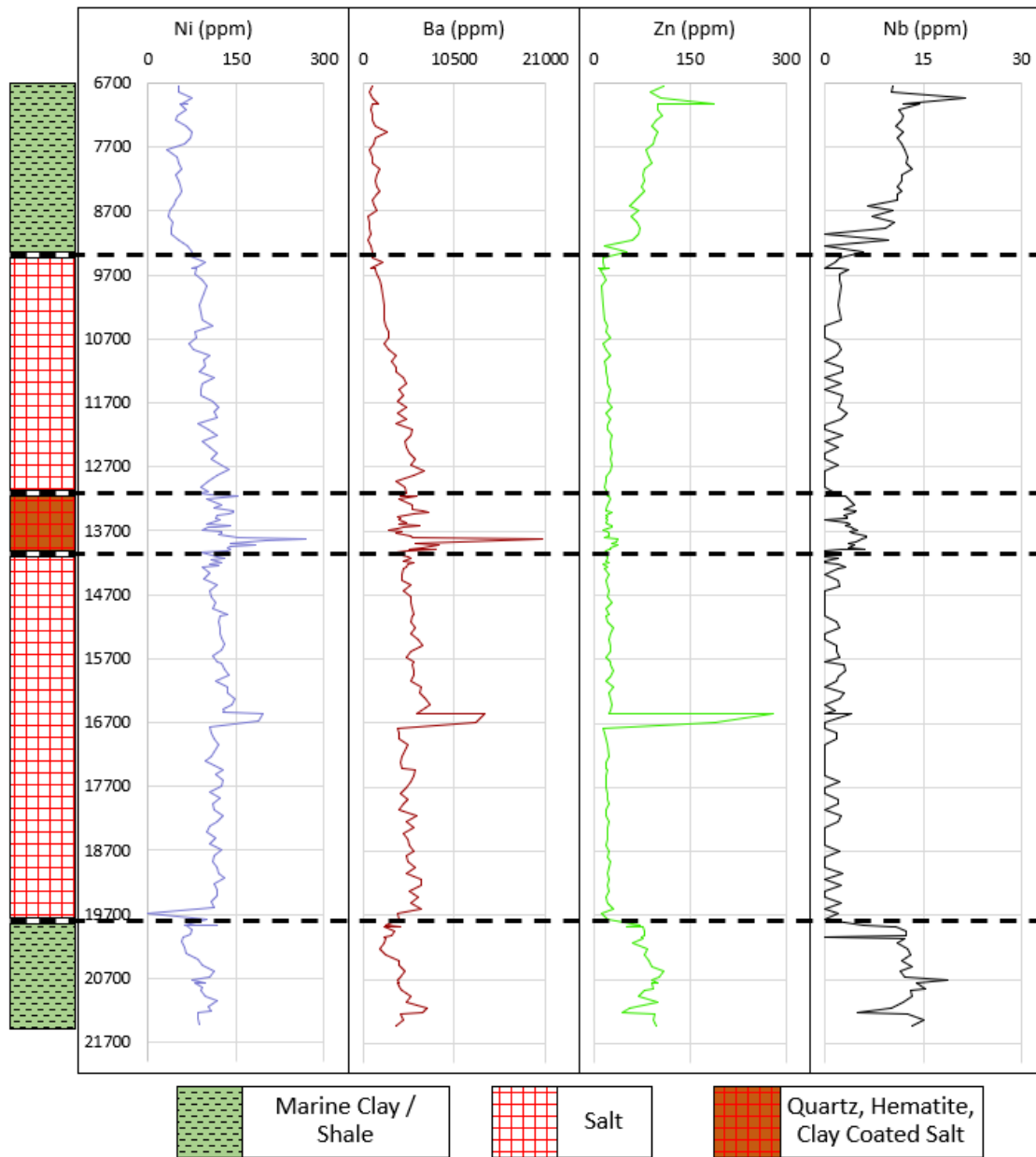


Figure 8.5: Remaining Elements of Interest, XRF graphs of Ni, Ba, Zn, and Nb. Black dashed lines represent a change in lithology. Lithology symbols and colors were based on the BakerHughes Atlas of Log Responses.

Nb had the lowest concentration average of all the EOI, averaging 4.37 ppm. The minimum concentration was <LOD and the maximum concentration (21 ppm) was found in the Pliocene/Miocene strata (Figure 8.5). Nb concentrations were highest in the Neogene strata. Once salt became the dominant lithology, the concentration of Nb fluctuated between <LOD and ~3 ppm. Within the suture zone, the concentration slightly increased to ~5 ppm.

#### 8.4.3 Rare Earth Elements – Element Geochemistry

The rare earth elements (REEs) present within the Louann Salt included Lanthanum (La), Cerium (Ce), Praseodymium (Pr), and Neodymium (Nd) (Figure 8.6). Each REE found within the cutting samples had their highest concentration within the Louann intervals. The concentrations of the REEs do not follow the same trends as the other major elements and EOI. The concentrations fluctuated rapidly through all samples and occasionally fell below the level of detection. Nd had the highest average concentration of 234 ppm in areas where it was detected, and shared a similar trend with Pr (150 ppm average) within the Louann interval. La and Ce reported similar concentrations, averaging 114 ppm and 100 ppm, respectively. Elements La and Ce differ from Pr and Nd by their presence in the Neogene strata.

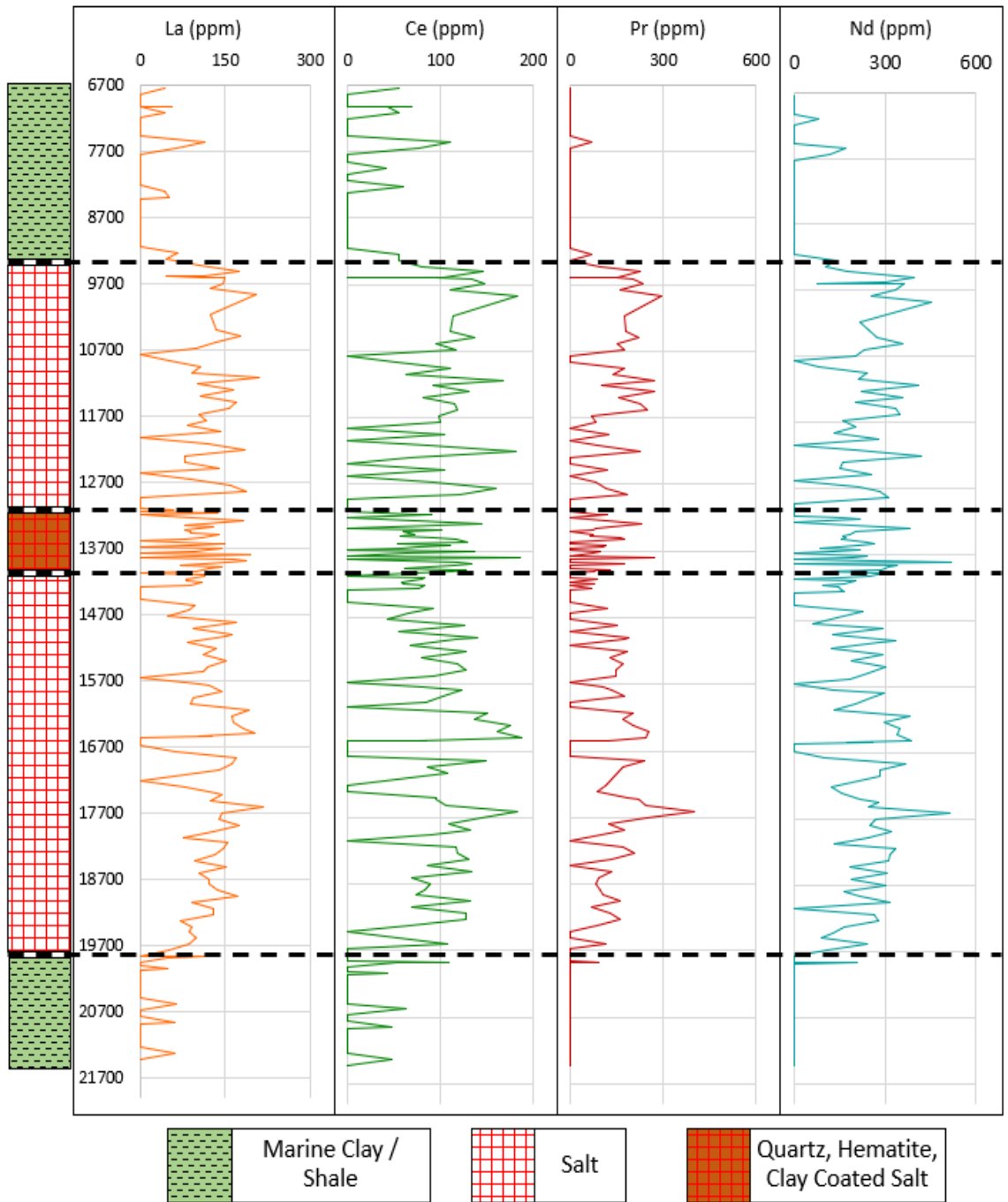


Figure 8.6: Rare Earth Elements, XRF graphs of La, Ce, Pr, and Nd. Black dashed lines represent a change in lithology. Lithology symbols and colors were based on the BakerHughes Atlas of Log Responses.



## 8.5 Cross Plot Analyses

Cross plots were used to show the relationship between specific elements. Major Elements were chosen to create a bulk lithology for the cutting samples. EOI were chosen based on the similarities of their geochemical variations and how well they correlated with one another. REEs were chosen to identify how they correlated with the cutting samples. Elements were plotted against Cl and Fe to determine correlations with the Louann Salt and suture zone, respectively.

### 8.5.1 Major Element Plots

The percentages of Mg, Si, S, and Ca were plotted against Cl to determine how the concentration of each element was affected by the changes in the concentration of Cl (Figure 8.7). The cross plots were divided into three separate areas (double dashed vertical lines) based on the percent of Cl. Zero to 19% identified the Neogene strata above and below the Louann interval. 20% to 49% ppm identified the suture zone interval, and 50% and above identified the Louann Salt interval. Figure 8.7A indicated the relationship between Mg and Cl. When Cl was the dominant element, the concentration of Mg decreased. Si had an inverse relationship with Cl, shown by the negative trend and  $R^2$  value of 0.9491 (Figure 8.7B). Si had the highest concentration within the Neogene strata above and below the Louann Salt. S concentrations fluctuated considerably when Cl was the dominant element (Figure 8.7C). Ca had the least consistent concentration when compared to Cl, shown by the  $R^2$  value of 0.0963. (Figure 8.7D).

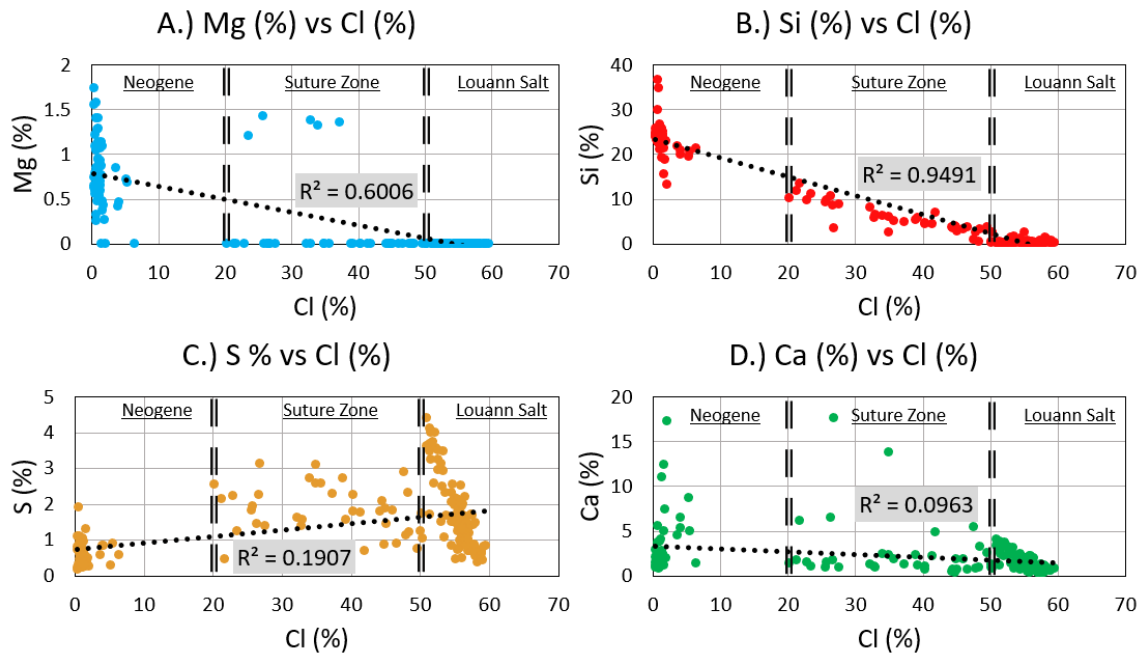


Figure 8.7: Major Elements cross plots from XRF analysis. All cross plots compare elements concentrations in percent: A) Mg vs. Cl; B) Si vs. Cl; C) S vs. Cl; D) Ca vs. Cl. Vertical-dashed lines indicate a change in lithology: Neogene strata (0 – 19% Cl), Suture Zone (20 – 49%), Louann Salt (>50%).

S and Ca were used as proxies to identify any potential anhydrite within the Louann Salt cuttings. Correlations between S and Ca overall were poor (Figure 8.8A). The poor trend was most likely because of outliers, which created two mixing areas within the cross plot. Ca in the upper Miocene/Pliocene units could possibly be due to carbonate material such as calcite, aragonite (fossils), or clays within these units. Further research showed that where the concentration of Cl is  $\geq 50\%$ , S and Ca had a good correlation with a  $R^2$  value of 0.9148 (Figure 8.8B), indicating anhydrite was likely present within the Louann Salt. The correlation between the two elements was not as pronounced within the suture zone as the

Louann Salt (Figure 8.8C), though the data does indicate anhydrite could be in the suture zone as part of the mobilized salt body.

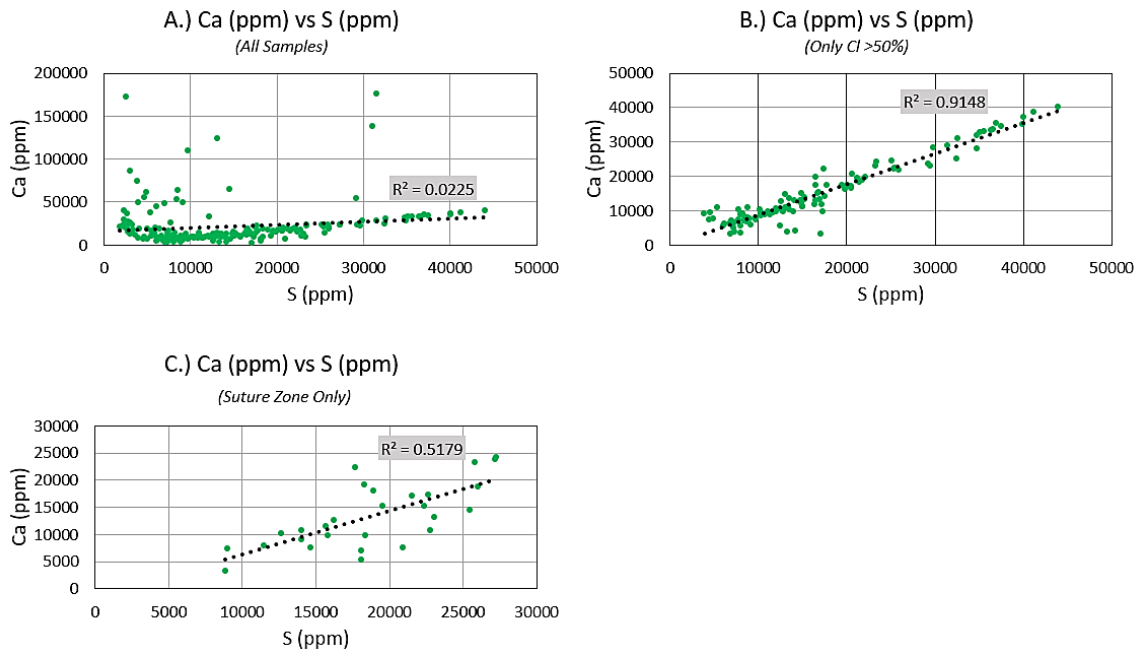


Figure 8.8: Cross plot of elements Ca vs S (ppm): A) Ca vs S – All Samples; B) Ca vs S – Only Cl > 50%; C) Ca vs S – Suture zone only.

### 8.5.2 Elements of Interest Plots

The concentrations of Cl, Si, Al, and K (ppm) were plotted against Fe (ppm) to identify how the suture zone affected the concentrations of each element (Figure 8.9). The cross plots indicated that there were two different mixing lines within each element comparison, identified by each trendline. The first trend showed the element concentrations outside of the suture zone interval (solid-filled point) and the second trend showed the element concentration within the suture zone (white-filled point). Cl is representative of halite, Si is representative of quartz, Al is representative of the clay minerals (smectite and halloysite), and K is representative of microcline and glauconite, and minor amounts of sylvite.

Elements Zn, Zr, and Nb do not represent mixing, so much as dilution of the system by the addition of siliciclastics in the suture zone (Figure 8.10). The concentrations of Cl, Al, K, Si, Zn, and Zr (ppm) were plotted against Nb (ppm) to determine the association Nb had with the cutting samples (Figure 8.11). Each of these cross plots had two separate clusters that could be tied to the lithology of the cutting samples. When the concentration of Cl was >200,000 ppm, the concentration of Nb did not exceed 6ppm. When the concentration of Cl was <200,000 ppm, the concentration of Nb reached 22 ppm. This trend was similar to each of the other elements.

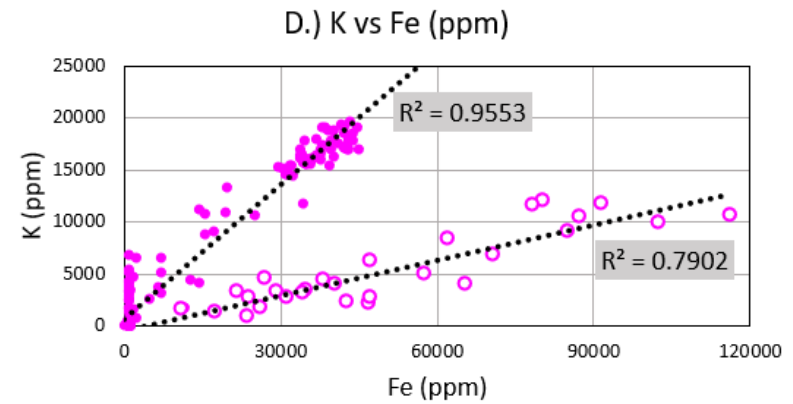
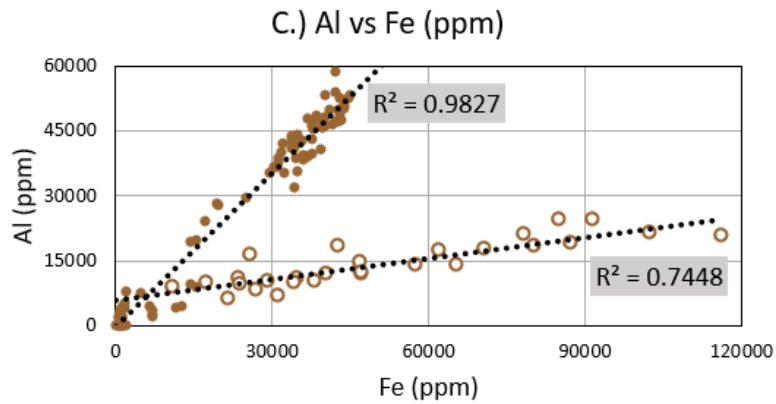
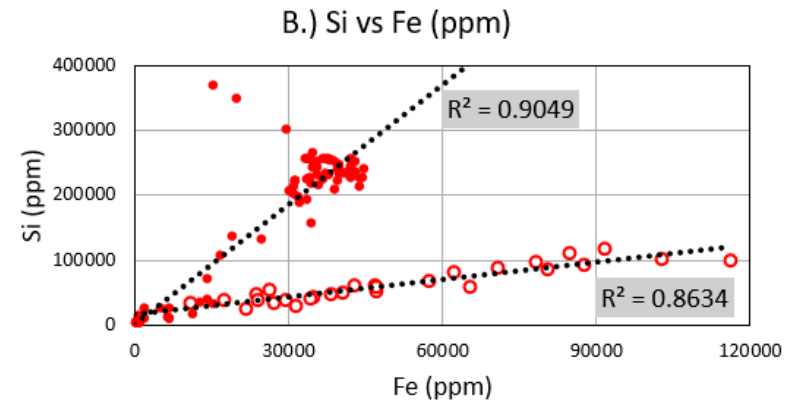
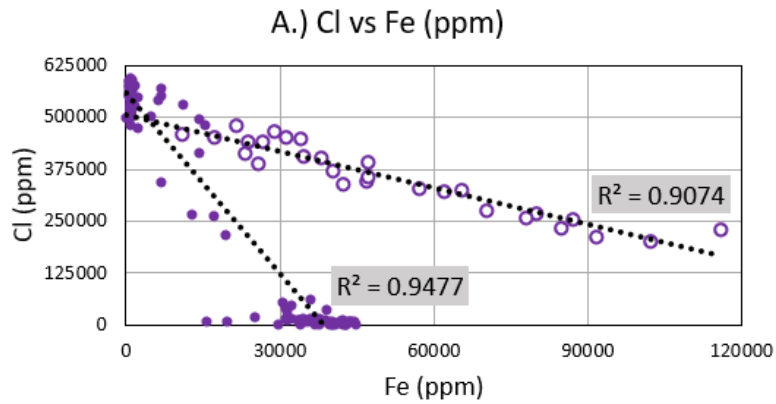


Figure 8.9: Cross Plots of Major Elements (Cl & Si) and Elements of Interest (Al & K) from XRF analysis. All cross plots compare elements concentration in ppm: A) Cl vs Fe; B) Si vs Fe; C) Al vs Fe; D) K vs Fe. Solid filled points represent element concentrations outside the suture zone. White-filled points represent element concentrations within the suture zone.

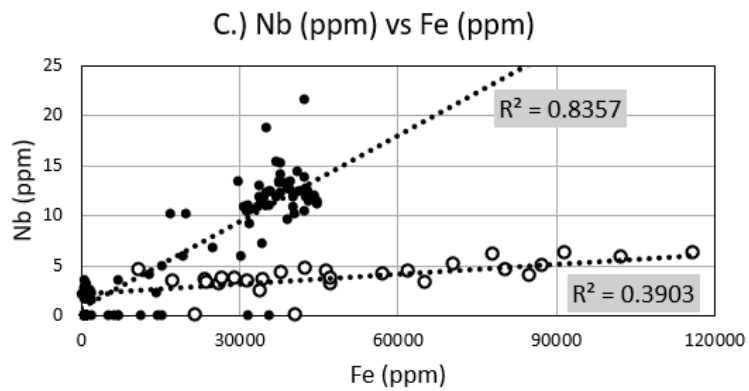
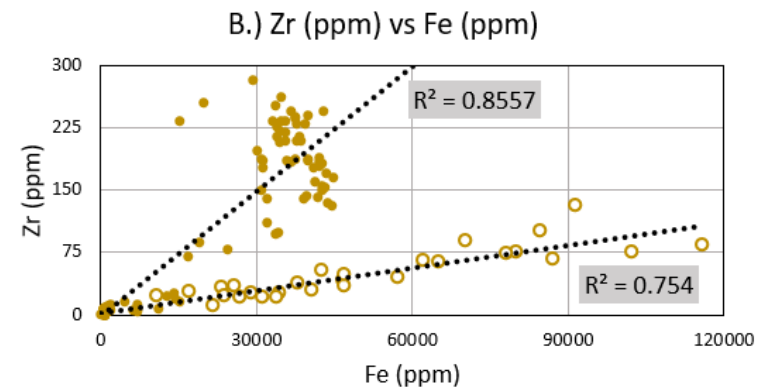
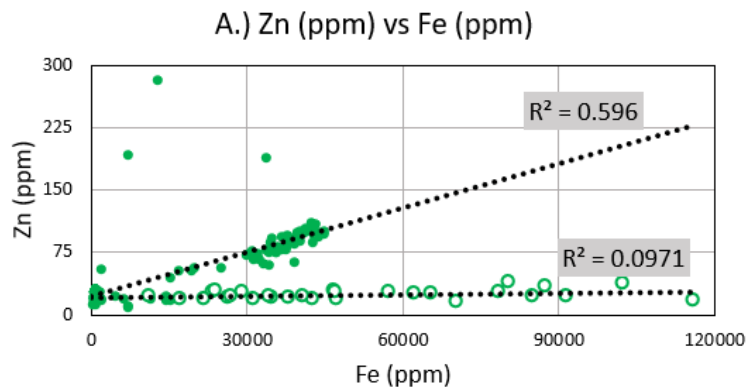


Figure 8.10: Cross Plots of EOI from XRF analysis. All cross plots compare elements concentration in ppm: A) Zn vs Fe; B) Zr vs Fe; C) Nb vs Fe. Solid filled points represent element concentrations outside the suture zone. White-filled points represent element concentrations within the suture zone.

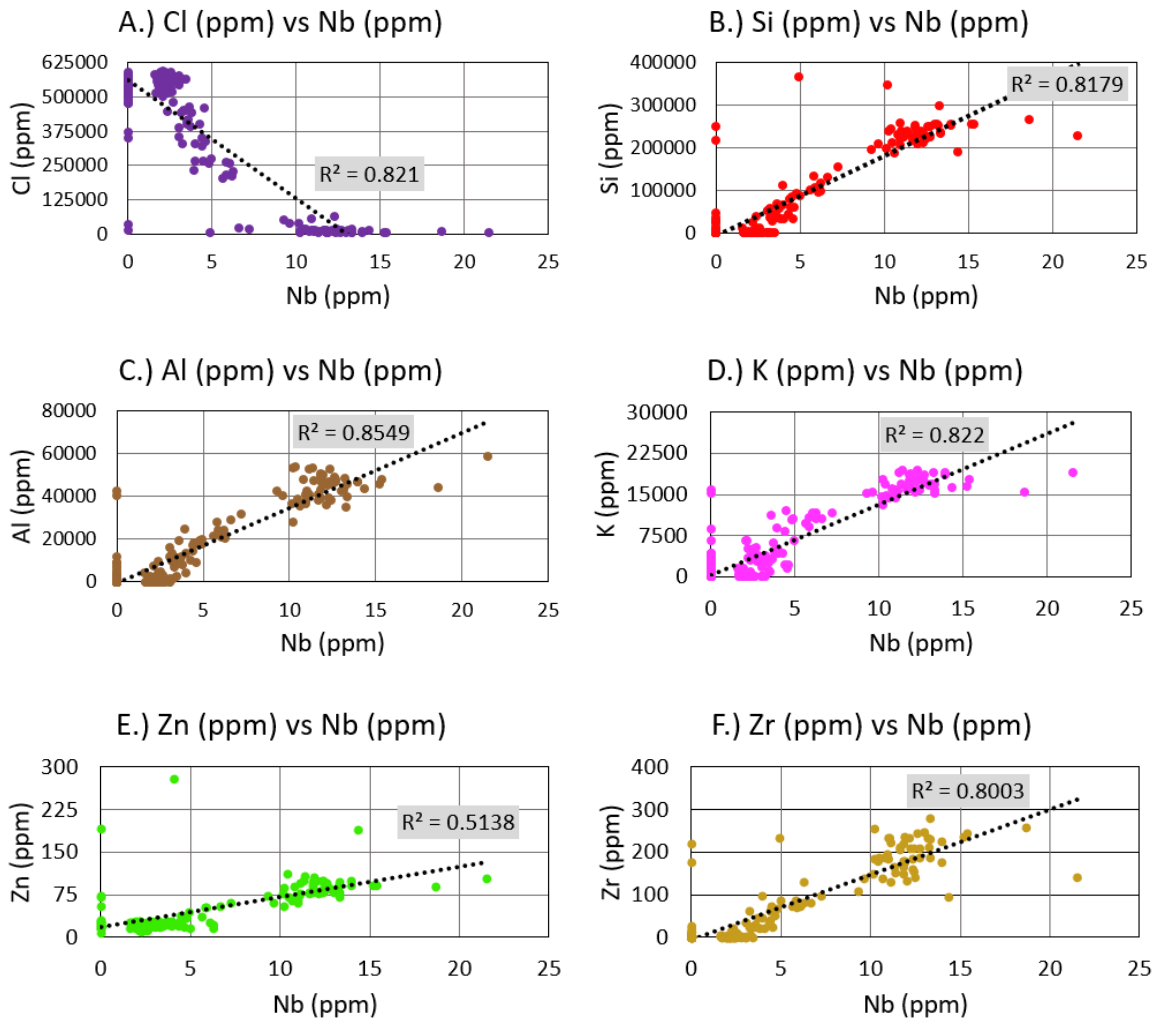


Figure 8.11: Cross plot of Major Elements (Cl & Si) and EOI vs Nb. All cross plots compare element concentrations in ppm: A) Cl vs Nb; B) Si vs Nb; C) Al vs Nb; D) K vs Nb; E) Zn vs Nb; F) Zr vs Nb.

Ba and Ni were selected due to the similar geochemical variations between the elements. The cross plot for Ba vs Ni showed that Ni tends to be present when the concentration of Ba is < 8,000 ppm (Figure 8.12). Ba in seawater has an average concentration of 6 ppb (part-per-billion), but the XRF results indicated that Ba concentrations averaged 4,384 ppm in the cuttings (Johnson et al., 2017). Therefore, the concentration of Ba in the cuttings could not be due to the influence of seawater. XRD results indicated that barite ( $\text{BaSO}_4$ ) was detected in each sample analyzed. This could potentially indicate that the higher concentration of Ba in the Puma Well cuttings may have been caused by contamination from drilling fluid. Also, this could explain the correlation between Ba and Ni (Figure 8.11), as Ni is also used in drilling fluid (DrillingFluid, 2018).

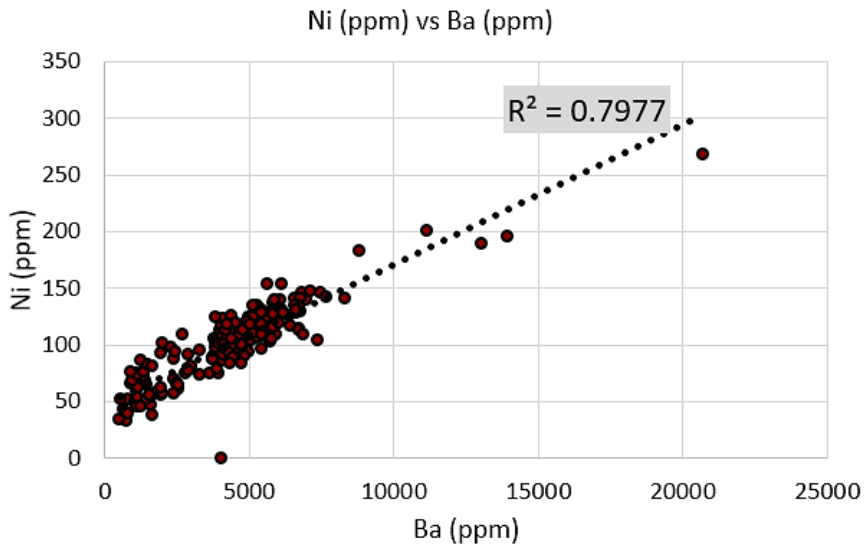


Figure 8.12: Ni vs Ba cross plot comparing Ba and Ni concentrations (ppm). Ba and Ni are used in drilling fluid. Their concentrations could be potentially caused by contamination from drilling fluid.



### 8.5.3 Rare Earth Elements Plots

The concentrations of Lanthanum (La), Cerium (Ce), Praseodymium (Pr), and (Nd) were plotted against Cl (%) to determine their association with the Louann Salt (Figure 8.13). Trendlines of the four cross plots showed a poor relationship/correlation between the REEs and Cl. Although there was not a direct relationship between the REEs and Cl, the REEs concentrations did cluster when chlorine was the dominant element in the system. At depths where the chlorine percent was less than 50%, the concentration of REEs were less prominent. Where chlorine was greater than 50%, the concentrations did not share an increasing or decreasing trend, but their occurrence was more consistent.

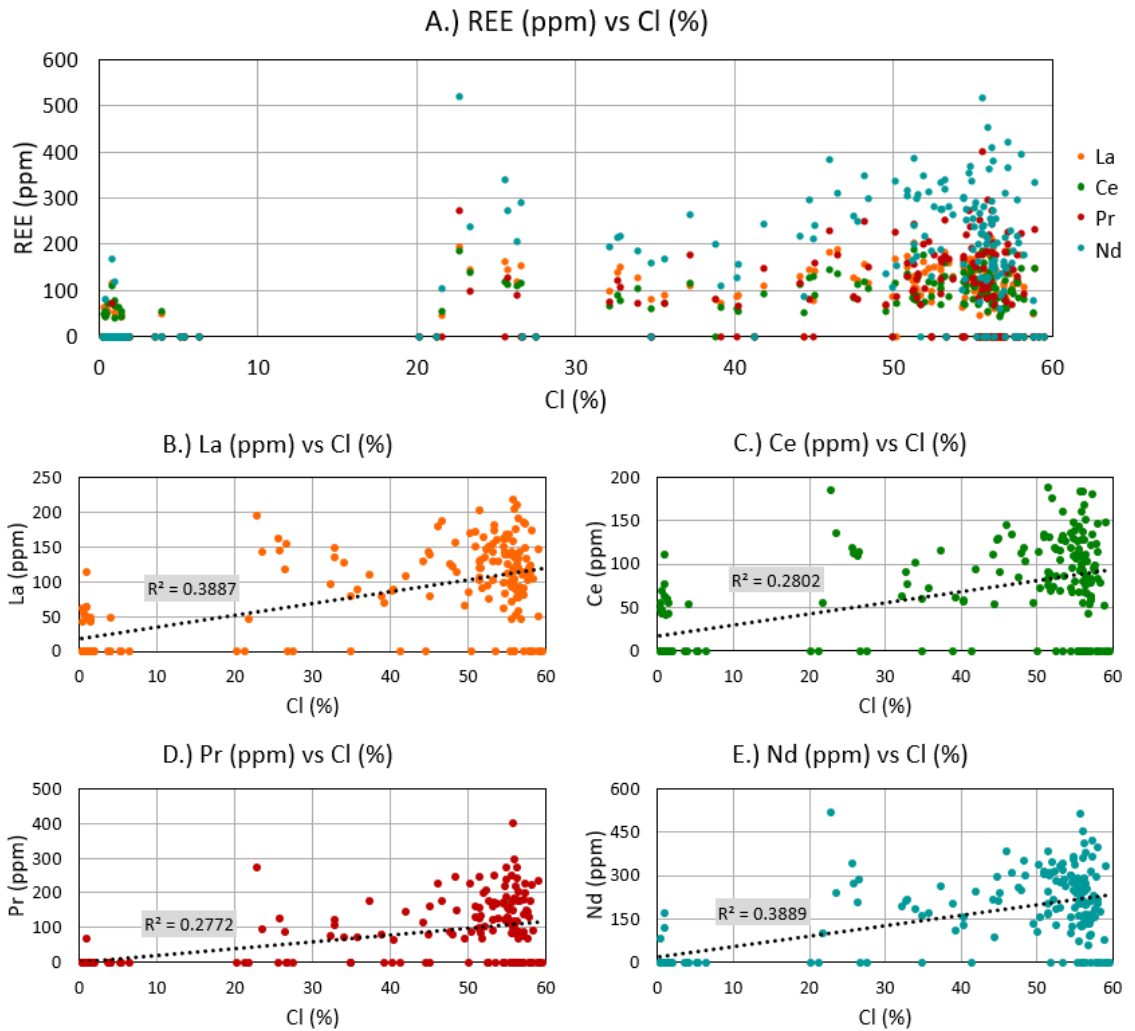


Figure 8.13: Rare Earth Element Cross Plot analysis. REEs are plotted in ppm and Cl is plotted in percent: A) All REEs (ppm) plotted together against chlorine (%); B) La vs Cl; C) Ce vs Cl; D) Pr vs Cl; E) Nd vs Cl.

## 9. DISCUSSION

### 9.1 XRD Analyses

#### 9.1.1 Suture Zone Mineralogy

The XRD analyses on cutting samples from the Puma West GC821-002 well showed that the mineralogical composition of the suture zone is primarily quartz, hematite, and a variety of clays. These minerals could have come from the different formations that the salt pierced as the Puma Diapir formed. As the salt migrated upwards into the Neogene strata, sediment was entrained in the salt body within the forming diapir (Figure 8.1). Based on the mineralogy of the suture zone, the lithology is primarily siliciclastic with a high Fe concentration, correlating to hematite ( $\text{Fe}_2\text{O}_3$ ).

The XRD graphs showed that the mineralogy was similar with only slight variations (Appendix E). The variations in the samples were detected between five and 20 two-theta ( $2\theta$ ), and primarily correlated to the clays within the sample. These variations could have been caused by variations in mineral intensities, mineralogy differences, and orientation of the mineral grains in the sample. The orientations of the grains in the side pack could differ slightly between each sample, resulting in the x-rays not reflecting at the proper angle to get an accurate mineralogical reading.

The change in mineralogy from salt to the quartz, hematite, and clays within the suture zone can be also confirmed with the results of the XRF analysis. With respect to Fe, the concentration of Cl decreased and the concentration of Si, Al, and K increased (Figure 9.1), and as the concentration of Fe increased, the concentration of Cl decreased (Figure 9.1A). The rise in concentration of Si is a result of quartz and various clays associated with the suture zone (Figure 9.1B). Clays and microcline identified within the suture zone are also associated with the increase in Al and K (Figure 9.1C and D). The concentration of K could also have come from any possible residual sylvite within the suture zone samples, although, the majority of the salt was dissolved out of the cutting samples before the XRD analysis.

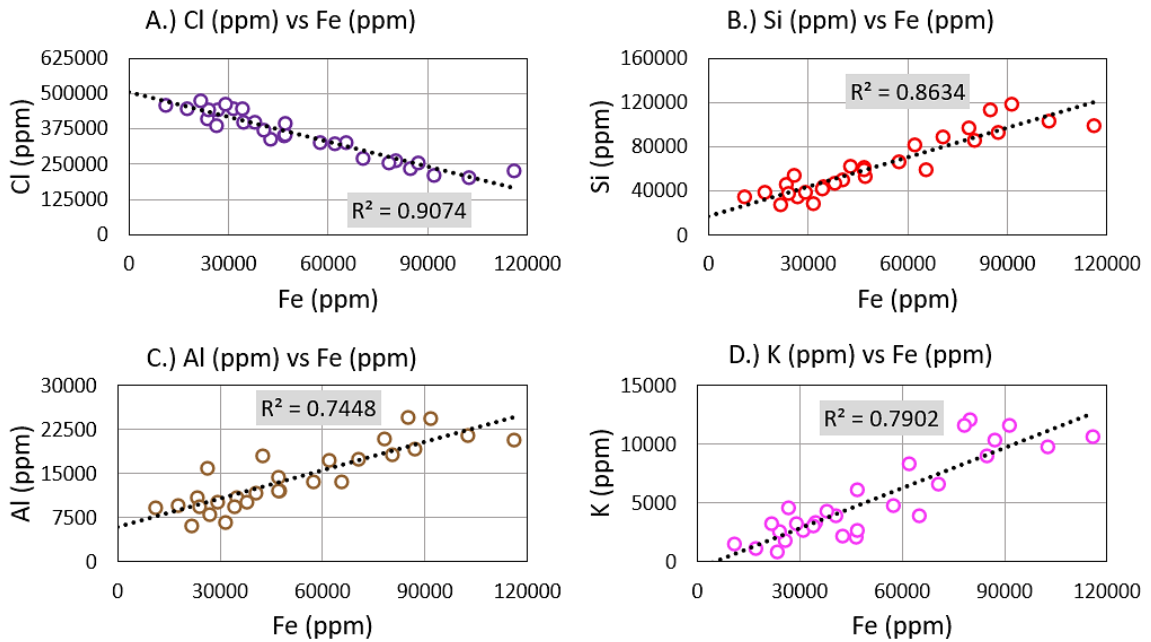


Figure 9.1: Cross plot of the suture zone interval from XRF data. All elements are plotted in ppm: A) Cl vs Fe; B) Si vs Fe; C) Al vs Fe; D) K vs Fe.

## 9.2 XRF Analyses

### 9.2.1 Major Elements

The results of the XRF analysis determined that Cl associated with halite from the Louann Salt was the dominant element within the cuttings. Changes in the concentration of Cl were directly related to the changes in mineralogy in the cuttings; in the suture zone, the concentration of Cl decreased due to the presence of quartz, hematite, and clay minerals, but Cl remained the dominant element in the suture zone. Si was the next dominant major element. In the Louann, its concentration is low in relation to Cl (Figure 8.3). Its presence is likely caused by a small amount quartz or sandy material sourced from the eroded highlands during the deposition of the Louann Salt. Within the suture zone, XRD results indicated that multiple minerals containing Si were present (Table 8.2). Quartz, microcline, and halloysite are the prospective minerals responsible for the presence of Si in the suture zone. The concentration of Si was greatest within the Neogene strata, due to the increased amount of siliciclastics in relation to the Louann Salt and suture zone.

Ca and S were the third and fourth dominant major elements. Together, these elements were used as proxies for potential interbedded anhydrite that could have precipitated in the Louann salt. Correlations made between Ca and S indicated that anhydrite is likely present within the Louann Salt (Figure 8.7) and potentially the suture zone. Anhydrite was not detected in the XRD analysis, but the methods used to isolate the

clays from the salt before analysis may have dissolved residual anhydrite in the cutting samples

Ca had only one major variation in concentration within the lower Louann Salt interval; Ca concentration spiked at ~5,046 m depth (~16,557 feet) from 5.4% to 17.7%, and correlated with a slight increase in S, which could potentially represent an anhydrite bed ~70 meters (~230 feet) thick (Figure 9.2). One of the difficulties associated with locating potential anhydrite beds was due to the sampling interval chosen for the XRF analysis: 27.4 meters (~90 feet). This sampling interval may have been too large to determine approximate locations of anhydrite beds within the salt. Analyzing each cutting packet would have provided a higher resolution sampling interval, but because each packet represented an agglomeration of ~9.1 m (~30 feet) of cutting samples, some of the finer lithologic differences within the salt body would not have been detected.

The concentration of Mg was <LOD for almost the entirety of the upper and lower Louann Salt intervals, except for the five samples within the suture zone interval (Figure 8.3). Expectations at the start of the study were that Mg would share a trend with K and indicate a small presence of the bittern-salt carnallite ( $\text{KMgCl}_6$ ) within the Louann Salt. Due to the absence of Mg in the Louann Salt, there is no indication that carnallite could have been precipitated.

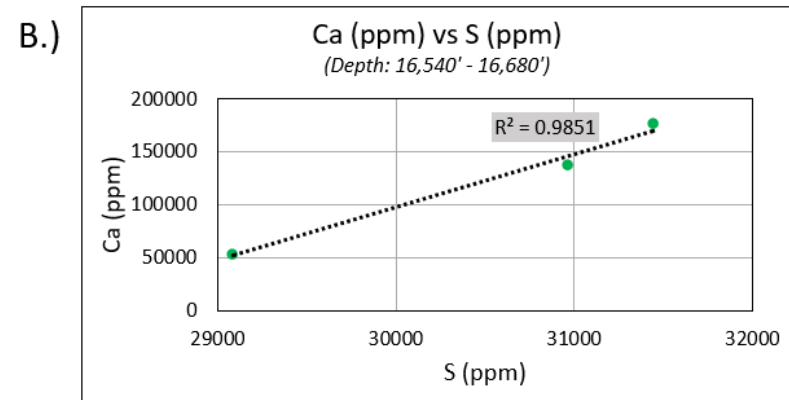
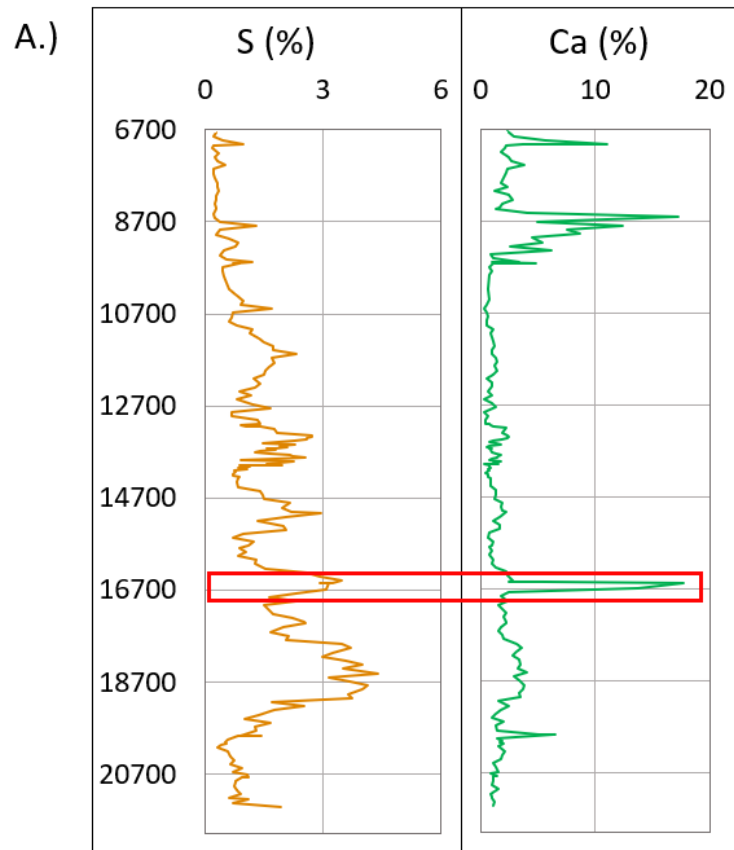


Figure 9.2: Cross plot of Ca vs S (ppm). A) Downcore XRF graphs of S and Ca. Location of possible anhydrite bed (Red box). B) The three points represent XRF samples 16,540 – 16,680. Correlation indicates the possibility of an anhydrite bed associated at these depths.

### 9.2.2 Elements of Interest

Elements Fe, Al, and K were chosen as EOI due to their abundance and variations throughout the cuttings. Fe had an average concentration in the Louann Salt interval of ~940 ppm when the concentration of Cl was <50% (Figure 8.4). This suggests that Fe had little to no presence within halite. In the suture zone interval, the average concentration of Fe significantly increased to ~51,290 ppm. XRD results indicated that the increased concentration of Fe was the result of hematite within the suture zone (Table 8.2).

Al was used to identify clay minerals within the cutting samples. Where the concentration of Cl was >50%, Al had an average concentration of ~980 ppm (Figure 8.4). These data indicate that the Louann Salt has little to no clay material, excluding the suture zone. Within the suture zone, the average concentration of Al increased to ~13,520 ppm. XRD analyses indicated that the increased concentration of Al was the result of clay minerals (smectite and halloysite) and non-clay mineral (microcline) (Table 8.2).

While K is inherent to several siliciclastic minerals, there are zones where Si is low or almost non-existent, such as throughout the salt body. K is also found in sylvite (KCl), which is a known mineral in the salt body based upon the XRD data (residual amount) (Figure 8.4) and the literature (Fredrich et al., 2007). The concentration of K averaged 2,604 ppm above the suture zone and 286 ppm below (Figure 8.4). This could indicate a small presence of sylvite in the upper Louann Salt interval in minor quantities (~<1%) (Figure 8.4). The possibility of the presence of sylvite in the upper Louann Salt over the lower interval is consistent with how bittern salts are the last evaporites to precipitate at



high salinity concentration (Table 9.1). However, because of the fluid nature of the Louann shortly after deposition, these are not the “cap” section of the Louann, rather are mixed throughout the salt body.

Table 9.1. Salinity based classification paragenesis and brine properties based on concentration of seawater (From Warren, 2016).

	Brine Stage	Mineral Precipitate	Salinity (%)	Degree evap.	Water loss (%)	Density (g/cc)
Sea	Normal marine or euhaline	Skeletal carbonate	37 – 37%	1x	0	1.04
Hypersaline	Mesohaline or Vitahaline	Alkaline earth carbonates	3 – 40%	1 – 4x	0 – 75	1.040 – 1.100
	Penesaline	CaSO <sub>4</sub> (gypsum/anhydrite) CaSO <sub>4</sub> + halite	140 – 250% 250 – 350%	4 – 7x 7 – 11x	75 – 85 85 – 90	1.10 – 1.214 1.214 – 1.126
	Supersaline	Halite (NaCl) Bittern Salts (K-Mg Salts)	>350 Extreme and variable	>11x >60x	>90 ≈99	>1.126 >1.290

Hypersaline is defined as >35‰. Biologists working in saline waters use a somewhat different classification of; fresh water (less than 1‰), subsaline (1–3‰), hyposaline (3–20‰), mesosaline (20–50‰), and hypersaline (greater than 50‰). Geohydrologists tend to refer to fresh water as less than 1‰, brackish water as 1–10‰, saline water as 10–100‰, and brine as greater than 100‰.

Zr, Zn, and Nb had the lowest concentrations of the EOI. XRF results show an interesting correlation between these elements. Zr had a very similar trend with Si, Al, K, and Fe (Figures 8.3 and 8.4). Similarities between these trends indicate that Zr is associated with the siliciclastic minerals in the Neogene strata and minerals within the suture zone. Zn followed the same trends, although variations in the suture zone were not as pronounced (Figure 8.5). Nb is often associated with mantle-derived carbonatites and could indicate

the suture zone has contributions from oceanic spreading centers or altered clay minerals with mantle processes (Mitchell, 2015). The Louann Salt would have been one of the first formations affected by spreading center processes as the GOMB was just beginning to open when the salt was deposited. These elements are not native to the salt, but instead were associated with the clays in the Neogene strata and within the suture zone.

### 9.2.3 Rare Earth Elements

Rare earth elements La, Ce, Pr, and Nd are associated with the halite bodies within the Louann Salt because of a greater presence when the concentration of chlorine was between 50 – 60% (i.e., the salt was pure or relatively pure; pure salt has a Cl wt% of 60.7% (WebMineral, 2022)). This suggests that these REEs were either deposited or precipitated concurrently with the Louann Salt. There are several mechanisms that could explain the inclusions of REEs within the salt interval. One possibility is that eroded sediments from the highlands north of the GOMB could have transported these elements. It is known that the Ozark Mountain Highlands consists of the Upper Ordovician-Lower Silurian Cason Shale, and are prolific in REEs and other trace elements (Grosz et al., 1995). As the highlands were weathered and sediment eroded into the GOMB during rifting of the North American and South American Plates, they were transported deep into the basin. The ions were most likely dissolved in the seawater and precipitated during concentration of the paleoseawater. A modern-day analog is the evaporites found in Searles Lake, California. The halite, trona, anhydrites and other evaporite minerals are known to contain abundant

REEs (Lowenstein et al., 2016). They are sourced from the nearby Sierra Nevada granitoids and subsurface hydrothermal springs (Lowenstein et al., 2016).

Another possibility is that the REEs could have been sourced from the generation of oceanic crust during periods of rifting during the Mid-Jurassic. This could have been caused by possible volcanic activity occurring, causing mantle-derived fluids to reach the surface in the GOMB region (Mitchell, 2015). Mantle-derived fluids have the highest concentrations of Lanthanides (REEs) (Mitchell, 2015). As fluids sourced from the mantle are mixing with seawater, REEs and other ions are easily mixed into the system. This would allow for the ions to disperse throughout the basin before or during precipitation of the Louann. More sample locations, coupled with decoupling of the stratigraphic section within the Louann is needed to verify either of these hypotheses.

The REEs are variable throughout the Louann, and do not necessarily show a direct correlation with a particular rock type. Figure 9.3 shows the cross plot of the REEs (ppm) vs S (ppm). These data show that the REEs tend to be more frequently present when the concentration of S is less than 25,000 ppm. This may be due to changes in seawater chemistry throughout precipitation by addition of freshwater, or potential dissolution and reprecipitation of the salt bodies. More information on the halite crystals is needed, such as strontium isotopes to determine water source, or SEM or thin section of salt crystals to determine primary or secondary textures.

Though the concentrations fluctuate and do not have a defined correlation at specific depths, there are concentrations of REEs that could be significant enough to be considered for economic profitability. Because the REEs are within a body of salt, dissolution mining would be the most cost-effective method used for extraction.

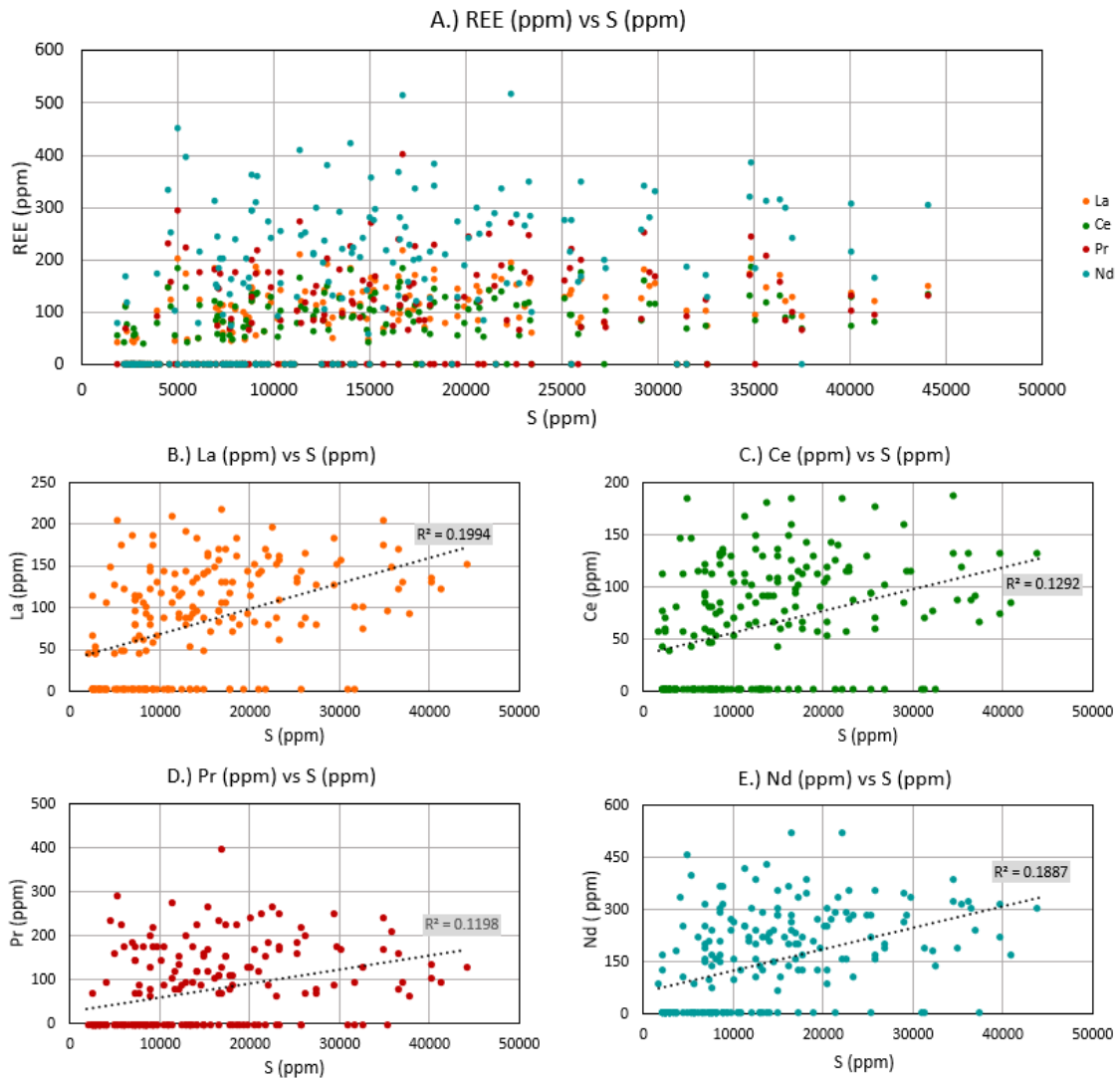


Figure 9.3: Cross plots of REEs from XRF analysis. All cross plots compare elements concentration in ppm: A) All REEs vs S; B) La vs S; C) Ce vs S; D) Pr vs S; E) Nd vs S.

### 9.3 Suture Zone Hypothesis

Suture zones form at the contact between two or more bodies of allochthonous salt. Understanding the formation of suture zones and suture terminology have been comprehensively reviewed and expanded by researchers such Dooley et al. (2012), Weijermars (2015, (B)), and Bouroullec and Weimer (2017). When drilling for hydrocarbons below salt structures, identifying and avoiding sutures is an important aspect when planning deepwater wells. The sediment entrained in salt may contain over-pressured or under-pressured pore fluids. Pore fluid may cause risks such as kicks (when over-pressured) or loss of circulation (when under-pressured) (Weijermars, 2015, (B)). Despite the risks associated with drilling through suture zones, few studies have been published on the formation of suture zones and their unique characteristics.

To develop an improved understanding of the suture zone within the Puma Well cuttings, a hypothesis was developed to answer the following questions: How did the suture zone form? How did the sediment become entrained in the suture zone? What are the possible sources for the minerals in the Puma Well suture zone? The cuttings offer a small window as to what minerals and elements are within the suture zone, but because the cuttings do not represent continuous data, the full extent of suture zone properties is not present.

### 9.3.1 Suture Zone Formation

The suture zone present in the Puma Well cuttings is located within the Puma Diapir (Figures 3.1 – 3.3), but it is probable that the suture did not form within the Puma Diapir due the incorporation of siliciclastics within this zone. If the suture formed within the diapir, the mineralogy would be primarily halite and other evaporitic minerals. Rather, it most likely formed beneath the Neogene strata, followed by salt remobilization, forming the diapir.

The Puma Diapir could have formed one of two ways, either as an allosuture or autosuture. An allosuture would likely form as two separate allochthonous salt bodies collided (Figure 9.4). These salt bodies are sourced from separate diapirs, then continued migration of the salt causes collision. During the collision, one salt sheet tends to override the other, generally because the overriding salt sheet contains more salt (more buoyant; less dense) or lies farther updip, termed an asymmetric allosuture (Dooley et al., 2012). When there is no overriding salt body, a symmetric allosuture forms (Figure 9.5). Continued flow of salt toward the suture from both sides inflates the salt sheets and transports the roofs toward one another. Allosutures can be complexly deformed, caused by salt sheets flowing at different rates and in different directions (Weijermars, 2015 (A)).

As an autosuture, the allochthonous salt body could have formed by internal folding and disruption of the original contact surface between the salt sheet and its overlying sediment veneer (Weijermars, 2015 (A)). Autosutures can form in one of two ways: overriding or encircling (Dooley et al., 2012). Overriding auto sutures form from the one

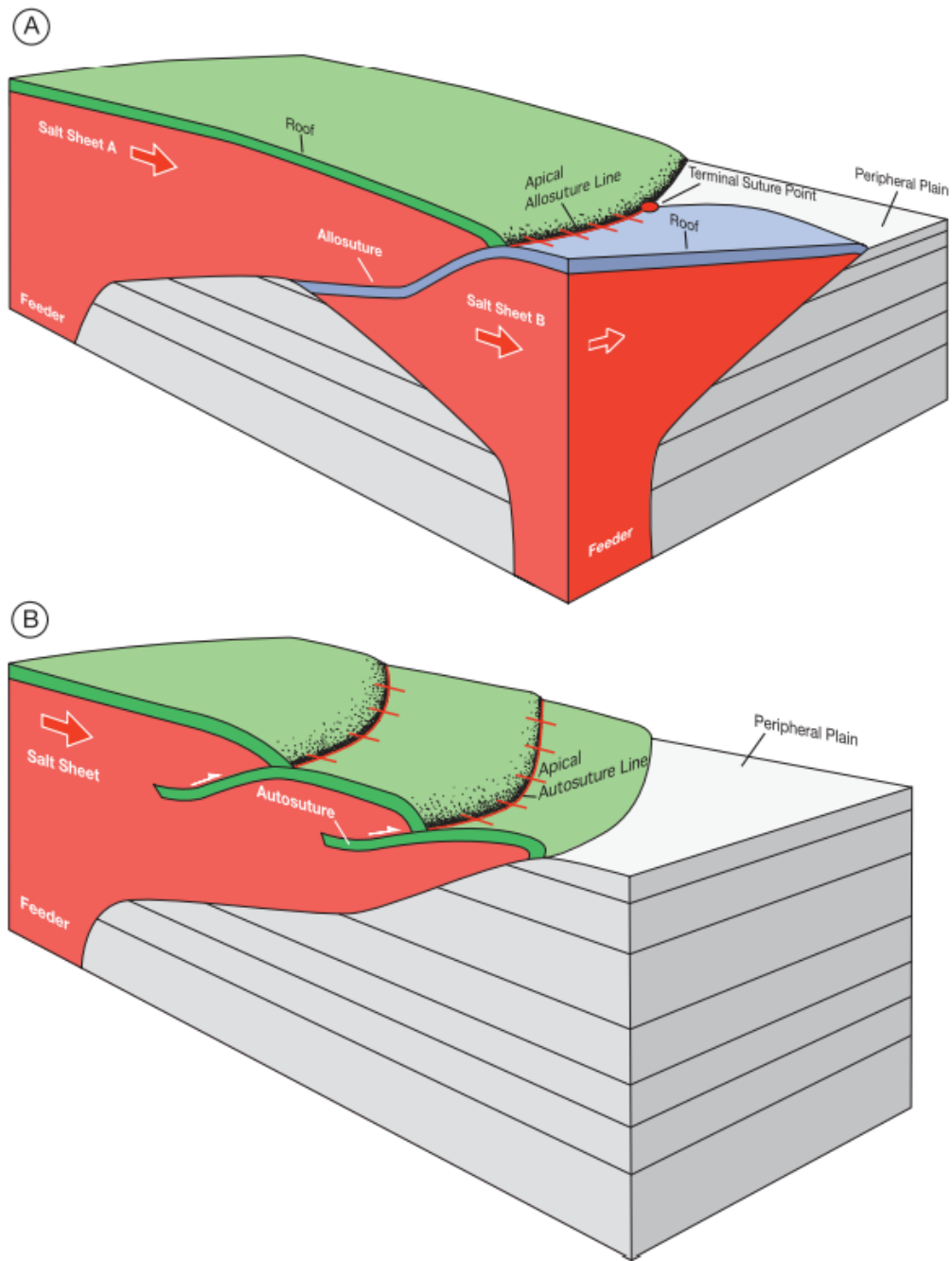


Figure 9.4: Block diagrams showing the characteristics of allosutures and autosutures. A) Allosuture forms from coalescence of two split sheets sourced from different feeders. B) Autosuture forms between two lobes of the same salt sheet moving at different speeds or in different directions (From Dooley et al., 2012).

body of salt overriding itself cause by the salt body moving at different speeds or two separate speeds (Figure 9.4). Encircling autosutures form by a body of salt separating to bypass an obstacle (Figure 9.6). After the suture zone within the salt body formed, the salt would likely have been remobilized due to differential loading and the resulting in the suture zone being incorporated into the diapir as it formed.

The suture zone within the Puma well could have formed as allosuture prior to the diapirism that formed the Puma Diapir, based on the decrease in salt content and increase of siliciclastics seen in the XRD and XRF results (Table 8.2 and Figure 8.7). The sutures seen in Figures 9.4A and 9.5 are at an inclined angle due to the collision of two allochthonous salt bodies. The decreased amount of salt within the suture zone is likely due to the increased amount of siliciclastics that were shed off the overlying formation (Dooley et al., 2012). In contrast, the sutures formed from autosutures are a result of different flow rates or encountering an obstacle (Figures 9.4B and 9.6). Based on how autosutures form, it is possible that the amount of salt within the suture zone would not decrease to the same degree as a suture zone formed from an allosutures. Also, there is no evidence that there is such an obstacle in the region to have caused an autosuture to form. To reach a definitive conclusion, the origin of the allochthonous salt would need to be determined.



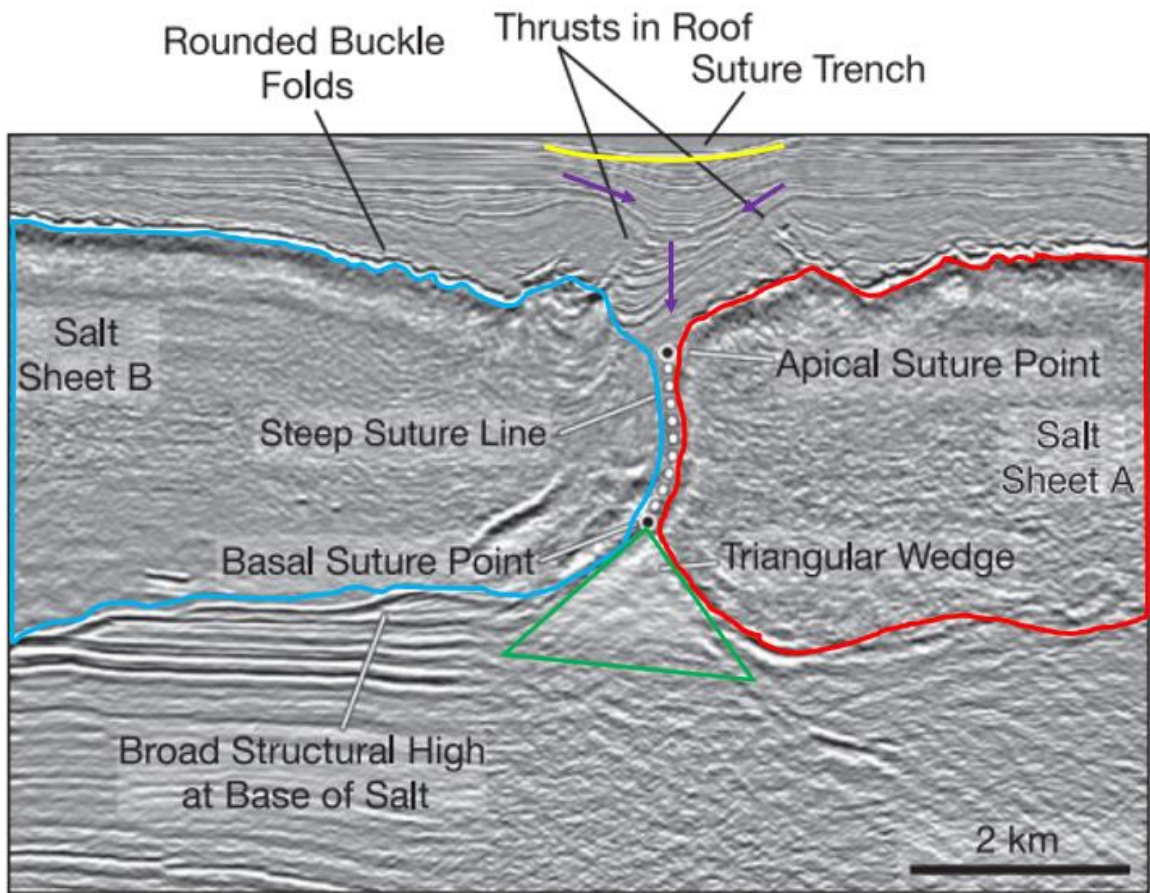


Figure 9.5: Seismic example of a symmetric allosuture (white dots). The suture is nearly vertical due to neither sheet overriding one another. Salt sheet A (red), salt sheet B (blue), sediment moving into suture (purple arrows), triangle wedge (green triangle). (Modified From Weijermars, 2015 (A)).

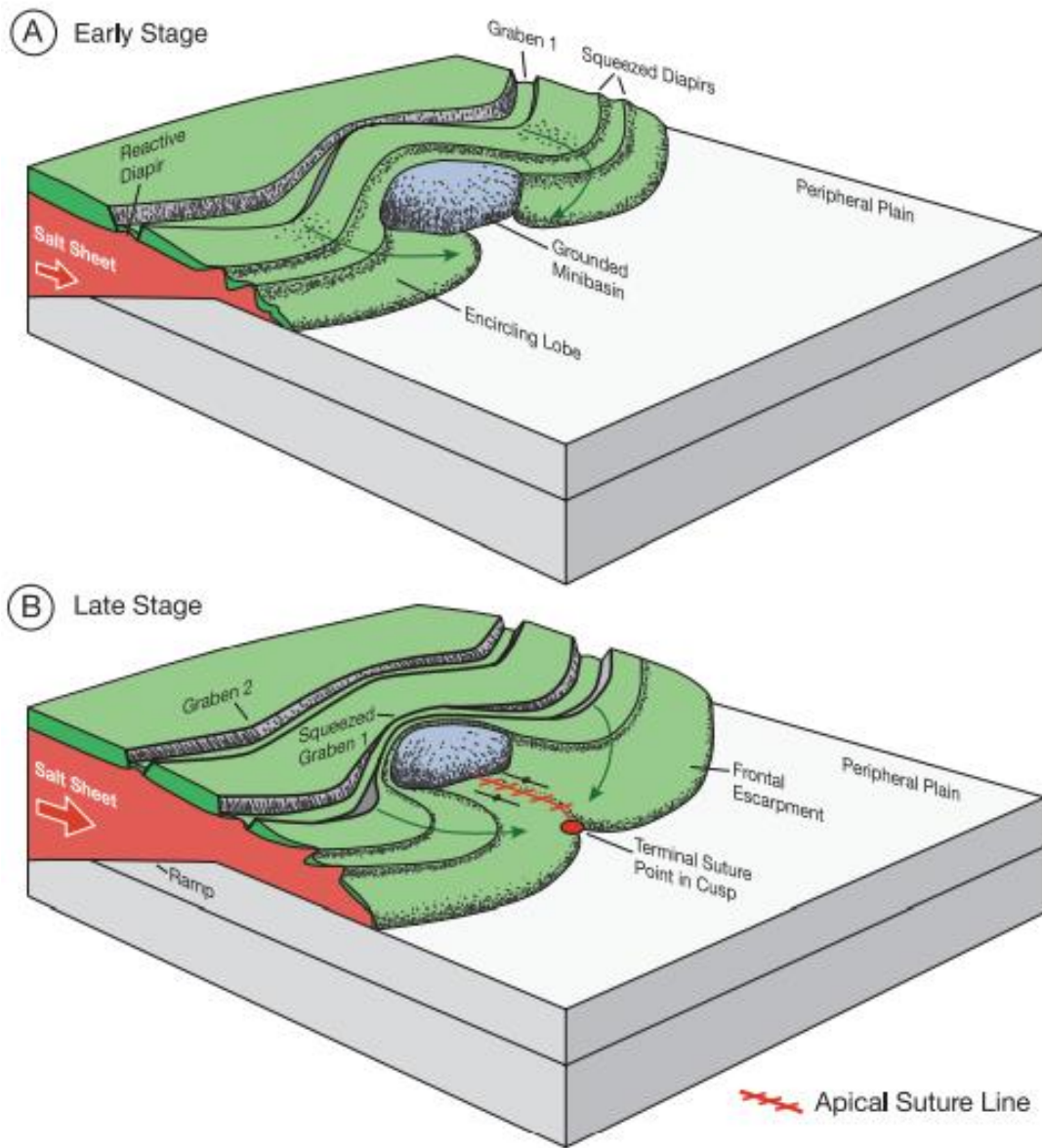


Figure 9.6: Block diagram of an encircling autosuture. A) The advancing salt sheet divided into two lobes to bypass a grounded mini basin. B) The two lobes encircled this obstacle and rejoined on the downslope side (From Dooley et al., 2012).

### 9.3.2 Sediment in the Suture Zone

Following the Dooley et al. (2012) model, sediments that become entrained within suture zones are sourced from the roof of the sheets of allochthonous salt bodies. Sediments extended downward into the salt, trapped along the suture into a “suture trench.” These sediments could have come from the roof of the overriding salt body or the roof of both salt bodies, depending how the two salt bodies contact each another. Sediments at the base of the suture form a triangular shaped wedge (Figure 9.5). This wedge is thought to be a result of the sediment that has traveled through the suture or the sediment beneath each body of salt being pushed together (Weijermars, 2015 (A)).

### 9.3.3 Source of Minerals within the Puma Well Suture Zone

Determining the source of the minerals within the suture zone is difficult without knowing the formation in which the suture zone originally formed. Possible units for the formation of the suture zone extend from the Upper Jurassic Norphlet Formation through the Early Cenozoic (~100+ Ma). Elements such as Zr, Zn, and Nb could be used as indicators of the strata the suture zone formed under. These elements are native to the clays within the suture zone, not the Louann Salt. The strata above the body of salt where the suture zone formed would have had a strong presence of minerals such as hematite, quartz, smectite, halloysite, and glauconite based on the XRD results (Table 8.2).

## 10. LIMITATIONS TO STUDY

At the time of this study, there were no published methodologies that outlined how to accurately determine the mineralogy of a suture zone within an evaporite body using XRD and XRF. The following limitations should be taken into consideration in future studies to further understand the geochemistry of suture zones:

- Accuracy of XRD results were based from the RockJock User's Guide (Eberl, D.D., 2003). Though the XRD results are stated to be an accurate analysis per Eberl, D.D., 2013 with a "degree of fit" of less than 1.00, it is possible that the analyses could be inaccurate with respect to some of the minor elements. Further analyses are needed to verify the complete mineralogy of the suture zone.
- The concentrations of sylvite and other soluble minerals may have been higher prior to dissolving out the soluble fraction of the XRD samples. It would be difficult to state their original concentrations without further analyses.
- After dissolving the soluble fraction of the sample, drying the sample should be completed at a temperature less than 60.0°C. This would prevent any potential gypsum in the sample from converting to anhydrite, leading to a more accurate XRD analysis.

## 11. CONCLUSIONS

The geochemical analyses performed on the Louann Salt cuttings from the Puma West GC821-002 well provided the following conclusions:

1. The Louann Salt interval from this well can be determined to be approximately 3,155 meters (10,350 feet) in thickness, based on XRF analyses reporting the concentration of Cl > 50%.
2. Trends in the elements Cl, Si, Al, K, Zr, Zn, and Nb from XRF analyses can be used to identify the Louann Salt interval and the suture zone when compared with Fe.
3. XRD analyses show that the mineralogy of the suture zone within the Louann Salt is primarily a quartz, hematite, and variety of clays. Barite identified from XRD and nickel identified through XRF are found within the Louann Salt, probably due to contamination from drilling fluid.
4. The mineralogy of the suture zone is similar throughout. The only noticeable variations in mineralogy are varying intensities of clay minerals present within each sample.
5. Rare earth elements are found in concentrations equivalent to those being mined for economic value in hard rock lithologies. The Louann Salt could potentially be used as a source for mining REEs through dissolution mining techniques.

6. Hypothesized model in which the suture zone within the Puma Well formed prior to the Puma Diapir forming. The suture zone could have formed from an allosuture due to the orientation these sutures form and no obstacle present to form an auto suture. The suture would likely have formed below strata with hematite, quartz, halloysite, and smectite between the Late Jurassic – Early Miocene. Origin of the suture is needed to confirm hypothesis.

## 12. RECOMMENDATIONS FOR FUTURE STUDIES

Recommendations for future studies on the Louann Salt and the suture zones within include:

- Continue gathering geochemical data (XRF, XRD, etc.) from other wells in the surrounding area to determine how geochemical variations stated in this study correlate within the Green Canyon Protraction Area / GOMB.
- Increase focus on the rare earth elements to determine if the Louann Salt can be used as a “reserve” or new economically viable source for rare earth elements.
- Use geophysical data and petrophysical data to correlate the extent of the suture zone within the area and potentially the region.

### 13. REFERENCES

- Andrews, D.I., 1960, Louann Salt and Its Relation to Gulf Coast Salt Domes: Gulf Coast Association of Geological Societies Transactions, v. 10, p. 215–240, doi: 10.1306/0bda61df-16bd-11d7-8645000102c1865d.
- BHP Billiton, 2004, BHP Makes Deepwater Discovery with its Puma Well in the GoM, 2004, RIGZONE Empowering People in Oil and Gas, [https://www.rigzone.com/news/oil\\_gas/a/10379/bhp\\_makes\\_deepwater\\_discovery\\_with\\_its\\_puma\\_well\\_in\\_the\\_gom/](https://www.rigzone.com/news/oil_gas/a/10379/bhp_makes_deepwater_discovery_with_its_puma_well_in_the_gom/) (accessed February 2020).
- BOEM., 2022 (A), Geographic Mapping Data in Digital Format: BOEM: Bureau of Ocean Energy Management, <https://www.data.boem.gov/Main/Mapping.aspx> (accessed March 2022).
- BOEM., 2022 (B), Northern GOM Deepwater Bathymetry Grid From 3D Seismic: BOEM: Bureau of Ocean Energy Management, <https://www.boem.gov/oil-gas-energy/mapping-and-data/map-gallery/northern-gom-deepwater-bathymetry-grid-3d-seismic> (accessed March 2022).
- BOEM., 2022 (C), API List Online Query: BOEM: Bureau of Ocean Energy Management, <https://www.data.boem.gov/Well/API/Default.aspx> (accessed April 2022).
- BP, E.& P.I., 2019, Exploration Plan – Puma West GC821 (Public Information Copy): Bureau of Safety and Environmental Enforcement, <https://www.data.bsee.gov/Other/DiscMediaStore/ScanPlans.aspx>. Document Number: GMGWO-WO-BOD-000-08595 (accessed March 2022).
- Bouroullec, R., and Weimer, P., 2017, Geometry and kinematics of Neogene allochthonous salt systems in the Mississippi Canyon, Atwater Valley, western Lloyd Ridge, and western Desoto Canyon protraction areas, northern deep-water Gulf of Mexico: AAPG Bulletin, v. 101, p. 1003–1034, doi: 10.1306/09011609186.



- Buffler, R. T., 1991, Early evolution of the Gulf of Mexico Basin, *in* D. Goldthwaite, ed., *An introduction to central Gulf Coast geology*: New Orleans Geological Society, Louisiana, p. 1–15.
- Badon, C.L., 1975, Stratigraphy and petrology of Jurassic Norphlet Formation, Clarke County, Mississippi: AAPG Bull., v. 59, pp. 377-392.
- Caesar, K.H., Kyle, J.R., Lyons, T.W., Tripathi, A., and Loyd, S.J., 2019, Carbonate Formation in salt dome cap rocks by microbial anaerobic oxidation of methane: *Nature Communications*, v. 10, p. 1–9, doi: 10.1038/s41467-019-08687-z.
- Dooley, T.P., Hudec, M.R., and Jackson, M.P., 2012, The Structure and Evolution of Sutures in Allochthonous Salt: AAPG Bulletin, v. 96, p. 1045–1070, doi: 10.1306/09231111036.
- DrillingFluid, 2018, Metals in drilling muds and cuttings drilling fluid management & disposal: *Drilling Fluid Management & Disposal*, <https://drillingfluid.org/drilling-fluids-waste-management/metals-in-drilling-muds-and-cuttings.html> (accessed June 2022).
- Eberl, D.D., 2003, User's guide to RockJock -- A program for determining quantitative mineralogy from powder X-ray diffraction data: U.S. Geological Survey Open-File Report 2003-78, 47 p.
- Eoff, J. D., R. F. Dubiel, O. N. Pearson, and K. Whidden, 2015, Geologic framework for the assessment of undiscovered oil and gas resources in sandstone reservoirs of the Upper Jurassic–Lower Cretaceous Cotton Valley Group, U.S. Gulf of Mexico region: *Gulf Coast Association of Geological Societies Transactions*, v. 65, p. 93–105.
- Ewing, T.E., and Galloway, W.E., 2019, Chapter - 16 Evolution of the Northern Gulf of Mexico Sedimentary Basin: *The Sedimentary Basins of the United States and Canada*, p. 627–685, doi: 10.1016/b978-0-444-63895-3.00016-4.

- EIA, 2020, Federal Offshore--Gulf of Mexico Field Production of Crude Oil (Thousand Barrels per Day), 2020, U.S. Energy Information Administration, <https://www.eia.gov/dnav/pet/hist/LeafHandler.ashx?n=pet&s=mcrfp3fm2&f=a> (accessed August 2020).
- Forgotson, J. M., 1954, Regional stratigraphic analysis of Cotton Valley Group of upper Gulf Coastal Plain: American Association of Petroleum Geologists Bulletin, v. 38, p. 2476–2499.
- Fort, X., and Brun, J.-P., 2012, Kinematics of regional salt flow in the northern Gulf of Mexico: Geological Society, London, Special Publications, v. 363, p. 265–287, doi: 10.1144/sp363.12.
- Fredrich, J.T., Fossum, A.F., and Hickman, R.J., 2007, Mineralogy of deepwater Gulf of Mexico salt formations and implications for constitutive behavior: Journal of Petroleum Science and Engineering, v. 57, p. 354–374, doi: 10.1016/j.petrol.2006.11.006.
- Grosz, A.E., Meier, A.L., and Clardy, B.F., 1995, Rare Earth Elements in the Cason Shale of Northern Arkansas: A Geochemical Reconnaissance: , p. 1–22.
- Hudec, M.R., and Jackson, M.P., 2007, Terra Infirma: Understanding salt tectonics: Earth-Science Reviews, v. 82, p. 1–28, doi: 10.1016/j.earscirev.2007.01.001.
- Hudec, M.R., Norton, I.O., Jackson, M.P.A., and Peel, F.J., 2013, Jurassic Evolution of the Gulf of Mexico Salt Basin. : AAPG Bulletin, v. 97 (10), p. 1683–1710, doi: <https://doi.org/10.1306/04011312073>.
- Hunt, B., Robinson, D.M., Weislogel, A.L., and Ewing, R.C., 2017, Sediment source regions and paleotransport of the Upper Jurassic Norphlet Formation, eastern Gulf of Mexico: AAPG Bulletin, v. 101, p. 1519–1542. <https://doi.org/10.1306/10171615156>.

- Jacques, J.M., and Clegg, H., 2002, Late Jurassic source rock distribution and quality in the Gulf of Mexico: Inferences from plate tectonic modeling: Gulf Coast Association of Geological Societies Transactions, v. 52, p. 429–440.
- Johnson, C.A., Piatak, N.M., and Miller, M.M., 2017, Barite (Barium), chap. D of Schulz, K.J., DeYoung, J.H., Jr., Seal, R.R., II, and Bradley, D.C., eds., Critical mineral resources of the United States—Economic and environmental geology and prospects for future supply: U.S. Geological Survey Professional Paper 1802, p. D1–D18, <https://doi.org/10.3133/pp1802D>.
- Kehle, R.O., 1988. The origin of salt structures. In: Schreiber, B.C. (Ed.), *Evaporites and Hydrocarbons*. Columbia University Press, New York, pp. 345–404.
- Land, L., Kupecz, J., and Mack, L., 1988, Louann salt geochemistry (Gulf of Mexico sedimentary basin, U.S.A.): A preliminary synthesis: *Chemical Geology*, v. 74, p. 25–35, doi: 10.1016/0009-2541(88)90144-1.
- Lowenstein, T.K., Dolginko, L.A.C., and García-Veigas, J., 2016, Influence of magmatic-hydrothermal activity on brine evolution in closed basins: Searles Lake, California: *Geological Society of America Bulletin*, v. 128, p. 1555–1568, doi: 10.1130/b31398.1.
- Mancini, E. A., R. N. Mink, B. L. Bearden, and R. P. Wilkerson, 1985, Norphlet Formation (Upper Jurassic) of southwestern and offshore Alabama: environments of deposition and petroleum geology: *AAPG Bulletin*, v. 69, p. 881–898.
- Mancini, E.A., B.H. Tew, and R.M. Mink, 1990, Jurassic sequence stratigraphy in the Mississippi interior salt basin of Alabama: *GCAGS Trans.*, v. 40, pp. 521-529.

- Mancini, E.A., and Puckett, T.M., 2002, Transgressive-Regressive Cycles: Application to Petroleum Exploration for Hydrocarbons Associated with Cretaceous Shelf Carbonates and Coastal and Fluvial-Deltaic Siliciclastics, Northeastern Gulf of Mexico: Sequence Stratigraphic Models for Exploration and Production: Evolving Methodology, Emerging Models, and Application Histories: 22nd Annual, p. 173–199, doi:10.5724/gcs.02.22.0173.
- Mann, C.J., and Thomas, W.A., 1964, Cotton Valley Group (Jurassic) Nomenclature Louisiana and Arkansas: TRANSACTIONS—GULF COAST ASSOCIATION OF GEOLOGICAL SOCIETIES, v. 14, p. 143–152.
- Marton, G., and Buffler, R.T., 1999, Jurassic—Early cretaceous tectono-paleogeographic evolution of the southeastern Gulf of Mexico Basin, *in* Mann, P., ed., *Sedimentary Basins of the World*, 4. Elsevier Science B.V, Amsterdam, p. 63–91.
- McGowen, M.K., and Harris, D.W., 1984, Cotton Valley (Upper Jurassic) and Hosston (Lower Cretaceous) Depositional Systems and Their Influence on Salt Tectonics in the East Texas Basin: The University of Texas at Austin. Bureau of Economic Geology Geological Circular 84-5, 41 p.
- Mink, R.M., B.H. Tew, S.D. Mann, B.L. Bearden, and E.A. Mancini, 1990, Norphlet and pre-Norphlet Geologic Framework of Alabama and Panhandle Florida Coastal Waters Area and Adjacent Federal Waters Area: Alabama Geological Survey, Minerals Management Service Cooperative Agreement No. 14-12-0001-30387 through the University of Texas, Austin, Bureau of Economic Geology, Draft Report, 81 p.
- Mitchell, R.H., 2015, Primary and secondary niobium mineral deposits associated with carbonatites: *Ore Geology Reviews*, v. 64, p. 626–641, doi: 10.1016/j.oregeorev.2014.03.010.
- Obid, J.A., 2005, Upper Jurassic Sequence Stratigraphy, Onshore to Offshore Alabama, Eastern Gulf of Mexico: *Gulf Coast Association of Geological Societies Transactions*, v. 55, p. 593–607.

- Pindell, J.L., Graham, R., and Horn, B., 2014, Rapid outer marginal collapse at the rift to drift transition of passive margin evolution, with a Gulf of Mexico case study: *Basin Research*, v. 26, p. 701–725. <https://doi.org/10.1111/bre.12059>.
- Pindell, J.L., and Kennan, L., 2001, Kinematic evolution of the Gulf of Mexico and Caribbean, *in* Proceedings, Gulf Coast Section SEPM Foundation 21st Perkins Research Conference, p. 193–220.
- Pindell, J.L., and Kennan, L., 2009, Tectonic evolution of the Gulf of Mexico, Caribbean and northern South America in the mantle reference frame: An update, *in* James, K.H., Lorente, M.A., and Pindell, J.L., eds., *The Origin and Evolution of the Caribbean Plate: Geological Society of London Special Publication 328*, p. 1–55.
- Rueda-Gaxiola, J., 2003, The origin of the Gulf of Mexico Basin and its petroleum subbasins in Mexico, based on red bed and salt palynostratigraphy, *in* Bartolini, C., Buffler, R.T., and Blickwede, J., eds., *The Circum-Gulf of Mexico and the Caribbean: Hydrocarbon Habitats, Basin Formation, and Plate Tectonics*, American Association of Petroleum Geologists Memoir 79, p. 246–282.
- Salvador, A., 1987, Late Triassic-Jurassic paleogeography and origin of Gulf of Mexico Basin: *AAPG Bull.*, v. 71, p. 419-451.
- Salvador, A., 1991, Triassic-Jurassic, *in* Salvador, A., ed., *The Geology of North America*, v.J: *The Gulf of Mexico*: Boulder, CO, Geological Society of America, p. 131–180. <https://doi.org/10.1130/DNAG-GNA-J.131>.
- Sherkati, S., Molinaro, M., Lamotte, D.F.D., and Letouzey, J., 2005, Detachment folding in the Central and Eastern Zagros fold-belt (Iran): salt mobility, multiple detachments and late basement control: *Journal of Structural Geology*, v. 27, p. 1680–1696, doi: 10.1016/j.jsg.2005.05.010.
- Stewart, F. H., 1963. Data of geochemistry, Chapter Y, marine evaporates. Geological Survey of America, Professional Paper 440-Y.

Swain, F. M., 1944, Stratigraphy of Cotton Valley beds of northern Gulf Coastal Plain: American Association of Petroleum Geologists Bulletin, v. 28, p. 577–614.

Tew, B.H., Mink, R.M., Mann, S.D., Bearden, B.L., and Mancini, E.A., 1991, Geologic Framework of Norphlet and Pre-Norphlet Strata of the Onshore and Offshore Eastern Gulf of Mexico Area: Gulf Coast Association of Geological Societies Transactions, v. 41, p. 590–600, doi: 10.1306/0c9b2119-1710-11d7-8645000102c1865d.

ThermoFisher., 2020, What is XRF (X-ray fluorescence) and How Does it Work? Retrieved September 29, 2020, from <https://www.thermofisher.com/blog/ask-a-scientist/what-is-xrf-x-ray-fluorescence-and-how-does-it-work/>

Wade, W.J., and Moore, C.H., 1993, Jurassic Sequence Stratigraphy of Southwest Alabama: Gulf Coast Association of Geological Societies Transactions, v. 43, p. 431–443.

Warren, J.K., 2016, Evaporites., p. 1–1813, doi: 10.1007/978-3-319-13512-0.

Warsitzka, M., Kley, J., & Kukowski, N. (2013). Salt diapirism driven by differential loading — Some insights from analogue modelling. *Tectonophysics*, 591, 83–97. doi: 10.1016/j.tecto.2011.11.018

WebMineral, 2022, Halite Mineral Data, <http://www.webmineral.com/data/Halite.shtml#.Yl39fSjMLcs> (accessed April 2022).

Weiland, R.J., Adams, G.P., McDonald, R.D., Rooney, T.C., and Wills, L.M., 2008, Geological and biological relationships in the Puma appraisal area: From salt diapirism to Chemosynthetic Communities: All Days, p. 1–16, doi: 10.4043/19360-ms.

Weijermars, R., 2015 (A), Analytical models of suture formation in salt canopies for safer well planning: *Tectonophysics*, v. 640-641, p. 1–19, doi: 10.1016/j.tecto.2014.11.009.

Weijermars, R., 2015 (B), Salt sheet coalescence in the Walker Ridge Region (Gulf of Mexico): Insights from analytical models: *Tectonophysics*, v. 640-641, p. 39–52, doi: 10.1016/j.tecto.2014.11.018.

## 14. APPENDICES

### 14.1 Appendix A – Thermo Niton XL3t GOLDD+ Detectable Elements

Table shows which elements can be detected by using the different calibrations of the Thermo Niton XL3t GOLDD+ handheld XRF. **T.A.G.** = Test All Geo Mode Calibration; **R.E.E.** = Rare Earth Element Calibration; **Min.** = Mining Calibration.

No.	Element	Description	T.A.G	R.E.E	Min.
12	Magnesium (Mg)	Associated with dolomite, carnallite, and clay minerals.	X	X	X
13	Aluminum (Al)	Associated with clay minerals.	X	X	X
14	Silicon (Si)	Associated with quartz and biogenic silica.	X	X	X
15	Phosphorus (P)	Associated with clays through adsorption, and trace element in salts.	X	X	X
16	Sulfur (S)	Associated with anhydrite.	X	X	X
17	Chlorine (Cl)	Associated with salts (halite, sylvite, and carnallite).	X	X	X
19	Potassium (K)	Associated with sylvite.	X	X	X
20	Calcium (Ca)	Associated with anhydrite, dolomite, and limestone.	X	X	X
21	Scandium (Sc)	Potential trace element with respect to evaporites.	X		
22	Titanium (Ti)	Potential trace element with respect to evaporites.	X	X	X
23	Vanadium (V)	Potential trace element with respect to evaporites.	X	X	X
24	Chromium (Cr)	Potential trace element with respect to evaporites. Percentage likely possibly from	X	X	X
25	Manganese (Mn)	Potential trace element with respect to evaporites.	X	X	X
26	Iron (Fe)	Potential trace element precipitated from redox reactions in seawater.	X	X	X
27	Cobalt (Co)	Potential trace element with respect to evaporites.	X	X	X

Continued.



No.	Element	Description	T.A.G	R.E.E	Min.
28	Nickel (Ni)	Potential trace element with respect to evaporites.	X	X	X
29	Copper (Cu)	Potential trace element precipitated from redox reactions in seawater.	X	X	X
30	Zinc (Zn)	Potential trace element with respect to evaporites.	X	X	X
33	Arsenic (As)	Potential trace element with respect to evaporites.	X	X	X
34	Selenium (Se)	Potential trace element with respect to evaporites.	X	X	X
37	Rubidium (Rb)	Potential trace element associated with bittern salt depositional environments.	X	X	X
38	Strontium (Sr)	Potential trace element associated with bittern salt depositional environments.	X	X	X
39	Yttrium (Y)	Potential trace element with respect to evaporites.	X	X	
40	Zirconium (Zr)	Potential trace element with respect to evaporites.	X	X	X
41	Niobium (Nb)	Potential trace element with respect to evaporites.	X	X	X
42	Molybdenum (Mo)	Potential trace element with respect to evaporites.	X	X	X
46	Palladium (Pd)	Potential trace element with respect to evaporites.	X		X
47	Silver (Ag)	Potential trace element with respect to evaporites.	X	X	X
48	Cadmium (Ca)	Potential trace element with respect to evaporites.	X	X	X
50	Tin (Sn)	Potential trace element with respect to evaporites.	X	X	X
51	Antimony (Sb)	Potential trace element with respect to evaporites.	X	X	X
52	Tellurium (Te)	Potential trace element with respect to evaporites.	X		
55	Cesium (Cs)	Associated with clay minerals.	X		
56	Barium (Ba)	Associated with anhydrite deposits.	X	X	X
57	Lanthanum (La)	Potential trace element with respect to evaporites.	X		

Continued.

No.	Element	Description	T.A.G	R.E.E	Min.
58	Cerium (Ce)	Potential trace element with respect to evaporites.	X		
59	Praseodymium (Pr)	Potential trace element with respect to evaporites.	X		
60	Neodymium (Nd)	Potential trace element with respect to evaporites.	X		
72	Hafnium (Hf)	Potential trace element with respect to evaporites.			X
73	Tantalum (Ta)	Potential trace element with respect to evaporites.			X
74	Tungsten (W)	Potential trace element with respect to evaporites.	X	X	X
75	Rhenium (Re)	Potential trace element with respect to evaporites.			X
79	Gold (Au)	Potential trace element with respect to evaporites.	X	X	X
80	Mercury (Hg)	Potential trace element with respect to evaporites.	X		
82	Lead (Pb)	Potential trace element associated with iron deposits.	X	X	X
83	Bismuth (Bi)	Potential trace element with respect to evaporites.	X	X	X
90	Thorium (Th)	Potential trace element with respect to evaporites.	X		
92	Uranium (U)	Associated with clay minerals, specifically black shales.	X		

14.2 Appendix B – Detected Elements from XRF Analysis

Elements that were identified in the XRF analysis and corresponding concentration.

Atomic Number	Element Name	Symbol	Average ppm
12	Magnesium	Mg	2,482.26
13	Aluminum	Al	14,793.95
14	Silicon	Si	77,095.61
15	Phosphorus	P	334.09
16	Sulfur	S	14,100.78
17	Chlorine	Cl	371,520.68
19	Potassium	K	5,991.65
20	Calcium	Ca	21,379.71
21	Scandium	Sc	3.13
22	Titanium	Ti	216.41
23	Vanadium	V	9.53
24	Chromium	Cr	14.73
25	Manganese	Mn	477.74
26	Iron	Fe	18,098.32
27	Cobalt	Co	36.42
28	Nickel	Ni	101.57
29	Copper	Cu	27.12
30	Zinc	Zn	41.74
33	Arsenic	As	2.97
34	Selenium	Se	1.16
37	Rubidium	Rb	53.05
38	Strontium	Sr	220.29
39	Yttrium	Y	0.47
40	Zirconium	Zr	60.75
41	Niobium	Nb	4.37
42	Molybdenum	Mo	3.88
46	Palladium	Pd	1.14
47	Silver	Ag	1.84
48	Cadmium	Cd	2.44
50	Tin	Sn	4.11
51	Antimony	Sb	7.06
52	Tellurium	Te	15.99
55	Cesium	Cs	5.85

Continued.

Atomic Number	Element Name	Symbol	Average ppm
56	Barium	Ba	4,384.05
57	Lanthanum	La	80.81
58	Cerium	Ce	64.45
59	Praseodymium	Pr	74.29
60	Neodymium	Nd	150.47
74	Tungsten	W	35.32
79	Gold	Au	6.77
80	Mercury	Hg	7.42
82	Lead	Pb	14.43
83	Bismuth	Bi	7.27
90	Thorium	Th	13.00
92	Uranium	U	0.97

14.3 Appendix C – XRF Data

Depth (ft)	Zr (ppm)	Zn (ppm)	Ni (ppm)	Fe (%)	Nd (ppm)	Pr (ppm)	Ce (ppm)	La (ppm)	Ba (%)	Nb (ppm)	Ca (%)	K (%)	Al (%)	Si (%)	Cl (%)	S (%)	Mg (%)
6750	181.75	110.23	52.35	4.21	0.00	0.00	55.68	43.42	0.11	10.37	2.34	1.70	5.36	24.41	1.43	0.27	0.87
6840	183.98	88.11	51.29	4.01	0.00	0.00	0.00	0.00	0.08	10.23	2.94	1.78	5.34	24.08	0.42	0.22	1.74
6930	140.01	104.54	74.88	4.20	0.00	0.00	0.00	0.00	0.11	21.50	5.62	1.90	5.86	22.87	0.65	0.46	1.58
7035	177.32	98.94	53.52	4.08	0.00	0.00	42.26	0.00	0.11	11.87	2.27	1.76	4.97	23.28	0.51	0.22	1.10
7030	154.79	100.92	68.31	4.26	0.00	0.00	69.80	55.13	0.14	12.37	3.71	1.82	5.27	22.83	0.62	0.27	1.04
7020	95.54	187.63	57.90	3.36	0.00	0.00	0.00	0.00	0.18	14.35	11.08	1.63	4.38	19.20	1.29	0.97	0.93
7110	164.53	99.67	65.47	4.47	80.87	0.00	55.00	43.50	0.09	11.33	2.12	1.69	5.34	23.89	0.43	0.18	1.55
7200	179.68	105.93	48.81	4.27	0.00	0.00	0.00	0.00	0.10	11.87	1.78	1.68	4.98	23.52	0.58	0.34	1.22
7290	148.18	98.74	47.88	4.24	0.00	0.00	0.00	0.00	0.11	11.81	2.44	1.70	4.95	22.99	0.72	0.24	1.41
7380	186.96	90.04	64.06	3.99	0.00	0.00	0.00	0.00	0.14	10.80	2.65	1.62	4.80	23.25	0.75	0.30	1.12
7470	134.79	99.37	74.73	4.39	0.00	0.00	0.00	0.00	0.28	11.96	3.83	1.77	5.00	21.05	1.05	0.53	1.41
7560	130.86	95.61	72.36	4.46	168.90	69.99	110.51	114.44	0.14	11.16	2.37	1.91	5.26	22.65	0.89	0.22	1.28
7650	167.98	92.42	62.16	4.36	119.61	0.00	77.04	64.53	0.12	11.79	2.17	1.86	5.08	22.62	0.98	0.23	1.29
7740	207.89	82.41	32.85	3.77	0.00	0.00	0.00	0.00	0.08	12.20	2.02	1.74	4.51	23.07	1.00	0.25	0.95
7860	189.25	87.08	49.99	4.24	0.00	0.00	0.00	0.00	0.11	12.71	1.72	1.73	4.68	22.56	0.96	0.31	0.85
7950	142.01	90.58	52.50	3.95	0.00	0.00	40.82	0.00	0.11	12.47	2.33	1.78	4.57	22.20	1.02	0.32	1.13
8040	187.31	80.09	56.09	3.74	0.00	0.00	0.00	0.00	0.19	13.34	1.22	1.59	3.97	23.35	1.66	0.36	1.09
8130	212.64	77.22	46.72	3.38	0.00	0.00	0.00	0.00	0.16	11.66	2.40	1.66	4.08	22.40	1.40	0.27	0.77
8220	206.90	78.57	51.88	3.44	0.00	0.00	60.22	0.00	0.14	11.67	2.79	1.60	3.83	21.83	1.27	0.28	0.65

Continued.

Depth (ft)	Zr (ppm)	Zn (ppm)	Ni (ppm)	Fe (%)	Nd (ppm)	Pr (ppm)	Ce (ppm)	La (ppm)	Ba (%)	Nb (ppm)	Ca (%)	K (%)	Al (%)	Si (%)	Cl (%)	S (%)	Mg (%)
8310	224.97	75.33	53.88	3.40	0.00	0.00	0.00	44.34	0.16	11.13	1.91	1.56	4.07	22.56	1.36	0.26	1.07
8400	181.89	78.62	56.23	3.67	0.00	0.00	0.00	51.05	0.20	11.80	1.61	1.64	3.90	22.36	0.98	0.28	0.67
8430	232.50	74.47	55.70	3.55	0.00	0.00	0.00	0.00	0.16	11.03	1.35	1.55	4.23	24.10	1.02	0.30	0.88
8520	184.00	65.60	45.87	3.13	0.00	0.00	0.00	0.00	0.11	10.97	4.03	1.45	3.75	22.05	1.19	0.23	0.60
8610	79.40	56.49	45.72	2.48	0.00	0.00	0.00	0.00	0.12	6.62	17.31	1.06	2.92	13.19	2.01	0.26	0.00
8700	187.20	70.33	37.83	3.11	0.00	0.00	0.00	0.00	0.17	10.45	4.98	1.49	3.86	21.27	1.59	0.39	0.37
8790	98.48	59.27	33.67	3.42	0.00	0.00	0.00	0.00	0.05	7.23	12.43	1.17	3.17	15.63	1.65	1.30	0.48
8880	137.99	67.01	42.42	3.21	0.00	0.00	0.00	0.00	0.07	10.60	7.49	1.43	3.54	18.78	1.73	0.38	0.43
8970	109.70	73.33	40.56	3.18	0.00	0.00	0.00	0.00	0.07	9.25	8.66	1.53	4.22	19.63	5.24	0.30	0.72
9060	176.89	71.06	39.09	3.14	0.00	0.00	0.00	0.00	0.08	0.00	4.54	1.53	4.02	21.94	3.61	0.60	0.85
9150	138.28	61.79	51.46	3.90	0.00	0.00	0.00	0.00	0.05	9.62	5.34	1.54	4.05	21.01	3.99	0.83	0.41
9240	18.56	16.64	67.78	1.43	135.16	68.97	55.39	66.40	0.09	0.00	2.62	0.40	0.91	3.84	49.58	0.77	0.00
9330	87.20	51.96	75.06	1.91	102.29	0.00	55.43	45.78	0.10	5.81	6.18	1.08	2.81	13.49	21.69	0.48	0.00
9420	9.08	14.21	72.80	0.09	174.58	93.31	79.12	104.70	0.11	2.36	0.90	0.09	0.41	1.27	58.29	0.39	0.00
9510	5.66	15.51	96.97	0.17	397.22	224.29	146.91	174.68	0.23	1.56	1.10	0.15	0.41	1.47	58.05	0.54	0.00
9580	13.97	16.37	85.79	1.53	299.86	150.60	102.54	114.27	0.12	0.00	3.32	0.86	0.88	3.22	48.44	1.21	0.00
9590	2.71	8.23	75.44	0.69	73.58	0.00	0.00	46.31	0.09	0.00	1.02	0.66	0.19	0.82	55.56	0.77	0.00
9605	3.69	10.49	82.16	0.68	364.07	200.64	134.13	148.87	0.15	2.23	1.07	0.51	0.23	0.70	57.30	0.88	0.00
9600	25.31	22.74	75.34	1.42	244.79	147.36	93.18	108.78	0.13	3.59	4.85	1.12	1.92	7.05	41.89	0.70	0.00
9690	4.09	13.64	80.84	0.09	333.53	232.96	147.56	147.78	0.16	2.20	0.73	0.34	0.00	0.66	59.00	0.45	0.00
9780	12.05	18.84	92.80	0.19	253.57	158.30	110.99	125.08	0.19	2.15	0.93	0.66	0.75	2.62	55.08	0.46	0.00
9870	2.63	12.24	101.12	0.07	452.00	294.84	183.22	204.68	0.20	2.57	0.76	0.51	0.00	0.60	55.97	0.50	0.00

Continued.

Depth (ft)	Zr (ppm)	Zn (ppm)	Ni (ppm)	Fe (%)	Nd (ppm)	Pr (ppm)	Ce (ppm)	La (ppm)	Ba (%)	Nb (ppm)	Ca (%)	K (%)	Al (%)	Si (%)	Cl (%)	S (%)	Mg (%)
10170	0.00	14.70	86.70	0.04	216.16	175.55	114.19	124.34	0.24	2.09	0.61	0.00	0.00	0.20	57.93	0.61	0.00
10410	0.00	17.46	93.69	0.04	273.61	177.87	111.23	133.21	0.25	2.45	0.72	0.00	0.16	0.20	56.37	0.97	0.00
10500	0.00	21.55	108.87	0.05	360.25	219.37	136.57	175.98	0.27	0.00	0.58	0.00	0.00	0.18	56.05	0.91	0.00
10590	0.00	18.43	79.99	0.03	228.79	150.72	95.72	133.14	0.30	0.00	0.31	0.04	0.00	0.18	57.45	1.70	0.00
10680	0.00	26.96	81.57	0.04	201.84	174.41	116.94	98.21	0.30	0.00	0.49	0.00	0.00	0.23	55.47	0.72	0.00
10770	0.00	14.76	69.66	0.04	0.00	0.00	0.00	0.00	0.24	1.92	0.61	0.00	0.00	0.16	58.94	0.67	0.00
10860	3.09	18.29	77.00	0.04	78.88	0.00	51.57	50.25	0.29	2.52	0.55	0.00	0.00	0.19	58.93	0.61	0.00
10950	0.00	26.91	104.87	0.05	238.40	175.76	111.28	105.27	0.38	1.89	0.57	0.00	0.22	0.22	55.69	0.80	0.00
11040	0.00	16.18	95.55	0.05	212.52	137.28	62.74	91.25	0.33	0.00	1.04	0.18	0.21	0.27	57.09	1.20	0.00
11130	3.03	18.04	98.13	0.05	410.45	272.46	167.87	210.10	0.38	2.69	0.89	0.32	0.22	0.36	56.29	1.13	0.00
11220	0.00	18.34	87.96	0.05	222.41	98.88	92.44	102.27	0.37	2.81	1.01	0.39	0.00	0.31	55.72	1.35	0.00
11310	3.45	20.89	112.85	0.06	356.77	271.88	130.23	165.23	0.46	0.00	1.11	0.43	0.20	0.34	54.78	1.50	0.00
11400	0.00	21.50	93.46	0.06	201.07	156.52	81.07	107.21	0.50	2.37	1.17	0.33	0.26	0.40	51.39	1.72	0.00
11490	0.00	25.90	89.69	0.05	335.57	225.65	114.77	170.59	0.41	0.00	0.96	0.32	0.25	0.40	50.19	1.73	0.00
11580	2.91	24.66	89.95	0.06	349.70	248.07	118.11	156.25	0.46	2.67	0.99	0.54	0.33	0.49	48.24	2.32	0.00
11670	0.00	20.86	111.28	0.06	158.30	67.76	98.33	103.49	0.40	2.38	1.34	0.37	0.27	0.41	57.55	1.70	0.00
11760	3.20	27.95	119.63	0.07	201.66	83.90	100.52	116.91	0.50	1.92	1.42	0.16	0.25	0.44	55.91	1.75	0.00
11850	0.00	19.52	112.28	0.06	131.49	0.00	0.00	84.70	0.40	3.47	1.19	0.25	0.25	0.37	56.60	1.64	0.00
11940	9.55	26.13	118.93	0.15	275.68	123.44	104.15	142.42	0.50	2.55	1.38	0.47	0.48	1.37	53.05	1.52	0.00
12030	0.00	20.50	85.91	0.06	0.00	0.00	0.00	0.00	0.39	0.00	1.13	0.42	0.23	0.39	57.91	1.50	0.00
12120	0.00	21.54	102.29	0.06	196.10	85.79	85.47	119.62	0.57	0.00	0.55	0.24	0.00	0.30	56.32	1.25	0.00
12210	2.55	27.25	118.03	0.06	421.54	225.90	181.11	184.52	0.55	2.74	0.96	0.28	0.00	0.27	57.24	1.39	0.00

Continued.

Depth (ft)	Zr (ppm)	Zn (ppm)	Ni (ppm)	Fe (%)	Nd (ppm)	Pr (ppm)	Ce (ppm)	La (ppm)	Ba (%)	Nb (ppm)	Ca (%)	K (%)	Al (%)	Si (%)	Cl (%)	S (%)	Mg (%)
12300	0.00	25.48	92.69	0.06	159.45	0.00	68.03	78.40	0.48	0.00	0.96	0.23	0.00	0.31	56.27	1.28	0.00
12390	0.00	26.23	105.29	0.06	148.79	0.00	0.00	77.48	0.49	2.05	0.66	0.67	0.20	0.35	56.29	0.87	0.00
12480	3.44	29.10	118.05	0.08	253.20	118.03	105.22	139.82	0.52	0.00	0.94	0.16	0.18	0.44	56.20	1.16	0.00
12570	2.82	25.24	108.34	0.08	0.00	0.00	0.00	0.00	0.59	0.00	0.35	0.11	0.00	0.37	57.98	0.80	0.00
12660	2.87	29.20	121.05	0.07	209.93	83.80	92.65	88.26	0.55	2.11	0.97	0.00	0.00	0.33	56.02	1.21	0.00
12750	6.50	26.09	139.04	0.08	282.10	113.19	159.93	158.59	0.69	0.00	1.30	0.00	0.00	0.35	55.76	1.65	0.00
12840	2.78	18.35	117.27	0.05	312.30	182.12	122.00	186.18	0.58	0.00	0.32	0.04	0.00	0.25	57.07	0.69	0.00
12930	0.00	19.55	103.10	0.05	0.00	0.00	0.00	0.00	0.39	0.00	0.69	0.00	0.00	0.20	58.27	0.69	0.00
13020	2.23	17.79	90.14	0.06	0.00	0.00	0.00	0.00	0.48	0.00	0.39	0.04	0.15	0.32	55.82	1.33	0.00
13100	0.00	21.18	102.88	0.05	0.00	0.00	0.00	0.00	0.49	1.65	0.41	0.04	0.00	0.27	57.73	1.42	0.00
13110	0.00	19.95	86.41	0.06	0.00	0.00	0.00	57.90	0.42	1.78	0.77	0.00	0.26	0.27	56.40	0.90	0.00
13145	14.01	21.76	105.71	0.48	154.67	86.42	71.93	0.00	0.43	0.00	0.85	0.25	0.72	2.66	50.32	1.03	0.00
13160	62.48	24.01	152.84	6.53	214.12	120.77	91.21	135.98	0.61	3.22	1.08	0.38	1.36	5.94	32.79	1.40	1.38
13200	31.51	25.62	100.02	2.34	0.00	0.00	0.00	0.00	0.41	3.51	2.23	0.08	1.10	4.53	41.32	1.77	0.00
13290	22.34	22.10	126.02	1.09	383.33	228.19	144.38	180.95	0.56	4.57	1.93	0.15	0.90	3.38	45.99	1.83	0.00
13350	34.51	20.02	113.15	2.60	200.93	81.73	0.00	79.31	0.56	3.03	2.39	0.18	1.61	5.41	38.85	2.72	0.00
13380	52.92	19.15	145.48	4.25	184.60	72.01	101.60	127.99	0.68	4.64	2.43	0.22	1.81	6.22	33.94	2.72	1.32
13410	40.94	27.73	146.14	4.67	158.74	0.00	59.99	79.87	0.75	4.42	2.34	0.21	1.44	6.10	34.88	2.58	0.00
13440	35.36	18.05	137.00	4.72	169.36	71.60	71.82	89.44	0.58	3.03	1.88	0.28	1.19	5.25	35.65	2.60	0.00
13470	23.86	21.25	116.72	3.47	156.56	65.33	56.41	89.60	0.40	3.49	1.08	0.34	1.10	4.36	40.32	2.28	0.00
13500	20.32	18.74	115.17	3.13	241.80	160.75	91.44	139.25	0.42	3.32	0.75	0.27	0.68	2.92	45.07	1.46	0.00
13530	27.68	21.48	123.02	4.05	265.29	176.27	116.30	109.73	0.41	0.00	1.33	0.39	1.17	4.96	37.23	2.30	1.36

Continued.



Depth (ft)	Zr (ppm)	Zn (ppm)	Ni (ppm)	Fe (%)	Nd (ppm)	Pr (ppm)	Ce (ppm)	La (ppm)	Ba (%)	Nb (ppm)	Ca (%)	K (%)	Al (%)	Si (%)	Cl (%)	S (%)	Mg (%)
13560	26.49	19.40	116.09	1.73	210.58	0.00	129.93	78.80	0.50	3.42	1.82	0.12	0.97	3.78	44.97	1.89	0.00
13590	21.04	22.00	98.78	2.67	86.11	0.00	53.55	0.00	0.41	3.78	0.77	0.45	0.81	3.45	44.43	2.09	0.00
13620	22.95	27.57	140.20	2.39	215.81	114.90	110.84	130.23	0.66	3.19	0.54	0.26	0.95	3.71	44.23	1.81	0.00
13635	44.03	27.29	115.57	5.73	217.84	106.39	77.49	148.61	0.47	3.97	0.99	0.48	1.36	6.60	32.86	1.58	0.00
13650	36.19	21.02	101.46	3.80	127.85	0.00	58.39	87.73	0.39	4.26	0.71	0.43	1.02	4.70	40.27	1.81	0.00
13680	87.90	15.34	91.32	7.05	0.00	0.00	0.00	0.00	0.29	4.96	0.92	0.66	1.76	8.85	27.53	1.40	0.00
13710	100.17	21.65	125.72	8.49	237.67	95.02	136.33	143.03	0.44	3.94	1.02	0.90	2.47	11.20	23.46	1.26	1.21
13740	64.15	23.45	124.17	6.20	193.87	74.58	63.34	97.17	0.38	4.39	1.27	0.83	1.73	8.16	32.21	1.62	0.00
13770	131.08	23.13	119.22	9.15	0.00	0.00	0.00	0.00	0.55	6.22	1.72	1.17	2.44	11.80	21.30	2.15	0.00
13800	81.60	16.21	153.59	11.59	518.59	271.75	185.96	195.89	0.56	6.24	1.53	1.06	2.06	9.85	22.82	2.24	0.00
13830	75.11	37.17	267.83	10.25	0.00	0.00	0.00	0.00	2.07	5.62	1.45	0.98	2.14	10.35	20.21	2.54	0.00
13860	66.75	34.50	199.96	8.72	340.72	0.00	118.10	163.23	1.11	4.79	1.00	1.04	1.90	9.35	25.63	1.83	1.43
13890	24.03	27.39	139.19	2.91	309.59	174.68	133.71	187.20	0.61	3.67	0.74	0.32	1.00	3.86	46.60	0.90	0.00
13920	75.27	38.23	182.11	8.02	288.34	0.00	114.59	154.28	0.88	4.47	1.74	1.21	1.82	8.57	26.60	2.26	0.00
13950	46.65	25.43	140.59	4.71	107.75	0.00	60.85	70.11	0.68	3.71	1.15	0.61	1.20	5.90	39.24	1.56	0.00
13978	72.39	25.88	134.17	7.82	274.34	126.89	113.00	144.78	0.53	6.07	1.52	1.16	2.10	9.72	25.78	1.95	0.00
13980	21.14	23.38	140.99	3.40	295.01	80.24	127.55	144.12	0.83	2.37	0.34	0.31	0.95	4.09	44.81	0.88	0.00
14010	10.03	18.48	134.21	2.16	247.59	79.32	112.60	121.72	0.51	0.00	0.81	0.32	0.63	2.66	47.88	1.14	0.00
14040	5.07	17.49	88.80	0.62	156.49	0.00	72.72	99.64	0.38	0.00	0.71	0.37	0.46	1.09	54.47	0.84	0.00
14070	7.14	18.60	99.57	1.12	0.00	0.00	0.00	0.00	0.44	0.00	0.87	0.17	0.42	1.67	53.44	1.08	0.00
14100	0.00	22.31	116.56	0.09	203.88	0.00	82.33	114.57	0.52	0.00	0.65	0.00	0.00	0.32	58.02	0.73	0.00
14130	0.00	21.80	130.64	0.09	163.54	88.58	79.20	113.95	0.54	2.00	0.72	0.00	0.00	0.27	57.02	0.77	0.00

Continued.

Depth (ft)	Zr (ppm)	Zn (ppm)	Ni (ppm)	Fe (%)	Nd (ppm)	Pr (ppm)	Ce (ppm)	La (ppm)	Ba (%)	Nb (ppm)	Ca (%)	K (%)	Al (%)	Si (%)	Cl (%)	S (%)	Mg (%)
14160	2.14	18.57	108.02	0.07	95.30	0.00	58.00	81.22	0.46	0.00	0.37	0.05	0.00	0.28	57.00	0.73	0.00
14190	3.13	22.99	125.83	0.10	146.31	74.77	59.47	80.81	0.58	0.00	0.65	0.01	0.00	0.33	57.14	0.71	0.00
14220	3.15	14.31	104.09	0.07	153.42	0.00	83.54	109.48	0.51	2.14	0.63	0.00	0.00	0.28	57.00	0.70	0.00
14250	5.34	21.13	120.31	0.07	166.25	66.87	76.06	89.02	0.49	3.25	0.69	0.00	0.17	0.31	56.43	0.86	0.00
14280	3.13	16.31	93.06	0.07	0.00	0.00	0.00	0.00	0.46	2.08	0.81	0.00	0.00	0.24	59.51	0.84	0.00
14370	0.00	23.50	105.62	0.09	0.00	0.00	0.00	0.00	0.44	0.00	0.88	0.81	0.18	0.38	59.23	0.80	0.00
14460	2.28	19.18	95.33	0.09	0.00	0.00	0.00	0.00	0.45	2.10	0.90	0.05	0.00	0.37	57.08	0.83	0.00
14550	0.00	21.22	117.04	0.08	223.67	116.89	92.03	95.90	0.55	2.20	1.28	0.01	0.00	0.26	55.66	1.41	0.00
14640	0.00	23.67	104.81	0.08	142.40	0.00	65.34	87.21	0.46	0.00	1.29	0.00	0.00	0.29	56.47	1.48	0.00
14730	2.76	21.09	107.63	0.07	58.61	0.00	43.07	47.25	0.54	0.00	1.22	0.03	0.18	0.30	56.77	1.49	0.00
14820	0.00	27.97	115.53	0.07	289.73	151.48	126.38	169.12	0.54	0.00	1.83	0.00	0.00	0.26	55.24	2.15	0.00
14910	0.00	19.47	109.81	0.07	128.42	0.00	55.16	92.72	0.57	0.00	1.73	0.04	0.00	0.25	56.00	1.95	0.00
15000	0.00	24.53	136.25	0.07	335.75	190.14	139.28	163.15	0.59	0.00	1.87	0.00	0.00	0.29	54.93	2.18	0.00
15030	0.00	19.05	121.75	0.07	281.96	176.33	116.77	151.40	0.57	0.00	2.28	0.00	0.00	0.32	52.58	2.95	0.00
15120	2.88	20.79	121.16	0.09	123.61	0.00	66.94	84.06	0.55	1.77	1.70	0.00	0.16	0.39	54.65	2.06	0.00
15210	0.00	29.60	123.08	0.07	290.77	181.18	127.49	133.19	0.59	2.22	1.10	0.00	0.00	0.26	56.21	1.34	0.00
15300	0.00	26.33	122.82	0.08	189.27	128.75	80.37	111.78	0.54	0.00	1.62	0.00	0.00	0.30	55.03	1.99	0.00
15390	5.42	23.06	125.19	0.07	300.50	170.93	118.78	151.60	0.64	0.00	1.65	0.00	0.00	0.29	54.50	2.06	0.00
15480	2.83	25.26	129.25	0.08	242.51	148.14	128.09	119.91	0.68	1.71	0.80	0.00	0.00	0.30	55.77	0.98	0.00
15570	2.33	24.95	125.28	0.07	183.60	144.56	91.84	112.63	0.56	1.83	0.68	0.00	0.17	0.26	57.67	0.71	0.00
15660	0.00	19.47	109.36	0.08	0.00	0.00	0.00	0.00	0.50	2.31	1.05	0.00	0.00	0.34	55.38	1.24	0.00
15750	0.00	26.41	117.45	0.08	128.70	102.54	79.33	105.00	0.59	0.00	0.97	0.00	0.00	0.30	55.97	1.12	0.00

Continued.

Depth (ft)	Zr (ppm)	Zn (ppm)	Ni (ppm)	Fe (%)	Nd (ppm)	Pr (ppm)	Ce (ppm)	La (ppm)	Ba (%)	Nb (ppm)	Ca (%)	K (%)	Al (%)	Si (%)	Cl (%)	S (%)	Mg (%)
16950	2.66	18.15	112.17	0.06	284.10	167.63	86.21	161.00	0.42	1.90	2.29	0.00	0.00	0.20	53.63	2.33	0.00
17040	0.00	20.82	120.79	0.06	280.86	152.78	106.91	140.12	0.51	0.00	1.51	0.04	0.00	0.22	55.17	1.50	0.00
17220	3.40	23.51	108.63	0.09	123.01	115.94	0.00	0.00	0.44	0.00	2.21	0.01	0.00	0.37	55.85	1.74	0.00
17310	4.23	19.77	96.90	0.06	154.43	86.59	0.00	78.10	0.44	0.00	1.98	0.00	0.00	0.26	56.41	2.21	0.00
17400	0.00	19.82	118.68	0.07	215.35	185.15	94.80	134.83	0.45	0.00	2.20	0.00	0.16	0.28	55.91	2.54	0.00
17430	2.64	21.25	126.70	0.08	276.35	220.45	95.89	143.87	0.61	0.00	2.22	0.00	0.25	0.34	54.66	2.55	0.00
17520	0.00	19.94	114.95	0.06	243.61	244.17	106.05	124.93	0.58	0.00	1.74	0.04	0.28	0.30	56.25	2.01	0.00
17610	3.23	18.90	127.38	0.07	515.89	400.95	183.30	218.39	0.54	2.17	1.51	0.00	0.00	0.31	55.74	1.67	0.00
17700	4.21	18.79	124.51	0.07	267.33	249.65	143.93	143.31	0.50	0.00	1.93	0.00	0.00	0.28	55.56	2.12	0.00
17790	2.97	21.83	105.40	0.06	250.56	123.27	108.76	138.59	0.42	0.00	2.06	0.00	0.00	0.28	54.73	2.07	0.00
17880	0.00	20.62	123.71	0.07	320.85	171.90	132.39	174.44	0.51	2.04	3.19	0.00	0.19	0.27	53.36	3.47	0.00
17970	2.20	22.81	109.21	0.06	242.93	99.43	91.39	130.30	0.47	1.98	3.53	0.04	0.16	0.29	51.37	3.69	0.00
18060	0.00	18.99	112.67	0.06	130.36	0.00	0.00	75.00	0.42	0.00	3.10	0.00	0.00	0.30	52.55	3.26	0.00
18150	3.49	20.26	127.52	0.07	332.26	168.63	116.27	155.54	0.62	2.46	2.84	0.04	0.21	0.25	53.05	2.98	0.00
18240	0.00	23.45	116.76	0.07	314.53	207.72	117.96	147.67	0.49	2.10	3.32	0.00	0.00	0.27	52.34	3.56	0.00
18330	0.00	20.85	104.72	0.06	308.43	133.31	131.07	131.65	0.58	0.00	3.52	0.04	0.00	0.30	51.58	4.00	0.00
18420	0.00	22.09	100.43	0.06	185.45	0.00	86.52	95.64	0.47	0.00	3.29	0.00	0.00	0.28	52.53	3.51	0.00
18510	4.23	20.74	116.22	0.07	305.36	131.62	133.86	151.33	0.51	0.00	4.02	0.00	0.00	0.25	50.95	4.40	0.00
18600	6.62	19.10	106.23	0.07	187.46	93.11	69.44	103.09	0.53	0.00	2.90	0.04	0.20	0.24	53.10	3.15	0.00
18690	5.91	22.75	126.32	0.07	299.24	83.37	89.19	120.94	0.58	2.25	3.35	0.00	0.16	0.25	51.54	3.66	0.00
18780	3.70	21.80	113.37	0.07	164.92	96.52	83.03	120.82	0.50	0.00	3.85	0.00	0.17	0.27	51.35	4.12	0.00
18870	0.00	25.74	109.65	0.07	216.49	104.16	74.37	136.30	0.51	0.00	3.73	0.00	0.00	0.27	52.08	4.01	0.00

Continued.

Depth (ft)	Zr (ppm)	Zn (ppm)	Ni (ppm)	Fe (%)	Nd (ppm)	Pr (ppm)	Ce (ppm)	La (ppm)	Ba (%)	Nb (ppm)	Ca (%)	K (%)	Al (%)	Si (%)	Cl (%)	S (%)	Mg (%)
18960	2.22	23.11	118.83	0.07	315.99	159.92	131.65	171.37	0.60	0.00	3.34	0.03	0.00	0.27	50.96	3.63	0.00
19050	3.07	20.60	120.13	0.07	0.00	67.52	68.53	91.55	0.49	2.61	3.45	0.00	0.00	0.29	51.77	3.75	0.00
19140	0.00	24.47	131.03	0.07	264.03	125.77	126.97	129.83	0.66	0.00	1.52	0.05	0.00	0.30	53.74	1.68	0.00
19230	0.00	20.41	113.80	0.07	277.84	161.70	127.76	130.34	0.67	2.43	2.43	0.04	0.18	0.26	53.18	2.51	0.00
19320	0.00	23.51	117.29	0.07	163.15	84.34	66.89	71.04	0.54	0.00	1.73	0.00	0.00	0.25	55.46	1.78	0.00
19410	5.38	18.98	116.71	0.07	126.79	0.00	0.00	92.50	0.64	0.00	1.34	0.04	0.00	0.29	55.61	1.36	0.00
19500	0.00	21.18	108.37	0.07	91.36	0.00	53.31	86.84	0.54	2.46	1.03	0.00	0.00	0.26	56.88	1.02	0.00
19590	0.00	29.89	112.48	0.08	239.05	114.82	108.15	98.04	0.67	0.00	1.96	0.05	0.00	0.31	55.15	1.65	0.00
19680	0.00	12.99	0.00	0.00	107.12	0.00	0.00	86.16	0.40	2.07	1.28	0.00	0.00	0.23	50.08	1.26	0.00
19770	0.00	20.29	100.18	0.07	0.00	0.00	0.00	51.85	0.41	0.00	1.47	0.00	0.00	0.27	55.98	1.31	0.00
19868	68.46	52.28	118.39	1.68	206.86	88.97	109.71	117.47	0.42	5.87	6.56	0.91	2.41	10.65	26.39	1.45	0.00
19877	148.56	77.43	65.40	3.09	0.00	0.00	54.34	48.30	0.25	10.14	6.46	1.46	3.66	19.95	4.06	0.85	0.46
19860	196.32	72.41	63.01	3.02	0.00	0.00	0.00	0.00	0.25	10.92	5.02	1.50	3.67	20.72	5.41	0.90	0.69
19950	184.26	79.74	75.09	3.58	0.00	0.00	0.00	0.00	0.36	12.30	1.39	1.60	3.95	21.40	6.40	0.57	0.00
20010	207.86	78.69	73.35	3.56	0.00	0.00	0.00	0.00	0.33	12.44	1.94	1.59	3.79	23.02	1.86	0.50	0.26
20040	218.59	74.50	66.05	3.55	0.00	0.00	42.48	49.03	0.25	0.00	1.68	1.58	4.25	25.03	1.49	0.54	1.14
20060	232.23	76.60	60.39	3.48	0.00	0.00	0.00	0.00	0.25	12.17	1.96	1.56	3.58	24.10	1.52	0.40	0.00
20130	232.63	60.58	56.54	3.33	0.00	0.00	0.00	0.00	0.24	10.95	1.59	1.60	4.08	25.75	1.35	0.33	0.70
20220	208.12	83.61	61.34	3.88	0.00	0.00	0.00	0.00	0.19	12.70	2.08	1.87	4.78	25.10	1.37	0.59	0.77
20310	234.41	79.07	64.71	3.74	0.00	0.00	0.00	0.00	0.25	13.13	1.87	1.69	4.29	25.51	1.23	0.63	0.60
20400	219.77	85.60	85.58	3.44	0.00	0.00	0.00	0.00	0.41	11.80	1.74	1.77	4.29	25.26	1.19	0.75	0.85
20490	211.94	90.87	91.31	3.83	0.00	0.00	0.00	0.00	0.41	13.23	1.15	1.90	4.87	25.32	1.07	0.66	0.53

Continued.

Depth (ft)	Zr (ppm)	Zn (ppm)	Ni (ppm)	Fe (%)	Nd (ppm)	Pr (ppm)	Ce (ppm)	La (ppm)	Ba (%)	Nb (ppm)	Ca (%)	K (%)	Al (%)	Si (%)	Cl (%)	S (%)	Mg (%)
20580	152.71	108.86	113.15	4.31	0.00	0.00	63.67	64.84	0.48	11.42	1.36	1.95	4.72	23.47	0.99	0.94	0.69
20670	158.09	101.93	105.49	4.13	0.00	0.00	0.00	0.00	0.44	12.29	1.58	1.94	4.67	23.46	0.83	0.73	0.71
20720	260.62	90.22	74.37	3.48	0.00	0.00	0.00	0.00	0.39	18.63	0.92	1.55	4.42	26.63	1.06	1.06	0.95
20760	178.03	100.76	96.61	4.22	0.00	0.00	0.00	0.00	0.42	13.95	1.42	1.86	4.70	25.48	0.71	1.09	0.73
20765	228.36	91.63	78.81	3.78	0.00	0.00	0.00	0.00	0.39	13.96	1.10	1.90	4.70	25.41	0.75	0.93	0.85
20850	244.76	92.02	92.82	3.66	0.00	0.00	47.66	60.62	0.43	15.35	1.13	1.78	4.77	25.71	0.56	0.79	0.80
20880	249.89	78.26	88.83	3.35	0.00	0.00	0.00	0.00	0.44	12.99	1.08	1.68	4.27	25.49	0.56	0.77	0.60
20970	281.24	70.20	96.75	2.95	0.00	0.00	0.00	0.00	0.54	13.30	1.00	1.53	3.52	30.05	0.67	0.75	0.26
21060	238.85	100.21	117.34	4.01	0.00	0.00	0.00	0.00	0.50	11.86	1.50	1.87	4.61	24.68	0.41	0.82	0.74
21150	254.16	56.28	103.47	1.96	0.00	0.00	0.00	0.00	0.73	10.22	0.85	1.31	2.77	34.74	0.84	0.90	0.47
21215	232.19	45.01	108.38	1.53	0.00	0.00	0.00	0.00	0.69	4.91	1.00	1.06	1.96	36.78	0.72	0.60	0.33
21240	245.44	94.86	84.01	4.28	0.00	0.00	0.00	0.00	0.43	12.60	0.96	1.79	4.90	24.95	0.33	1.10	0.63
21330	235.96	93.76	83.88	3.75	0.00	0.00	47.65	62.09	0.47	15.21	1.21	1.65	4.59	25.71	0.40	0.73	0.65
21420	229.37	97.92	86.74	3.95	0.00	0.00	0.00	0.00	0.37	13.32	1.14	1.68	4.57	23.73	0.48	1.92	0.56

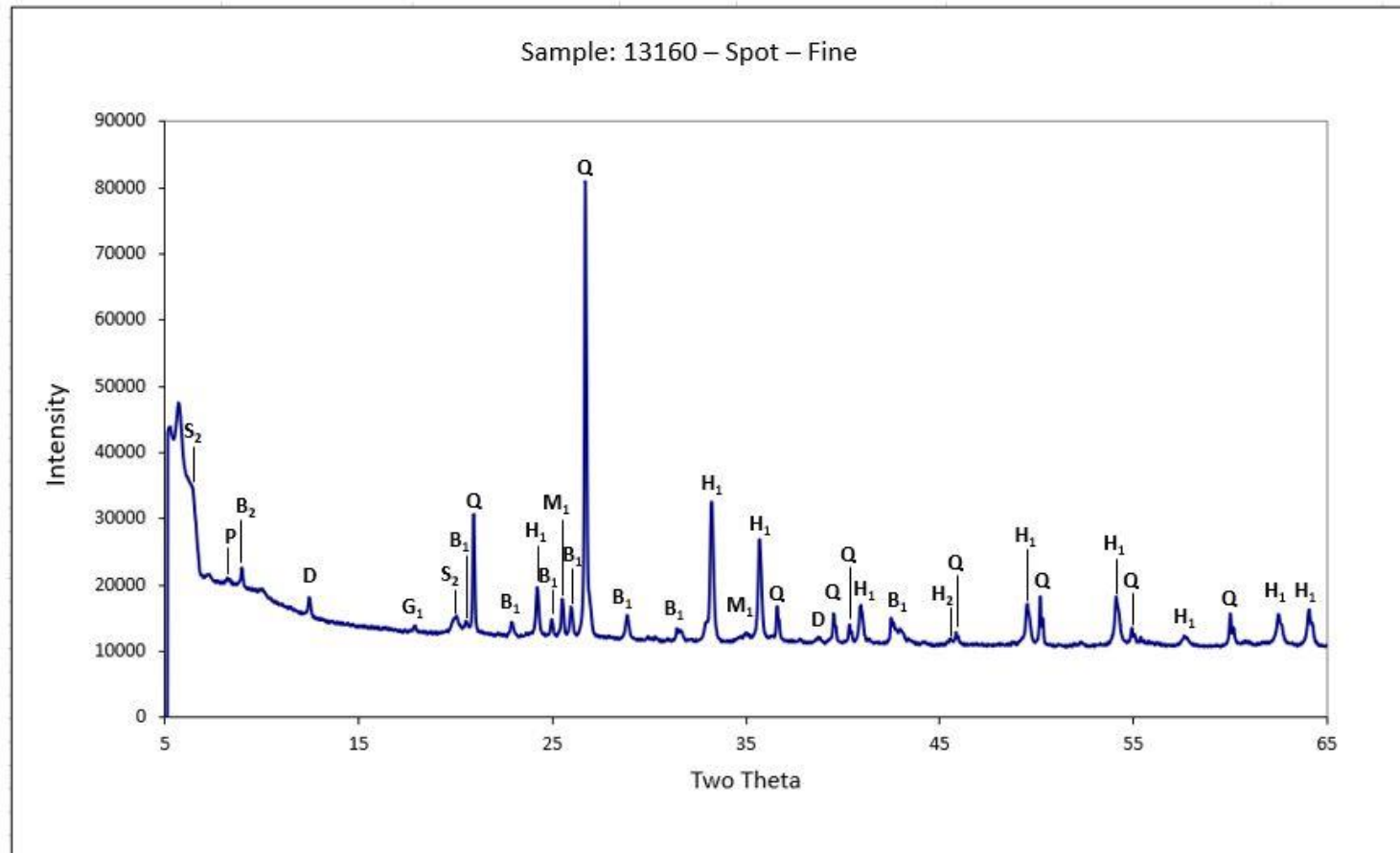
14.4 Appendix D – Detailed XRD Results

Sample Name:	13160 Spot Fine	13200 - 13230	13350 - 13380 Fine	13410 - 13440 Fine	13500 - 13530	13635 Spot Fine	13710 - 13740	13830 - 13860 Fine	13920 - 13950 Fine	13978 Spot Fine
Full Pattern Degree of Fit:	0.0372	0.0876	0.0775	0.0633	0.0377	0.0451	0.0393	0.0455	0.0451	0.0490
<u>Mineral</u>	Wt %	Wt %	Wt %	Wt %	Wt %	Wt %	Wt %	Wt %	Wt %	Wt %
<b>NON-CLAYS</b>										
Quartz	25.5	32.0	28.7	23.0	26.0	26.7	25.7	26.2	28.6	24.6
Hematite	20.7	12.2	10.4	15.6	19.4	17.1	16.9	17.1	20.3	19.6
Kspar (Intermediate Microcline)	6.6	6.5	5.6	6.0	6.7	6.0	6.7	6.3	7.3	7.4
Barite	4.1	4.8	4.1	5.1	5.4	3.3	2.4	6.9	7.4	2.9
Anhydrite	2.7	5.3	6.5	2.9	1.3	0.6	2.5	1.9	2.2	4.0
Gypsum	1.8	2.7	1.7	1.8	2.6	2.1	2.1	3.4	1.4	1.4
Goethite	0.9	1.1	1.0	1.4	0.9	0.5	0.5	0.4	0.7	1.0
Calcite	0.4	0.9	0.7	1.0	0.6	0.6	0.5	1.5	0.6	0.6
Halite	0.3	0.3	0.3	0.4	0.4	0.3	0.2	0.4	0.2	0.2
Sylvite	0.0	0.1	0.0	0.0	0.1	0.0	0.1	0.0	0.0	0.1
Kspar (Ordered Microcline)	0.0	0.0	0.0	0.0	0.0	0.0	0.0	0.0	0.0	0.0
Total Non-Clays	63.0	65.8	59.1	57.2	63.4	57.1	57.7	64.2	68.8	61.8
<b>CLAYS</b>										
Smectite (Ca-Kinney Montmorillonite)	5.6	3.8	13.2	16.0	11.3	17.4	12.7	11.9	12.2	14.9
Halloysite	8.9	10.9	10.1	13.8	11.4	11.2	10.3	6.2	5.3	6.2
Smectite (Na-Kinney Montmorillonite)	10.8	2.3	7.9	6.0	1.0	2.7	6.4	4.8	3.8	6.3
Glauconite	2.5	7.5	5.3	4.0	5.4	4.4	4.3	4.4	4.6	3.5
Biotite (1M)	2.5	1.2	2.2	2.4	1.8	2.0	1.9	1.9	1.1	0.6
Dickite	1.4	1.6	2.2	0.7	0.0	0.5	1.2	2.5	0.6	3.8
Chlorite (CMM)	0.0	1.7	0.0	0.0	2.4	3.4	1.4	1.2	1.3	0.0

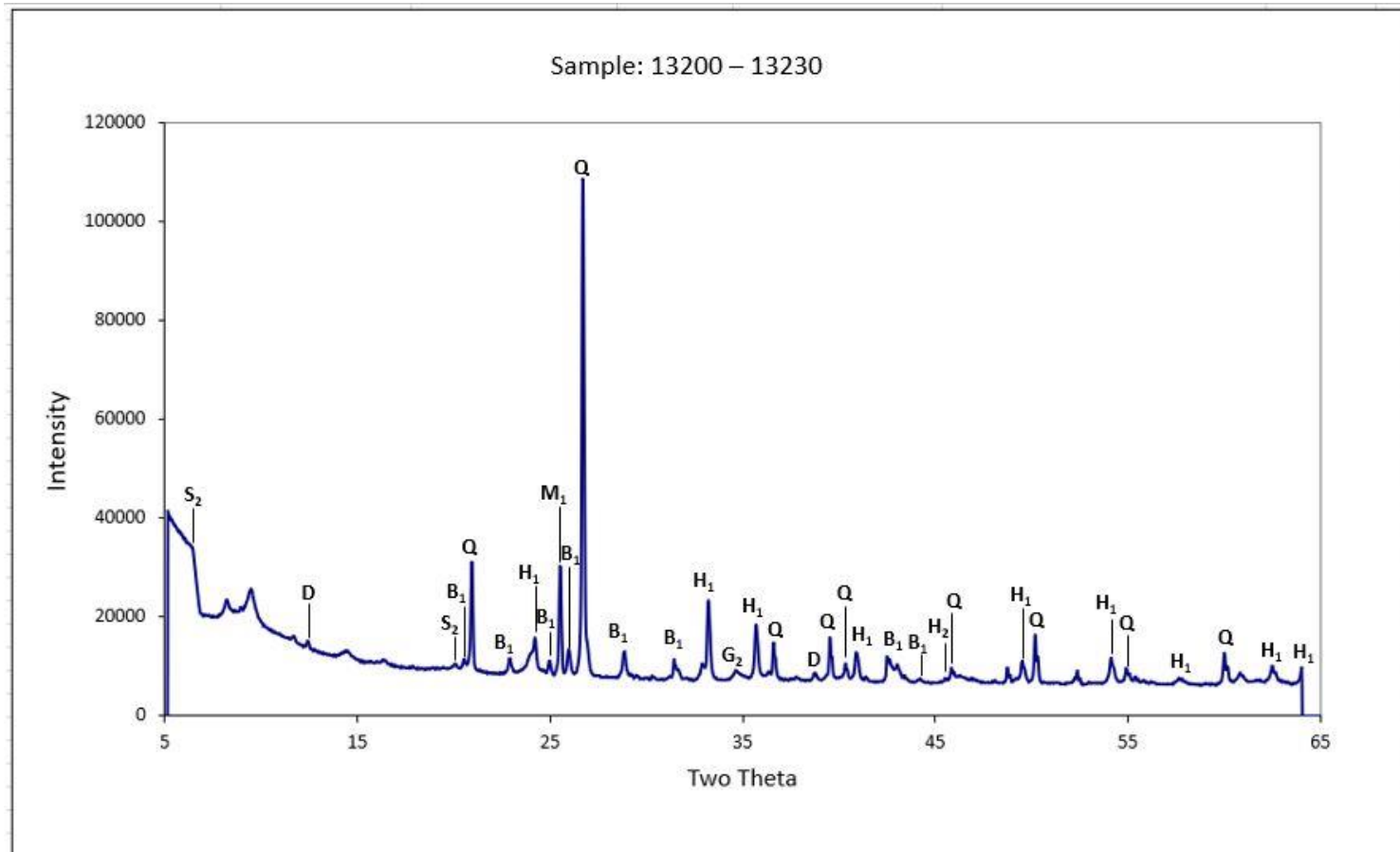
Continued.

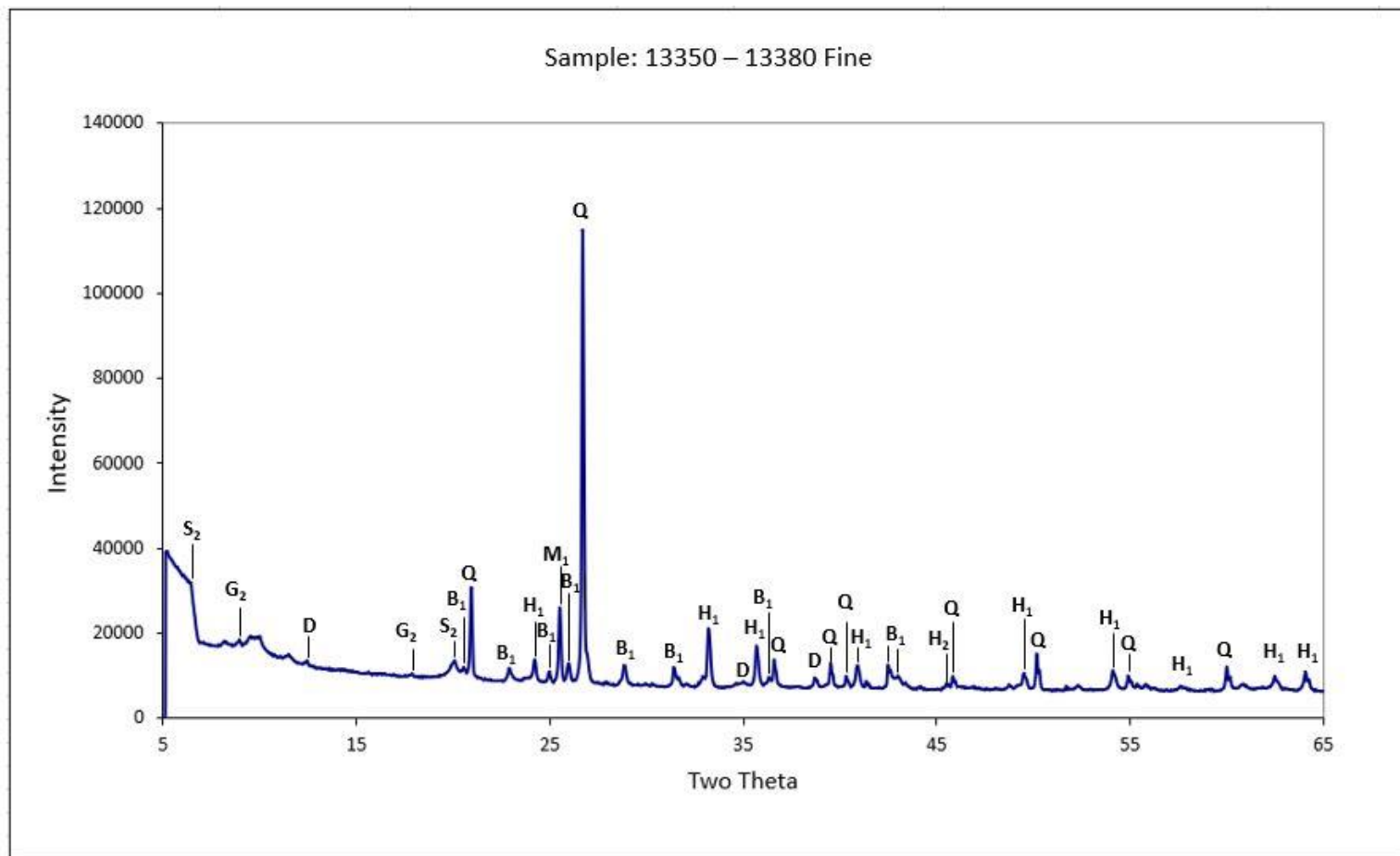
Sample Name:	13160 Spot Fine	13200 - 13230	13350 - 13380 Fine	13410 - 13440 Fine	13500 - 13530	13635 Spot Fine	13710 - 13740	13830 - 13860 Fine	13920 - 13950 Fine	13978 Spot Fine
Palygorskite	1.6	0.0	0.0	0.0	3.0	0.0	1.6	2.5	1.1	0.8
Smectite (Saponite)	0.0	5.2	0.0	0.0	0.0	0.0	0.0	0.0	0.0	0.0
Muscovite (2M1)	0.0	0.0	0.0	0.0	0.0	0.0	1.5	0.0	0.6	1.8
Chlorite (Fe-rich; Tusc)	3.9	0.0	0.0	0.0	0.0	0.0	0.0	0.0	0.0	0.0
Illite (EP-10-66)	0.0	0.0	0.0	0.0	0.0	0.0	0.8	0.3	0.1	0.0
Kaolinite (Dry Branch)	0.0	0.0	0.0	0.0	0.3	0.4	0.0	0.0	0.0	0.2
Kaolinite (Ordered)	0.0	0.0	0.0	0.0	0.0	0.9	0.0	0.0	0.0	0.0
Illite (2M1; SG4)	0.0	0.0	0.0	0.0	0.0	0.0	0.2	0.0	0.4	0.0
Illite (1M Metabent; 0% exp)	0.0	0.0	0.0	0.0	0.0	0.0	0.0	0.0	0.0	0.0
Illite (1Md)	0.0	0.0	0.0	0.0	0.0	0.0	0.0	0.0	0.0	0.0
Illite (1M; R>3; 95%I)	0.0	0.0	0.0	0.0	0.0	0.0	0.0	0.0	0.0	0.0
Illite (R>1, 70-80%I)	0.0	0.0	0.0	0.0	0.0	0.0	0.0	0.0	0.0	0.0
Illite (1M; RM30)	0.0	0.0	0.0	0.0	0.0	0.0	0.0	0.0	0.0	0.0
Phlogopite (2M1 )	0.0	0.0	0.0	0.0	0.0	0.0	0.0	0.0	0.0	0.0
Total Clays	37.0	34.2	40.9	42.8	36.6	42.9	42.3	35.8	31.2	38.2
<b>TOTAL</b>	100.0	100.0	100.0	100.0	100.0	100.0	100.0	100.0	100.0	100.0

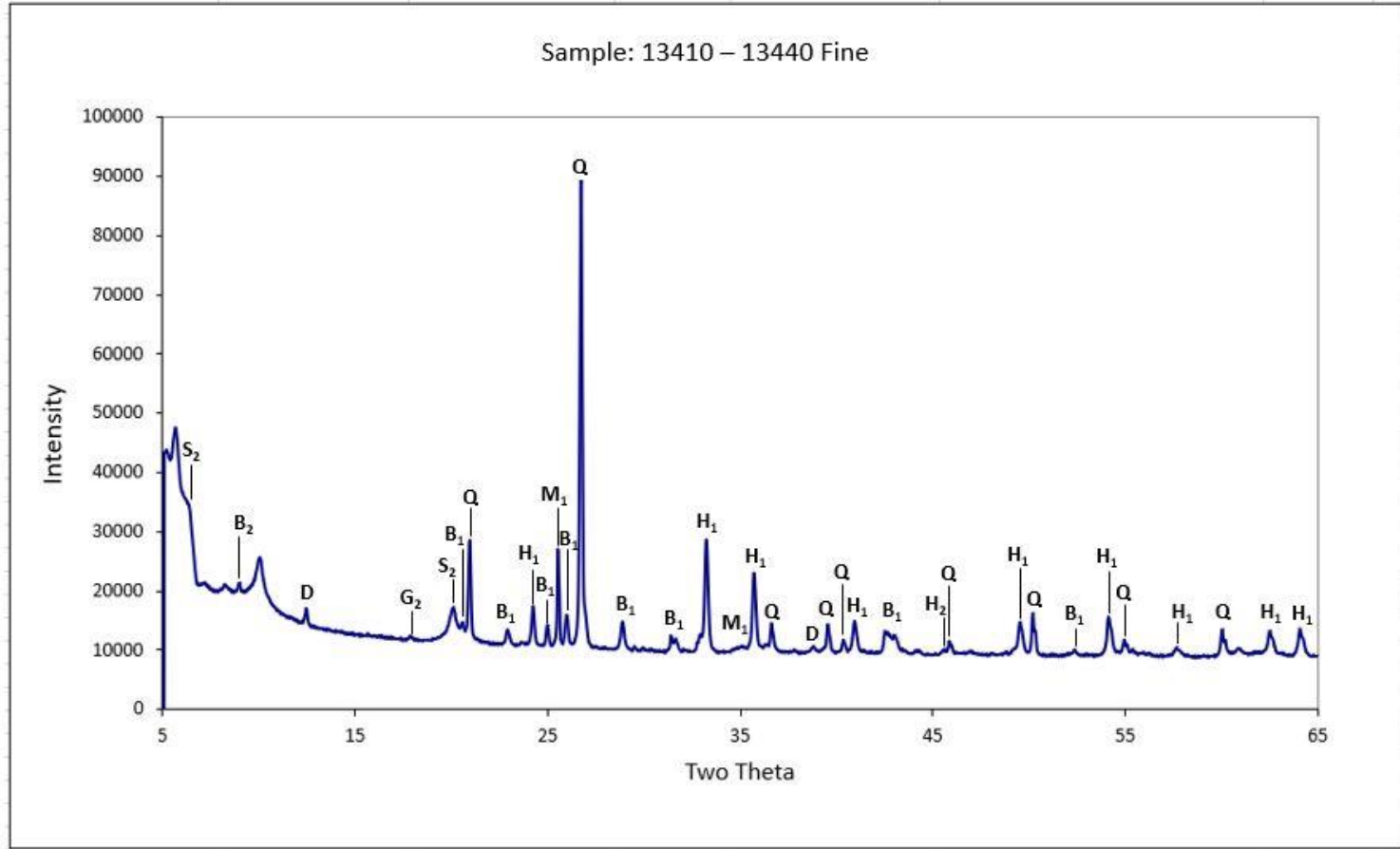
14.5 Appendix E – XRD Graphs

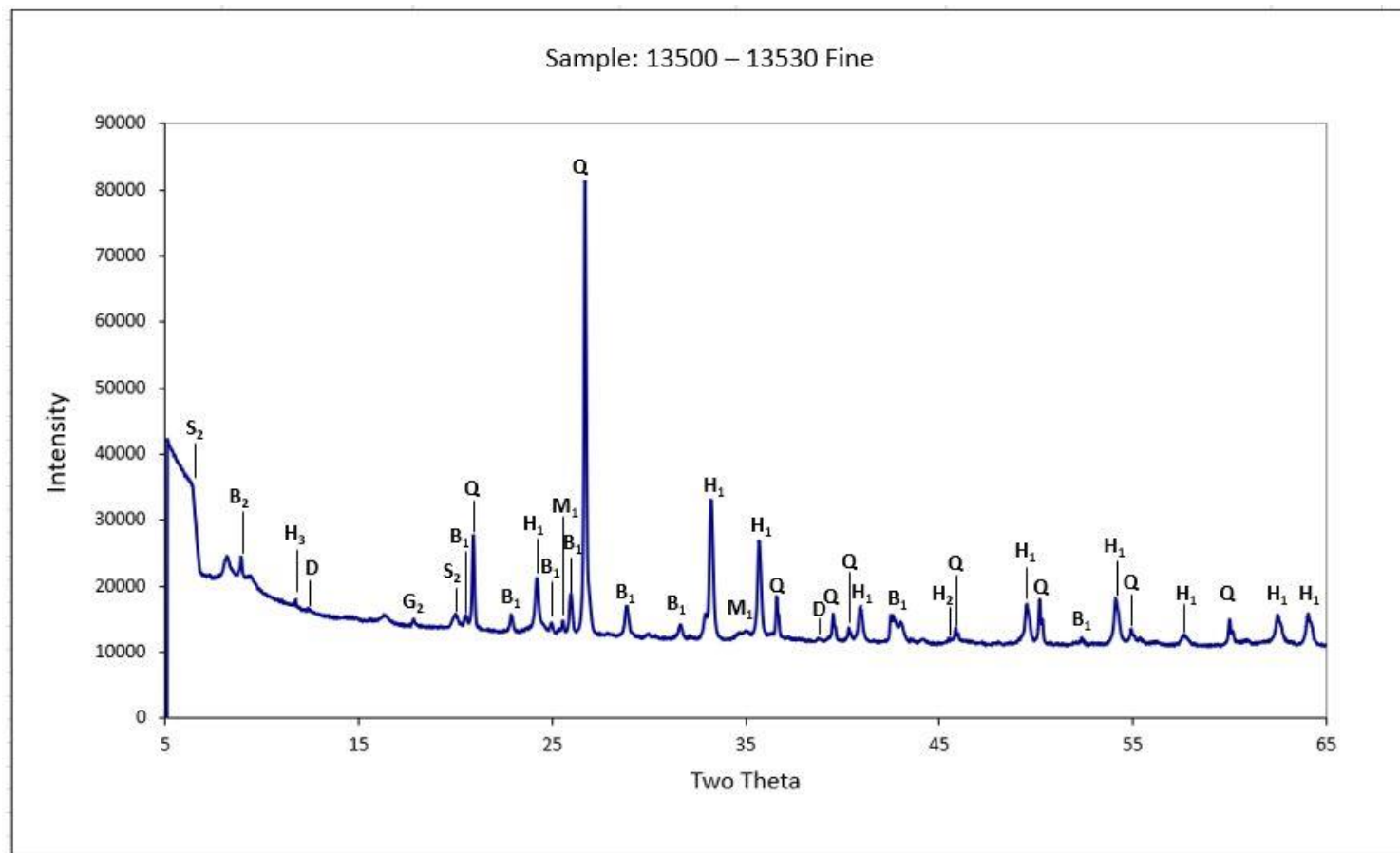


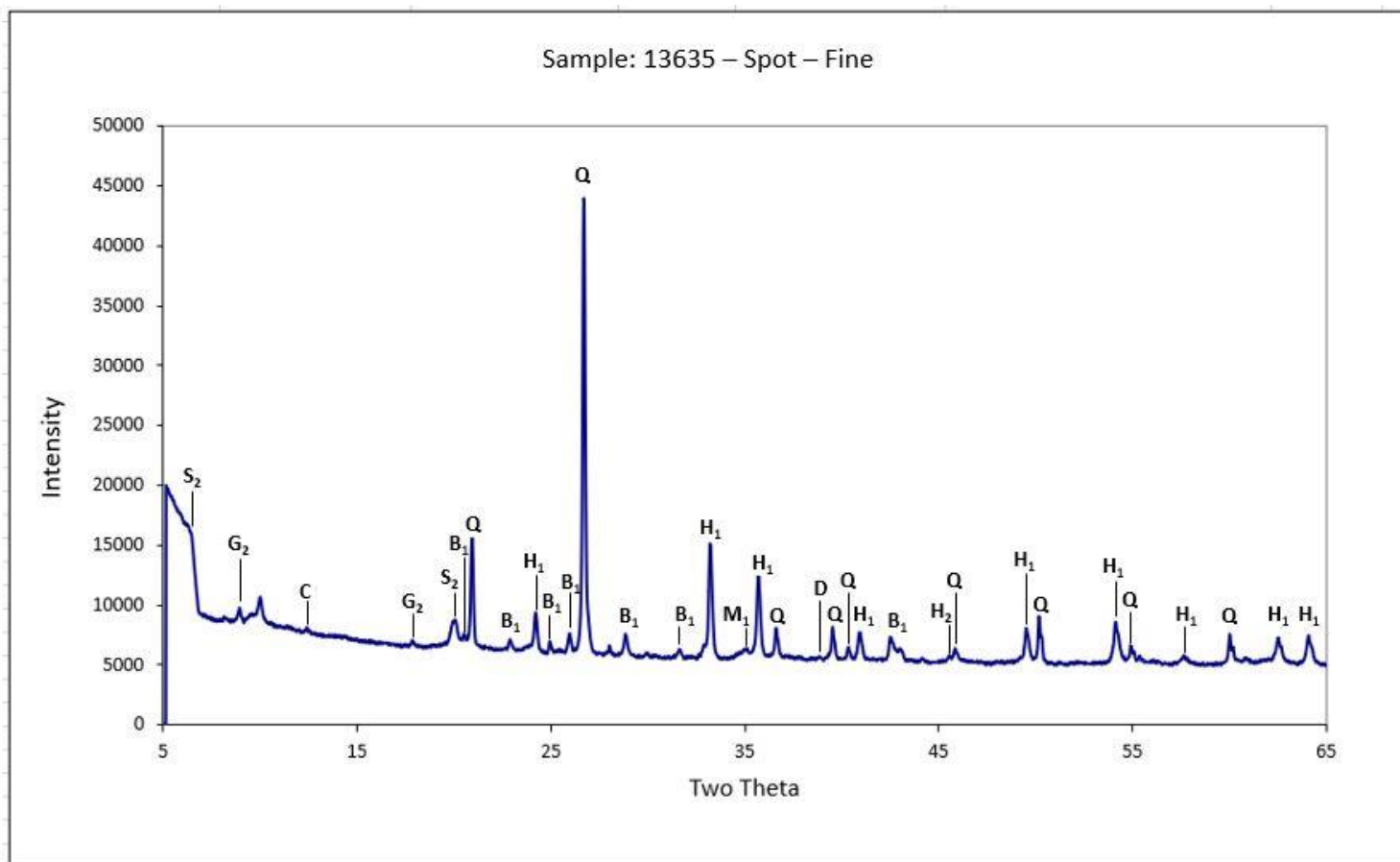


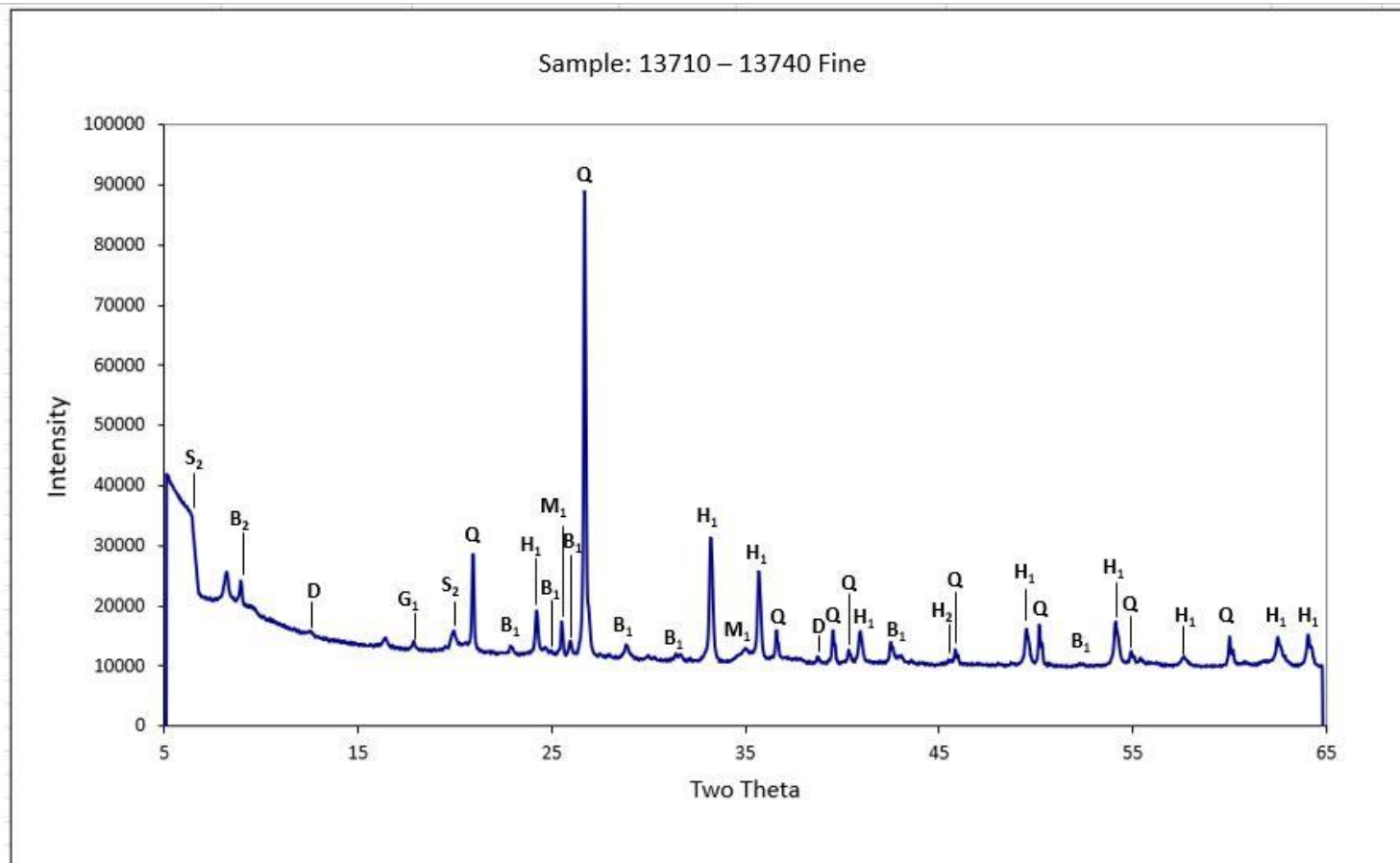


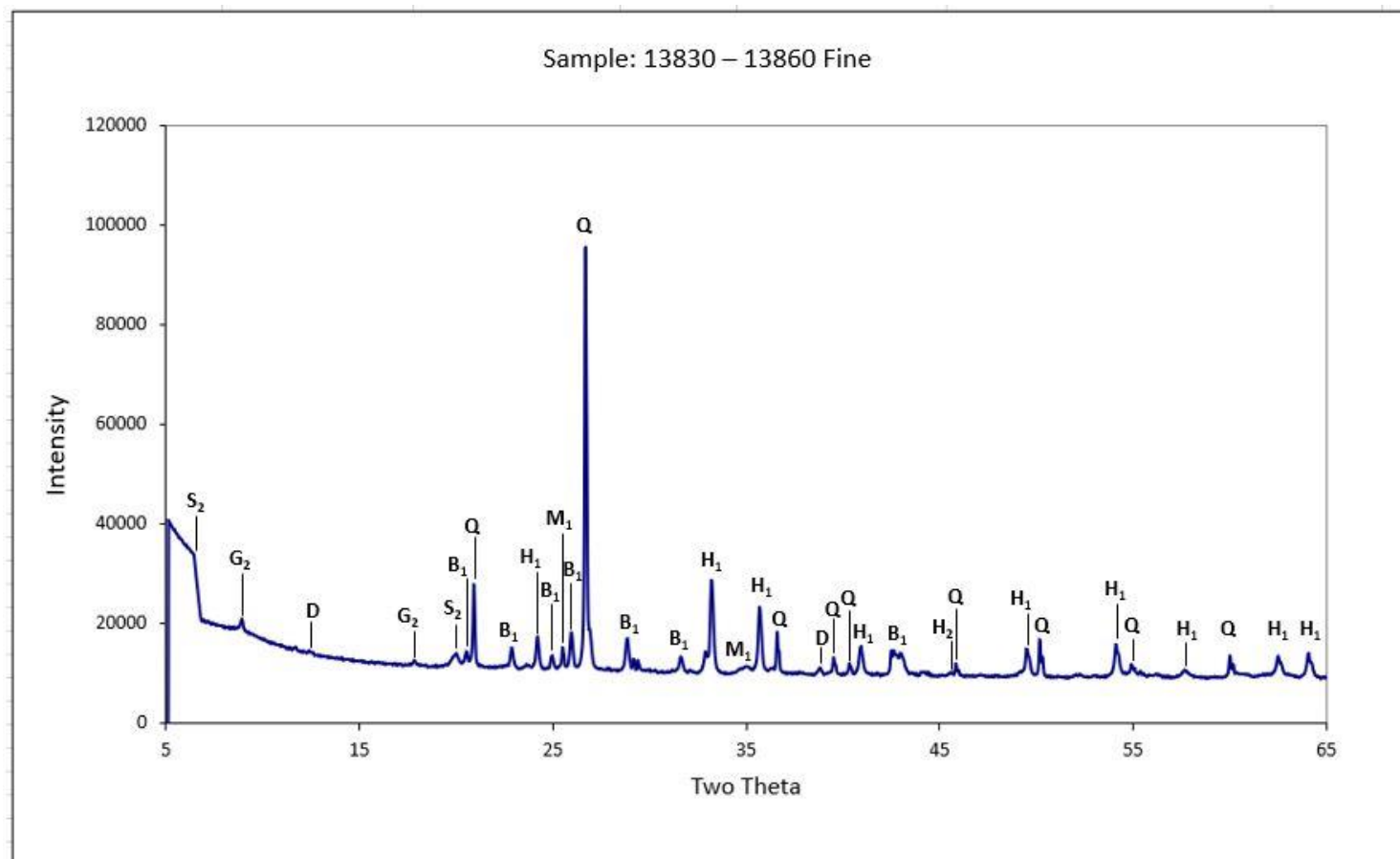


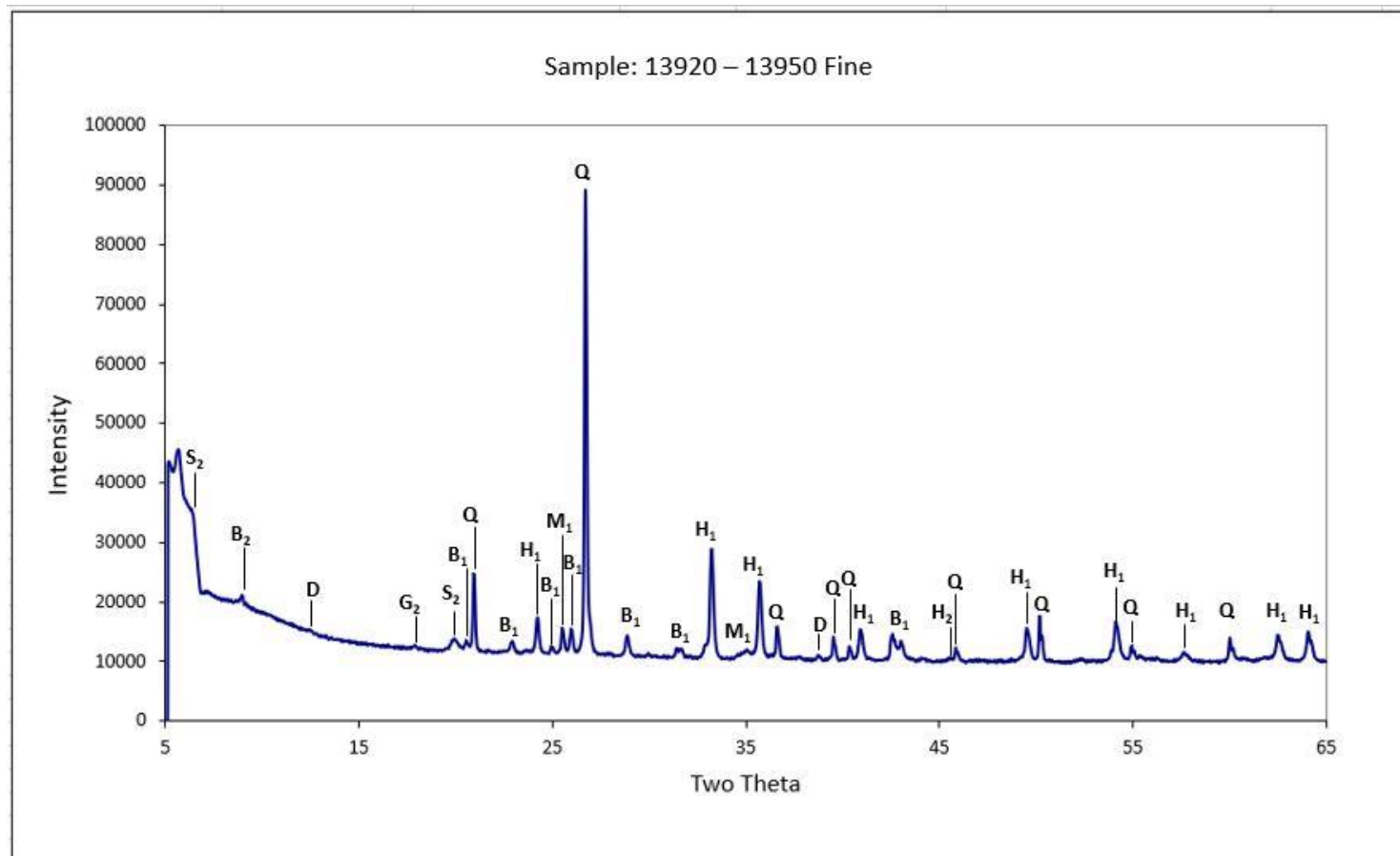




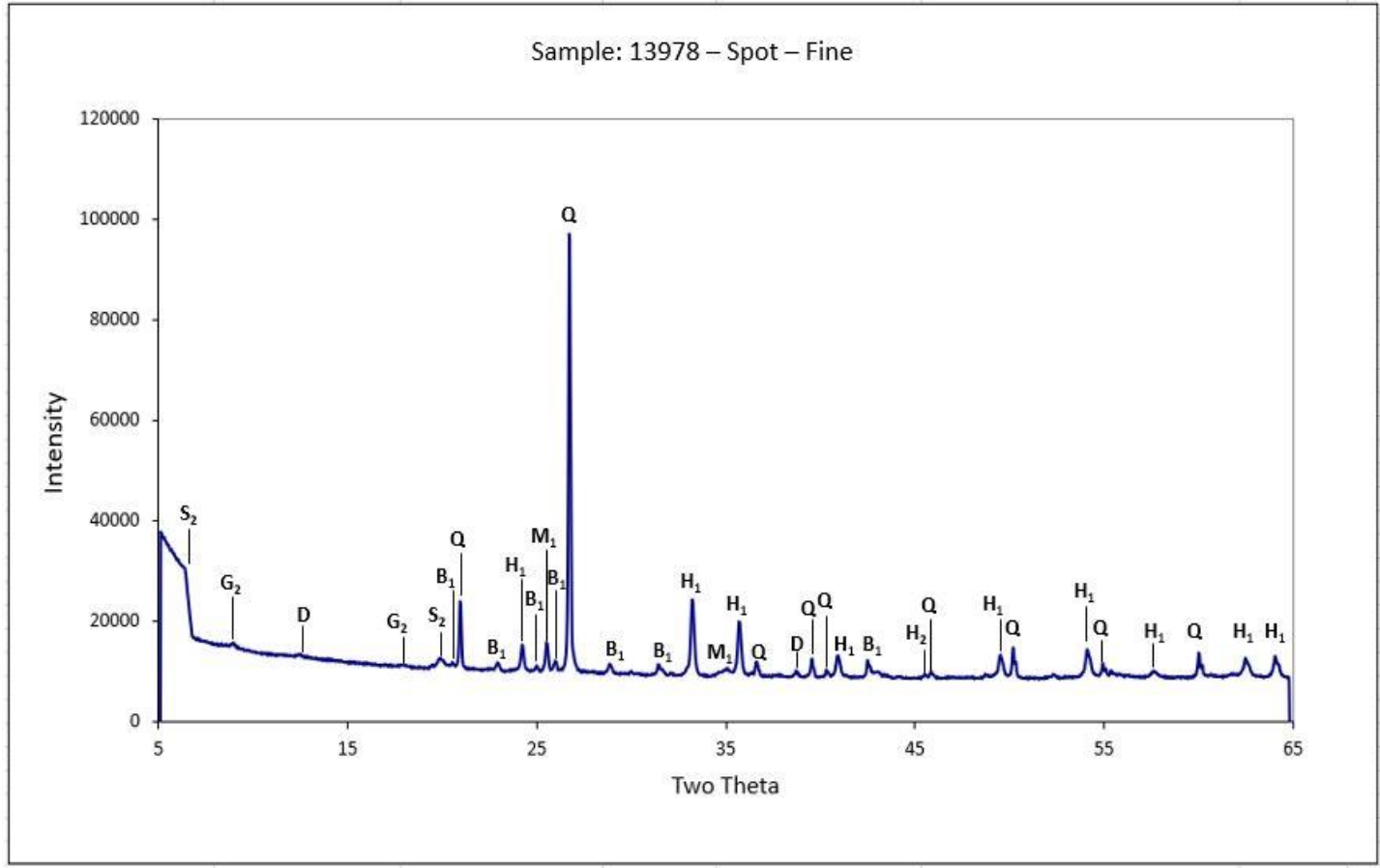












## 15. VITA

Brian L. Lesh graduated from McKinney High School in McKinney, TX in May 2010 and then enrolled at Stephen F. Austin State University the following August. He decided to major in geology in Spring, 2011 and continued taking classes at SFASU through Fall, 2013 until moving to San Antonio, TX. After some time, he decided to return to SFASU in Fall, 2017 determined to complete his Bachelor Degree. In August, 2019, he graduated with a Bachelor of Science majoring in Geology and minoring in General Business. Upon completion of his undergraduate degree, he enrolled at the Graduate School of Stephen F. Austin State University and graduated with a Master of Science in Geology in August, 2022.

Permanent Address: 23803 Castle Peak San Antonio, TX 78258

Style Manual Designation: GSA

This thesis was written by Brian L. Lesh